Université de Montréal

CRCHUM
CENTRE DE RECHERCHE

Research unit of biomechanics and imaging in cardiology

Ultrafast echocardiography

In vitro and in vivo study using diverging circular beams

by Daniel Posada

Research center, University of Montreal hospital (CRCHUM)

Department of physiology, Faculty of medicine

Biomedical Engineering department, University of Montréal

Memoire submitted to the faculty of graduate studies to obtain the title of Master of Science in biomedical engineering.

August 31, 2015

Resumé

Grâce à son accessibilité, sa polyvalence et sa sécurité, l'échocardiographie est devenue la technique d'imagerie la plus utilisée pour évaluer la fonction cardiaque. Au vu du succès de l'échographie ultrarapide par ondes planes des techniques similaires pour augmenter la résolution temporelle en échocardiographie ont été mise en œuvre. L'augmentation de la résolution temporelle de l'échographie cardiaque au-delà des valeurs actuellement atteignables (~ 60 à 80 images par secondes), pourrait être utilisé pour améliorer d'autres caractéristiques de l'échocardiographie, comme par exemple élargir la plage de vitesses détectables en imagerie Doppler couleur limitées par la valeur de Nyquist. Nous avons étudié l'échocardiographie ultrarapide en utilisant des fronts d'ondes ultrasonores divergentes. La résolution temporelle atteinte par la méthode d'ondes divergentes a permis d'améliorer les capacités des modes d'échocardiographie en mode B et en Doppler couleur. La résolution temporelle de la méthode mode B a été augmentée jusqu'à 633 images par secondes, tout en gardant une qualité d'image comparable à celle de la méthode d'échocardiographie conventionnelle. La vitesse de Nyquist de la méthode Doppler couleur a été multipliée jusqu'à 6 fois au delà de la limite conventionnelle en utilisant une technique inspirée de l'imagerie radar; l'implémentation de cette méthode n'aurait pas été possible sans l'utilisation de fronts d'ondes divergentes. Les performances avantageuses de la méthode d'échocardiographie ultrarapide sont supportées par plusieurs résultats *in vitro* et *in vivo* inclus dans ce manuscrit.

Keywords – Echocardiographie ultrarapide, onde divergente, onde plane, multiple PRFs commutées, Doppler couleur ultrarapide, extension de la vitesse de Nyquist

Abstract

Because of its low cost, versatility and safety, echocardiography has become the most common imaging technique to assess the cardiac function. The recent success of ultrafast ultrasound *plane wave imaging* has prompted the implementation of similar approaches to enhance the echocardiography temporal resolution. The ability to enhance the echocardiography frame rate beyond conventional values (~60 to 80 fps) would positively impact other echocardiography features, *e.g.* broaden the color Doppler unambiguous velocity range. We investigated the ultrafast echocardiography imaging approach using ultrasound diverging waves. The high frame rate offered by the *diverging wave* method was used to enhance the capabilities of both B-mode and color Doppler echocardiography. The B-mode temporal resolution was increased to 633 fps whilst the image quality was kept almost unchanged with reference to the conventional echocardiography technique. The color Doppler Nyquist velocity range was extended to up to 6 times the conventional limit using a weather radar imaging approach; such an approach could not have been implemented without using the ultrafast *diverging wave* imaging technique. The advantageous performance of the ultrafast *diverging wave* echocardiography approach is supported by multiple *in vitro* and *in vivo* results included in this manuscript.

Keywords – Ultrafast ultrasound, Ultrafast echocardiography, Diverging wave, Plane wave, Staggered multiple-PRF, Ultrafast color Doppler, Nyquist velocity extension

Acknowledgements

This memoire concludes my master degree in biomedical engineering at the University of Montréal. The main focus of my master was the ultrafast echocardiography technique using diverging waves to enhance both the temporal resolution and Nyquist velocity range known in conventional echocardiography. The work done included both *in vitro* and *in vivo* experiments that facilitated the validation of the researched imaging strategies.

I would like to express my deepest gratitude to my supervisor, Professor Damien Garcia at the university of Montreal hospital research center (CR-CHUM), for giving me the opportunity to participate of his research project, for introducing me to the ultrasound imaging field and for his unconditional support.

I would also like to thank my colleagues at the LBUM laboratory for all their help, fruitful discussions and ideas in regard to my project. I would like to express my special appreciation to Boris, research assistant at the LBUM laboratory, for helping me with all the *in vitro* setups and solving technical issues.

Lastly, I would like to thank my wife and mother for supporting me throughout this experience; it would not have been possible without their support.

Montreal, August 31, 2015

Daniel Posada

Contents

List of abbreviations

AIC_c:	Akaike's information criterion
AV:	Aortic valve
ceiling():	ceiling function
cm:	Centimetre
CNR:	Contrast to noise ratio
CW:	Continuous wave ultrasound
DCB:	Diverging circular beam
Echo-PIV:	Echographic particle image velocimetry
floor():	floor function
Hz:	Hertz
IQ:	In-phase and quadrature signal components
IVC:	Isovolumetric contraction
fps:	Frames per second
FWHM:	Full width at half maximum
lcm():	Least common multiple function
LV:	Left ventricle
LVOT:	Aortic out-flow-tract
max| |:	Max absolute value
mm:	Millimetre
mod():	modulus function
m/s:	Meters per second
MLA:	Multiline acquisition ultrasound approach
MV:	Mitral valve
nint():	nearest integer function
NRMSE:	Normalised root-mean-square error
PRF:	Pulse repetition frequency
PW:	Pulsed wave ultrasound
PZT:	Piezoelectric
RF:	Radiofrequency
RMSE:	Root-mean-square error
ROI:	Region of interest
RSS:	Sum of squares of the residuals
TGC_N:	Gain compensation function
VFM:	Vector flow mapping
TEE:	Transesophageal echocardiography
TTE:	Transthoracic echocardiography
US:	Ultrasound
VBV:	Vector blood velocity imaging
2D:	Two-dimensional
3D:	Three-dimensional

List of symbols

a	Material frequency-dependent attenuation
α	Attenuation coefficient
A	Amplitude decay
A_0	Wave original amplitude
A	Aperture area
b	Element half width
B	Bandwidth
β	Steering angle
β_{max}	Maximum steering angle
c	Ultrasound propagation velocity
$dir(\beta, \phi)$	Element directivity function (Angular response)
$D_b(\theta)$	Directivity function of an individual element
$\Delta\varphi$	Phase shift
Δx	Array pitch
ϵ_i	Error measurement
f_c	Center frequency
f_{cut}	Cut off frequency
f_d	Doppler frequency shift
$\forall$	For all
ϕ	Diverging circular beam angular width
$h(k)$	Filter impulse response
$i = \sqrt{-1}$	Imaginary unit
IQ	In phase and quadrature signal components
k	Wave number
λ	Wave length
n	Sample length
n_N	Nyquist number
n_PRF	Number of PRFs in the multiple PRF pulsing approach, 1, 2 or 3
N	Number of elements
N_A	Number of transmissions to create one B-mode image in focused ultrasound
N_B	Number of transmissions to create one compounded B-mode image
N_D	Doppler ensemble length
p	Acoustic field pressure
p_0	Original acoustic field pressure
$p(r, \theta)$	Radiation pattern pressure
ψ	B-mode tilting angle
$\frac{p_i}{q_i}$	Dual PRF ratio
Q	Flow rate
r	Interrogated ROI depth
$r_{\mathrm{max}\,\mathrm{roi}}$	Maximum interrogated ROI depth

r^2	Coefficient of determination
ρ	Medium density
$S_N(t)$	Gain compensated radiofrequency signals
$S(t)$	Compressed B-mode image
σ^2	Standard deviation
t	Time required to interrogate a given depth
T_{image}	Time required to generate one B-mode image
T_{duplex}	Time required to generate one duplex image
τ_n	Delay law
θ	Interrogated ROI angular position
Θ	Angle between the Doppler and particle velocity
w	Single element width
$v_0(\omega)$	Normal velocity in the frequency domain
V	Blood velocity
V_{N}	Nyquist velocity
V_{D}	Doppler velocity
V_{D}^{u}	Unambiguous Doppler velocity
V_{N_e}	Extended Nyquist velocity
μ	Mean
ω	Angular frequency
W_n	Weighing function
x_n	Centroid location of the n^{th} element
$x(n)$	Filter input (Unfiltered signal)
$\overrightarrow{x_n}$	Coordinates of every element in the phased array
$\overrightarrow{x_0}, \overrightarrow{z_0}$	Spatial location of the virtual source
$X(t)$	Bandpass radiofrequency signal
$\tilde{X}(t)$	Complex envelope
$X_+(t)$	Pre-envelope or analytic signal
$\hat{X}(t)$	Hilbert transform of the bandpass signal
$y(n)$	Filter output (Filtered signal)
Z	Material acoustic impedance
$\mathbb{Z}$	Integer number

Chapter 1

Introduction

Cardiovascular diseases are the main cause of mortality worldwide, resulting in around 14 million deaths every year, most of them attributed to heart disorders [1]. In this context, early diagnosis of cardiomyopathies would improve the cost-effectiveness of medical treatments and reduce the mortality rates associated with this type of health issue.

For more than 50 years, echocardiography has been used to investigate motion and hemodynamics of the heart [2, 3]; it is a radiation free, non-invasive medical imaging modality that allows real time assessment of the cardiac function. As the most widespread cardiac imaging technique, echocardiography is a valuable tool to diagnose a variety of cardiac anomalies [4], however, the quantitative information it provides is limited due to the following reasons:

Temporal resolution (frame rate): the conventional echocardiography temporal resolution is about 40 to 80 frames per second (fps). Considering that the cardiac cycle occurs in a brief period of time (0.8 second on average), higher echocardiography frame-rates would provide more detailed information on the human heart behaviour.

Conventional color Doppler unambiguous velocity range (Nyquist limit): blood velocities are unambiguously estimated by color Doppler only within the Nyquist range (velocities beyond the Nyquist limit experience aliasing). Taking into account that cardiac bloodstreams reach velocities beyond the echocardiography Nyquist range, extending the echocardiography color Doppler unambiguous range would contribute to more reliable cardiac blood flow measurements.

Solving the abovementioned issues would also allow emerging echocardiography applications to be developed, *e.g. color Doppler vector flow mapping* (VFM). In addition to the axial velocities estimated by color Doppler, the VFM application can provide 2D vector blood velocity maps [5]; such a technique uses axial velocities information to estimate the perpendicular transverse velocity. In echocardiography, color Doppler velocities provide the axial information needed by the VFM application; therefore, avoiding color Doppler aliasing becomes a priority. In the same way, enhancing the echocardiography frame-rate would benefit the VFM applications by providing more detailed information on the cardiac blood flow.

Keeping in mind the ideas laid out in the previous paragraphs, this document presents various methodologies that were implemented to enhance both the echocardiography temporal resolution and the unambiguous color Doppler velocity range; this document also includes the *in vitro* and *in vivo* results obtained using these approaches. The main purpose was to enhance the conventional echocardiography capabilities and improve the conditions of other emerging echocardiography applications.

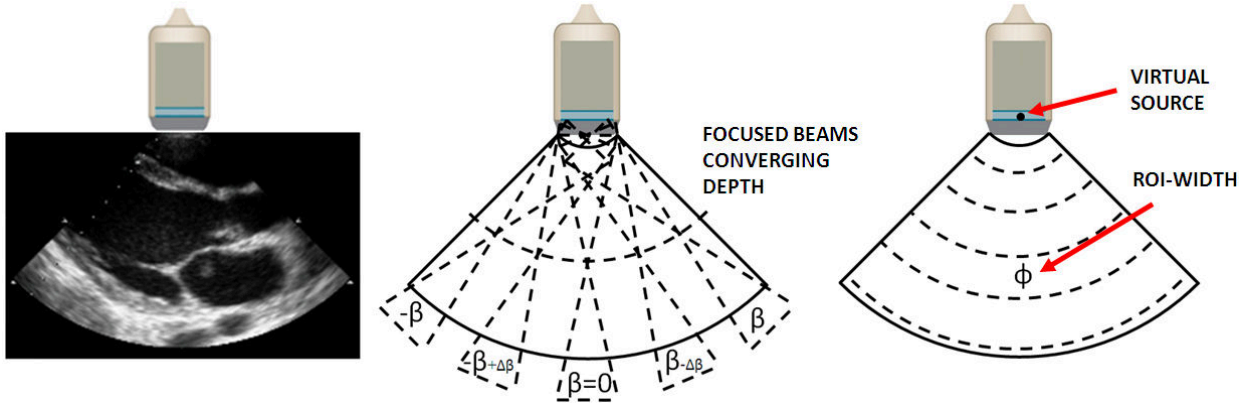

Fig. 1.1 – *Conventional cardiac ultrasound vs ultrafast echocardiography. Left panel:* Echocardiography parasternal long-axis view. *Center:* In conventional focused echocardiography, multiple tilted beams are transmitted within the angular range $[-\beta:\beta]$ to reconstruct one greyscale image. *Right panel:* Diverging circular beams insonify wide regions of interest; in consequence, one complete image can be created after each diverging beam is transmitted.

1.1 Conventional ultrasound vs ultrafast ultrasound

The main objective of the research presented in this manuscript was to increase echocardiography temporal resolution without degradation of the image quality featured by the conventional focused echocardiography approach; the high frame rate provided by *ultrafast ultrasound* was exploited to fulfill such a goal. *Ultrafast ultrasound* is possible thanks to the transmission of non-converging ultrasound beams, *e.g.* plane waves. Montaldo *et al* have shown that *ultrasound plane wave imaging* can provide comparable image quality to that of conventional focused ultrasound while significantly increasing the temporal resolution [6]. Although the interesting performance featured by plane wave imaging, such a technique is not well suited to conduct cardiac imaging; the sectorial echocardiographic region-of-interest (ROI) (see Fig. 1.1 – left panel) cannot be insonified with a single plane wave transmission.

In order to accomplish echocardiography high frame rates, diverging circular beams (DCB) were selected to develop the *ultrafast echocardiography* technique [7]; DCB are intuitively well suited to insonify the wide echocardiography ROI (see Fig. 1.1 – right panel). It was assumed that one complete sectorial image could be generated after every DCB transmission. The following paragraphs give a brief explanation of the *conventional* and *ultrafast echocardiography* methods addressed throughout this manuscript.

The *conventional echocardiography* approach fires consecutive tilted beams that converge to a given depth (see Fig. 1.1 – center panel); the traditional focused ultrasound approach reconstructs only one echographic line after every ultrasound beam is transmitted (one *A-line* at a time). Given that echocardiographic images gathers about 130 *A-lines*, the same number of tilted beams needs to be fired before one image is completed [8].

As opposed to the conventional echocardiography approach, *ultrafast echocardiography* creates one complete echographic image (130 *A-lines* at a time) after every ultrasound beam is transmitted; the last statement entails the imaging rate provided

with the ultrafast approach is at least a hundred times higher compared to the conventional ultrasound method.

1.2 Research hypothesis

Increasing echocardiography (B-mode and color Doppler) temporal resolution will provide more complete hemodynamic cardiac assessments. Such a high frame rate imaging approach should exhibit similar or better image quality and blood velocity estimates compared to the conventional technique.

1.3 Aims of study

The research presented in this manuscript aimed to develop an ultrafast echocardiography imaging technique (>700 fps) with extended color Doppler unambiguous range. The specific objectives pursued along this project were:

1. Increase the echocardiography technique temporal resolution using ultrafast ultrasound while maintaining the conventional image quality standards.
2. Extend the color Doppler unambiguous range by taking advantage of the high temporal resolution provided by *ultrafast ultrasound*.
3. Assess the image quality and color Doppler velocity estimates provided by ultrafast echocardiography (quantitatively and qualitatively).

1.4 Project methodology

State of the art review: A thorough literature review was performed to identify former contributions aiming to increase the echocardiography temporal resolution and extend the color Doppler unambiguous range. Advantages and weaknesses of former contributions were identified in order to define the project approach. A broad amount of articles and books are cited throughout this manuscript in case the reader requires further explanation and/or illustration.

Diverging circular beams implementation using the Verasonics scanner: The DCB echocardiography imaging approach was implemented using the Verasonics system; this is an open architecture ultrasound device that allows transmitting arbitrary ultrasound beams as well as recording the reflected ultrasound echoes (for post-processing).

Conventional vs ultrafast echocardiography image quality comparison: The image quality of the ultrafast and conventional echocardiography approaches were compared to each other. Both the spatial resolution and contrast to noise ratio were quantified using the two techniques. The results allowed an assessment of the ultrafast method (see chapter 4, section 4.3).

Ultrafast color Doppler *in vitro* assessment: ultrafast Color Doppler imaging was performed using diverging waves and staggered pulse repetition frequencies (PRFs). *In vitro* experiments were conducted to verify the accuracy of this technique (see chapter 5, section 5.2.3).

Ultrafast echocardiography *in vivo* examinations: Healthy volunteers were examined using both ultrafast B-mode and ultrafast color Doppler echocardiography; the ultrafast echocardiography technique was qualitatively assessed.

1.5 Memoire outline

This manuscript is organized as explained in this paragraph: *chapter two* introduces the anatomy of the human heart and left ventricle (LV) hemodynamics. Chapter two also presents the echocardiography technique and the main emerging cardiac blood velocity vector (BVV) imaging approaches. *Chapter three* presents ultrasound imaging principles (B-mode and Doppler) and some signal processing related methods. *Chapter four* presents how echocardiography temporal resolution was increased using diverging beams [5, 9]. *Chapter five* explains how the color Doppler unambiguous range was extended using staggered PRFs. *Chapter six* offers a brief discussion of the work done.

1.6 Supplementary Work

The color Doppler unambiguous range extension using staggered PRFs was also implemented for vascular imaging (using plane waves). Experiments were conducted in a common carotid artery (see chapter 5, section 5.3.3).

1.7 List of publications and presentations

The publications and presentations listed below were respectively written and given by the author throughout the research project execution:

Papers included in this memoire

1. **Daniel Posada** , Arnaud Pellissier , Boris Chayer, François Tournoux, Guy Cloutier, Damien Garcia. "Staggered multiple-PRF ultrafast color Doppler" (submitted to IEEE Transactions on medical imaging).

Conference proceedings

1. **Daniel Posada**, Sarah Dort, Boris Chayer, Shahrokh Shahriari, Guy Cloutier, Hervé Liebgott, Damien Garcia. "Towards High Frame Rate Cardiac Ultrasonography - a Circular Wave Imaging Approach". *Proceedings of IEEE International Ultrasonics symposium (IUS), 2013,* Joint UFFC, EFTF and PFM symposium, Prague, Czech Republic, july 21-25, 2013.
2. **Daniel Posada**, Boris Chayer, Guy Cloutier, Damien Garcia. "Nyquist velocity extension in ultrafast color Doppler". *Proceedings of IEEE International Ultrasonics symposium (IUS), 2014,* Joint UFFC, EFTF and PFM symposium, Chicago, USA, september 3-6, 2014.

Presentations and posters

1. **Daniel Posada .** "Ultrafast cardiac ultrasound", *The Artimino Conference on Medical Ultrasound Technology,* 2013.
2. **Daniel Posada,** François Tournoux, Guy Cloutier, Damien Garcia. "Ultrafast echocardography". *Ultrasonics symposium (IUS),* 2014 *IEEE International*.
3. **Daniel Posada**, Sarah Dort, Boris Chayer, Shahrokh Shahriari, Guy Cloutier, Hervé Liebgott, Garcia D. "Towards High Frame Rate Cardiac Ultrasonography - a Circular Wave Imaging Approach". *Ultrasonics symposium (IUS),* 2013 *IEEE International*.
4. **Daniel Posada**, Boris Chayer, Guy Cloutier, Damien Garcia. "Nyquist velocity extension in ultrafast color Doppler". *Ultrasonics symposium (IUS),* 2014 *IEEE International*.

Bibliography

[1] W. H. Organization. *The top 10 causes of death*. (2014).

[2] D. H. Evans, *Doppler ultrasound: Physics, instrumentation, and clinical applications*: John Wiley & Sons, 1989.

[3] B.-F. Osmanski*, et al.*, "Ultrafast Doppler Imaging of Blood Flow Dynamics in the Myocardium," *Medical Imaging, IEEE Transactions on,* vol. 31, pp. 1661-1668, 2012.

[4] V. Mor-Avi*, et al.*, "Current and evolving echocardiographic techniques for the quantitative evaluation of cardiac mechanics: ASE/EAE consensus statement on methodology and indications: endorsed by the Japanese Society of Echocardiography," *Journal of the American Society of Echocardiography,* vol. 24, pp. 277-313, 2011.

[5] P. P. Sengupta*, et al.*, "Emerging trends in CV flow visualization," *JACC: Cardiovascular Imaging,* vol. 5, pp. 305-316, 2012.

[6] G. Montaldo*, et al.*, "Coherent plane-wave compounding for very high frame rate ultrasonography and transient elastography," *Ultrasonics, Ferroelectrics and Frequency Control, IEEE Transactions on,* vol. 56, pp. 489-506, 2009.

[7] H. Hasegawa and H. Kanai, "High-frame-rate echocardiography using diverging transmit beams and parallel receive beamforming," *Journal of Medical Ultrasonics,* vol. 38, pp. 129-140, 2011.

[8] V. Chan and A. Perlas, "Basics of ultrasound imaging," in *Atlas of Ultrasound-Guided Procedures in Interventional Pain Management*, ed: Springer, pp. 13-19, 2011.

[9] C. Papadacci*, et al.*, "High-contrast ultrafast imaging of the heart," *IEEE transactions on ultrasonics, ferroelectrics, and frequency control,* vol. 61, pp. 288-301, 2014.

Chapter 2

Cardiac hemodynamics, Echocardiography and vector blood velocity imaging

The human heart can be visualised using a variety of medical imaging tools, *e.g.* nuclear imaging, angiography, cardiac magnetic resonance (CMR), cardiac computed tomography and echocardiography (other might exist but these are the most widespread). Due to its low cost, simplicity and safety, echocardiography occupies a very unique position among the cardiac imaging techniques; on the other hand, echocardiography does not provide 2D blood velocities as other techniques do, *e.g.* CMR provides 2D and 3D time resolved blood flow maps. Emerging ultrasound based techniques such as color Doppler VFM would give echocardiography the capability to estimate 2D blood velocities; however, enhancing the conventional echocardiography temporal resolution and unambiguous color Doppler velocity range would be necessary to efficiently implement the VFM imaging application.

In this chapter, the reader can find information related to the following physiological and imaging topics: The heart anatomy and the LV hemodynamics; the conventional echocardiography technique capabilities and limitations; the most known cardiac vector blood velocity imaging techniques: CMR, echo-PIV and *color Doppler VFM*; and finally, the relevance to further improve the *color Doppler VFM* application.

2.1 Cardiac anatomy and left ventricle hemodynamics

Echocardiography allows visualisation of the blood flow through the human heart and motion of the cardiac structures. Among the four cardiac chambers, the LV outstands because of its size and the strength needed to pump blood to the whole human body; given the importance of the LV, it becomes the main target of the echocardiographic examination. All the structures attached to the LV are also of high interest during the cardiac echo examination (see Fig. 2.1):

The mitral valve (MV): The MV separates the left atrium from the LV; such a valve serves as a gate between the pulmonary circulatory system and the LV.

The papillary muscles: The papillary muscles are attached to the LV and the mitral valve leaflets. These muscles help the mitral valve open as the LV dilates and close as the LV contracts.

The aortic valve (AV): The AV works as a gate between the aorta artery and the LV. The AV allows oxygenated blood to flow towards the arterial circulatory system.

The left ventricular outflow tract (LVOT): The LVOT is a cavity that conducts the blood flow out of the LV towards the aorta artery.

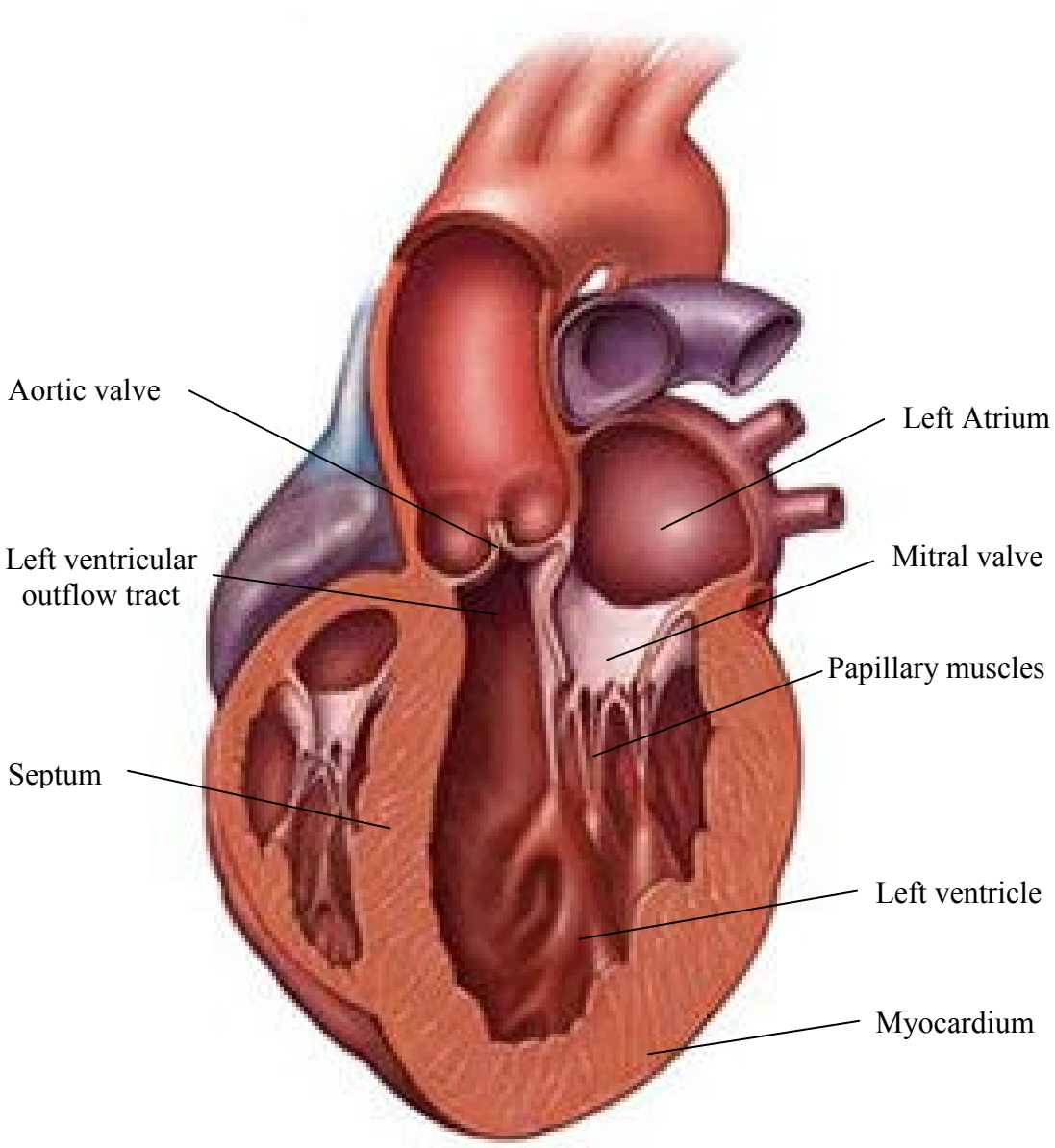

Fig. 2.1 – *Most relevant cardiac structures that interact with the LV* (source: Mayo Foundation for Medical Education and Research, http://www.mayoclinic.org).

The pericardium/myocardium/endocardium: The pericardium, myocardium and endocardium are the tissue layers that enclose the left and right ventricles.

Beyond the interest inspired by the internal structures of the heart, the LV exhibits particular hemodynamic events that can be visualised using cardiac imaging methods, *e.g.* color Doppler echocardiography and echo-PIV. Progressively, more and more studies aim to correlate the cardiac function to the LV hemodynamics, for instance, Mehregan *et al* used color Doppler echocardiography to identify abnormal vortexes in the LV; such a technique could be exploited to identify potentially diseased patients [1]. The hemodynamics events that take place in the LV during the cardiac cycle are presented in the following paragraphs.

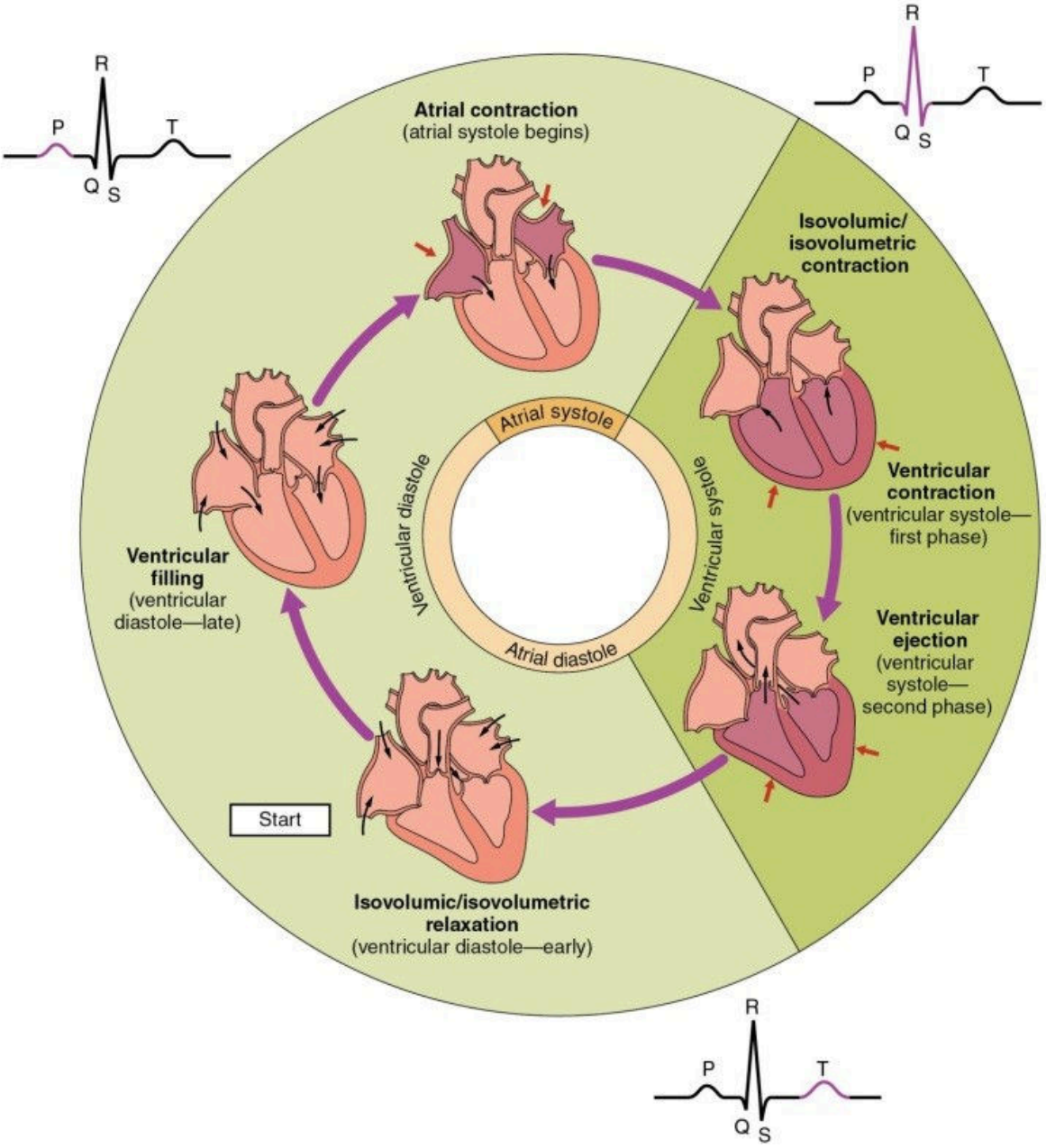

Fig. 2.2 - *Hemodynamic phases inside the cardiac chambers.* In clockwise sense: *Isovolumetric relaxation*, *ventricular filling*, *atrial contraction*, *ventricular contraction* and *ventricular ejection* [2].

2.1.1 Cardiac hemodynamics

The human heart has two atriums and two ventricular chambers. Despite the importance of all these chambers, the LV is the one responsible to pump oxygenated blood into the arterial circulatory system. Considering the demanding job performed by the LV, it is not a surprise this chamber exhibits the most active hemodynamics in the human body. Extensive research has made possible the identification of the hemodynamic stages that take place

during the cardiac cycle [3]; a thorough description of the LV hemodynamics is presented in the following paragraphs (see Fig. 2.2):

Isovolumetric relaxation: The heart muscle enters its relaxing mode with the valves closed. The ventricular pressure rapidly declines but the volume in the LV remains constant. This phase lasts until the ventricular pressure drops below the atrial pressure; at this specific moment the mitral valve opens and the ventricular filling starts.

Ventricular filling: The LV relaxes which generates a pressure gradient from the left atrium. During this phase, the mitral valve is wide open so blood can flow from the left atrium to the LV. Although pressure in the LV is lower than pressure in the ventricular outflow tract, the aortic leaflets prevent any backflow from the aorta.

Atrial contraction (systole): Both atriums contract at the same time increasing the pressure in the atriums and pumping remaining blood into the right and left ventricles. This hemodynamic phase is also known as *atrial kick*.

Isovolumetric contraction: The myocardial tension forces the mitral valve to close. During this phase, both the mitral and aortic valves remain closed, therefore, pressure in the LV rapidly rises under constant volume conditions.

Ventricular systole: Pressure builds up inside the LV as this one contracts; this phase is known as *ventricular contraction* or *first phase of the ventricular systole*. Subsequently, the aortic valve is naturally released, which enables blood to flow into the arterial circulatory system; this phase is known as *ventricular ejection*.

2.1.2 Left ventricle vortex and its use as a cardiac function marker

The human heart shares many similarities with hydraulic systems. By the same token, the blood flow depends on the boundaries imposed by cardiovascular system. Laminar and turbulent stream patterns may appear in the human body; such patterns are the result of the momentum generated by blood motion and the frictional effects caused by anatomical boundaries, *e.g.* the heart and vessel walls [4]. Although turbulent patterns are not usual in the circulatory system, a turbulent vortex that appears into the LV seems to have positive properties. Recent *in vivo* studies using echo-PIV have described the formation of such a vortex inside the LV. According to Cimino *et al.*, the left-ventricular vortex adopts different shapes along the cardiac hemodynamic cycle [5]. Cimino *et al* also suggests such a vortex exhibits variations in sick patients; it is with this in mind that the characterization of such a vortex could help create alternative markers to diagnose cardiac disorders.

Non-invasive *vector blood velocity* imaging techniques such as *color Doppler VFM* would be valuable to assess the intraventricular blood flow vorticity. However, the color Doppler velocities used by the *color Doppler VFM* application are often incorrectly measured by the echocardiography technique (velocities display aliasing). In addition, the temporal resolution of the conventional color Doppler technique does not provide enough information per cardiac cycle to effectively implement the *color Doppler VFM* application. Generating more accurate color Doppler estimates at higher frame rates, would allow the *color Doppler VFM* application to conduct efficient and accurate cardiac hemodynamic assessments.

2.2 Echocardiography examination review

Among the numerous existing cardiac imaging techniques, only echocardiography has become ubiquitous [6]; this happened thanks to its low cost, use of non-ionising radiation, portability, and its ability to carry out non-invasive cardiac examinations in real time. All these features have allowed echocardiography to develop at a rapid and steady pace. The addition of new echocardiographic applications such as color Doppler, tissue Doppler, speckle tracking, just to mention a few, have led this imaging technology to occupy a pivotal position in the diagnosis and follow up of the heart function.

Echocardiography was originated in the mid 1940's when the German physician Wolf-Dieter Keidel investigated the use of ultrasound with medical diagnosis purposes. At that time he proved that rhythmic volume variations of the heart could be measured using ultrasound. In the early 1950's Inge Edler and Carl Hellmuth Hertz continued to develop echocardiography in Lund-Sweden; they found that ultrasound frequencies in the megahertz range were needed to emit ultrasonic energy deep into human tissues and produce useful 2D echographic images. By the mid 1950's echocardiography was already used as a routine diagnostic tool. During the 1960's, the clinical application of echocardiography spread over Europe and the United States, making possible many cardiac diagnostic procedures. In the 1970's echocardiography witnessed three big revolutionary events: first, the introduction of linear arrays for real time imaging by Griffith and Henry; second, the discovery of contrast echocardiography by Gramiak; third, the beginning of spectral continuous ultrasound Doppler. The introduction of these echocardiographic tools skyrocketed the popularity of the cardiac-echo technique.

Following the echocardiography revolution in the 70's, color Doppler came along in the 1980's to reinforce the importance of cardiac ultrasonography. Since then, echocardiography has settled as an affordable technique thanks to its demand and big success. In the recent years, the low cost to produce ultrasound machines has increased its usability around the world; moreover, thanks to the present position occupied by echocardiography in the clinical setting, many innovating research projects strive to further improve multiple features of this imaging modality [7].

The transthoracic and transesophagial echocardiographic approaches are presented in the following paragraphs. It is also explained how structures and/or blood flow inside the cardiac chambers can be visualized using this imaging technique.

2.2.1 The transthoracic echocardiography approach (TTE)

During the transthoracic echocardiography examination, the phased array transmits ultrasonic energy into the heart through the gaps existing between the ribs; the ultrasound transducer is positioned using to the distinctive landmarks exhibited by the heart, *e.g.* the apex and septum. Multiple transthoracic views can be obtained depending on the transducer position over the thoracic cage: (A) parasternal/suprasternal, (B) subcostal or (C) apical (see Fig. 2.3 - left-panel). The echocardiographic views are classified in terms of the transducer approach, but also in function of the long and short axis concept. The long axis is the line crossing the heart from the apex to the left ventricular outflow tract; the short axis is located in the plane perpendicular to the long axis (see Fig 2.4 – upper-right panel).

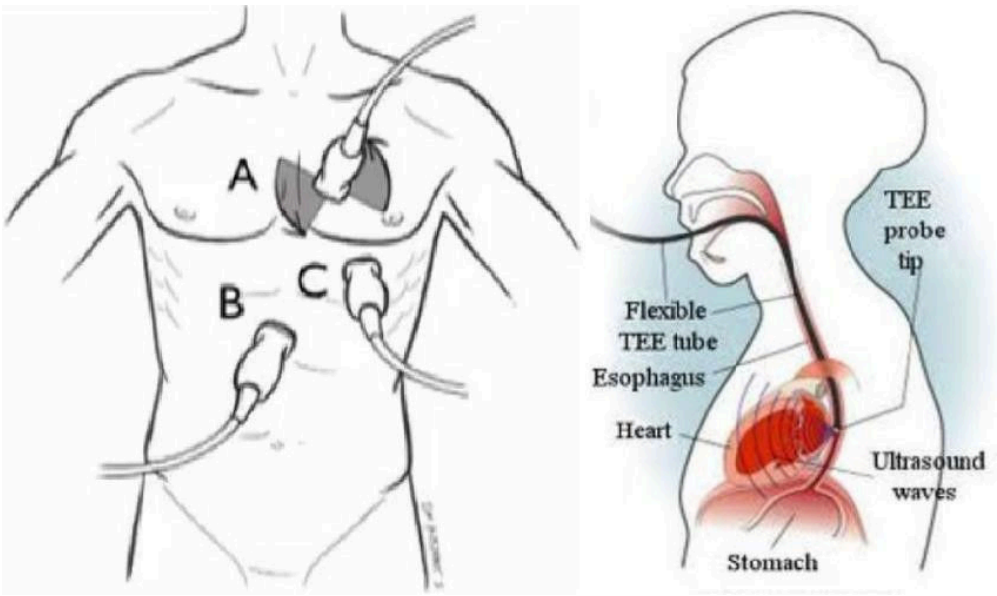

Fig. 2.3 - *Transthoracic and trasesophageal echocardiography approaches. Left panel:* Transthoracic echocardiography approaches. (A) Parasternal and suprasternal approach, (B) Subcostal approach and (C) Apical approach. *Right panel:* Trasesophageal echocardiography approach [8].

The ultrasound transducer position establishes whether the view of the heart is acquired along the short or long axis, *e.g.* apical views can only be longitudinal. In some cases, the same approach can provide both short and long-axis views, *e.g.* the parasternal approach can provide both short-axis and longitudinal views. The most common transthoracic echocardiography views are presented in the following paragraphs [9]:

The *parasternal long-axis* (PLAX) view (see Fig. 2.4 - left-upper-panel): as stated by its name, this view is conducted from a parasternal transthoracic approach, the left and right ventricles, as well and the left ventricular outflow tract and the left atrium can be displayed.

The *parasternal short-axis* (PSAX) view (see Fig. 2.4 - right-upper-panel): The parasternal short axis view can be performed at different heights along the LV; from the apex through the aortic valve level. This view displays how the LV contracts and relaxes in the radial direction.

The *apical four-chamber* (A4C) view (see Fig. 2.4 - left-lower-panel): The transducer is placed in the 5th intercostal space. The left and right ventricles as well as the right and left atriums can be visualised in the echocardiographic image.

The *apical two-chamber* (A2C) view (see Fig. 2.4 - right-lower-panel): This view is performed from an apical approach; the LV and the left atrium are captured in this view.

In addition to the four echocardiographic views described before, the apical long axis (also called apical three-chamber view) is a less frequently used echocardiographic view of the heart (see Fig. 2.5). The left ventricular outflow tract, the mitral valve and the aortic valve are completely included in this view.

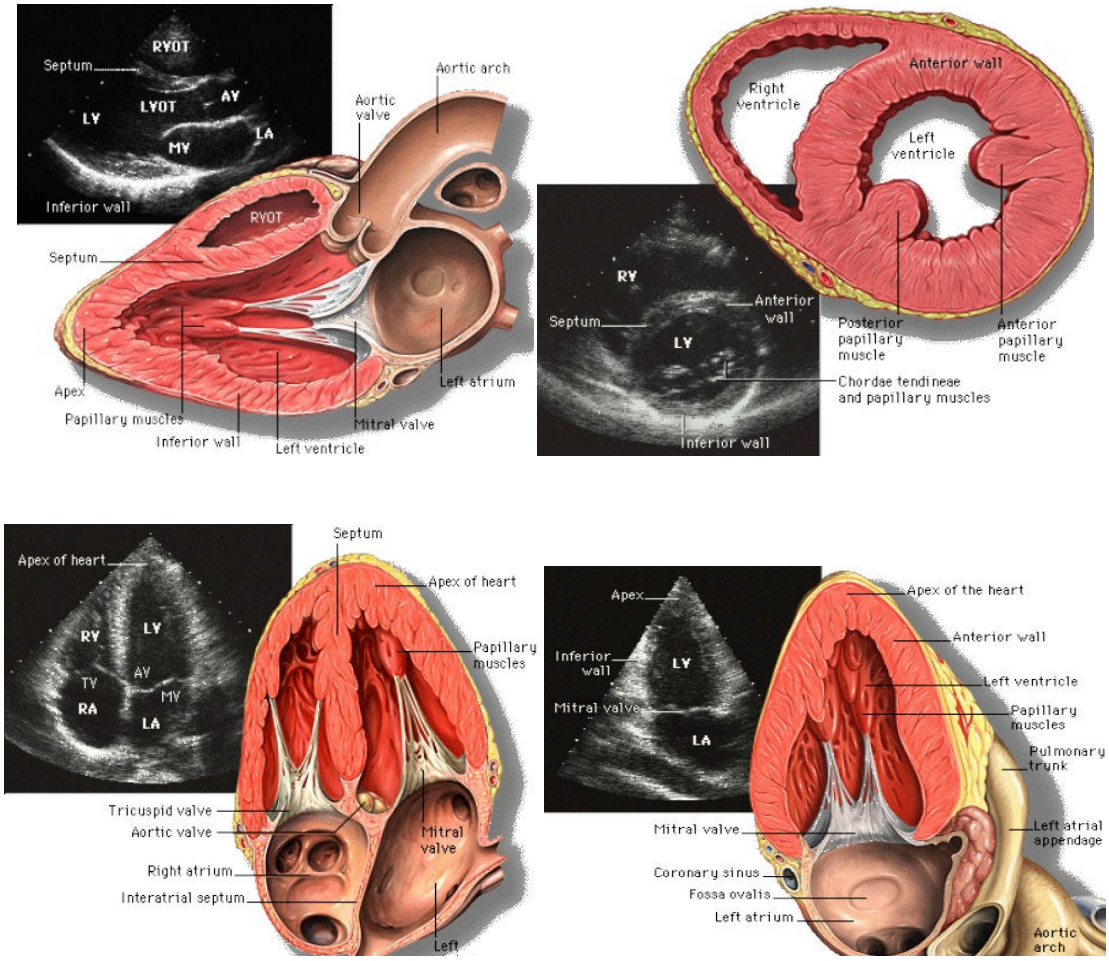

Fig. 2.4 - *Right-upper panel:* Parasternal long-axis view. *Right-upper panel:* Parasternal short- axis view. *Left-lower panel:* Apical four-chamber view. *Right-lower panel:* Apical two-chamber view [10].

The three-chamber view is especially convenient to perform either continuous or color Doppler examinations; stenosis and regurgitation on the aortic and mitral valves can be determined using this type of view. Also, in the apical three-chamber view, the left ventricular outflow tract and the ultrasound beam are aligned which helps measuring the maximal blood velocities (jet-velocity) during the ventricular diastole by using Doppler ultrasound (see section 2.1.1 for more details on cardiac phases). Moreover, thanks to the particular position of the LV and the aortic out-flow-tract in this view, color Doppler is used as gold standard to detect aortic insufficiency [11].

A particular property of the apical three-chamber view is its capacity to image the plane in which the intracavitary blood flow can be simplified to a 2D scenario. Although the intracardiac blood flow is known to have a the three-dimensional nature, recent studies have revealed that essential flow dynamics parameters of the heart can be accurately approximated using this 2D view [1, 12, 13].

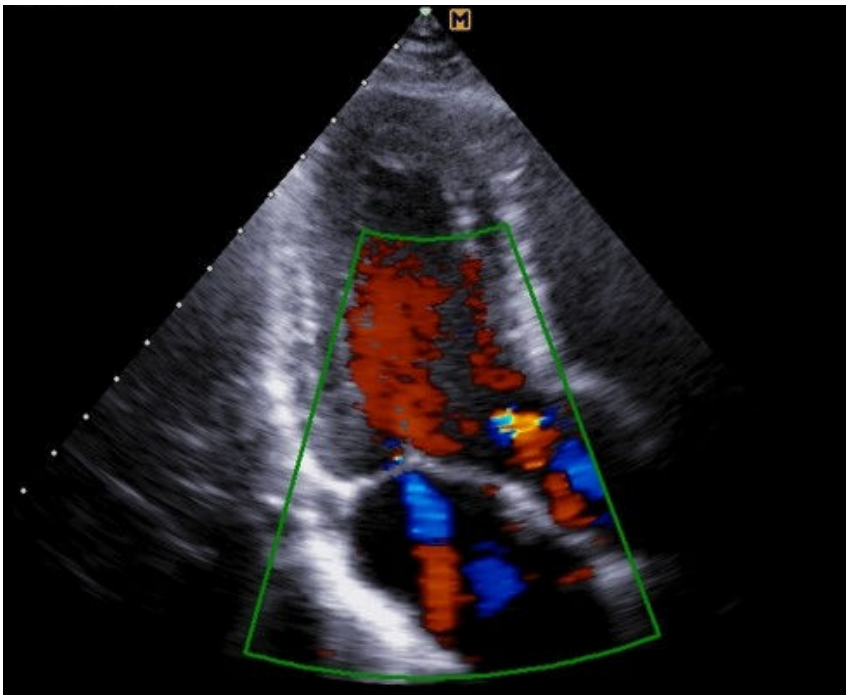

Fig. – 2.5 *Apical long axis or Apical 3-chamber view:* The LV, the left ventricular outflow tract (LVOT), the mitral valve (MV) and the aortic valve (AV) are displayed during systole [14].

2.2.2 The transesophageal echocardiography approach (TEE)

The transesophageal echocardiography examination is conducted through the esophagus (see Fig. 2.3 - right-panel). A slim and flexible tube carrying a transducer at the tip is introduced through the throat and then into the esophagus. This technique might be capable of providing higher quality images than those obtained with the transthoracic approach; the main reasons are the transducer being closer to the heart and the higher central frequency of the ultrasound transducer (typically 5 MHz). However, as all endoscopic procedures, transesophageal echocardiography entails a moderate probability of complications [6, 15], as opposed to the very low risk related to the TTE imaging approach. The TEE technique is indicated when transthoracic echocardiography is not feasible or does not provide sufficient information of the cardiac function. Also, it is suitable to detect cardiac sources of embolization and when conducting catheterisation procedures. Since the motivation of this memoire has been the transthoracic echocardiography approach, only a general explanation of the TEE method is available here; nonetheless, more complete information concerning this approach can be found in the book *"A practical approach to transesophageal echocardiography"* [16].

2.2.3 Conventional echocardiography capabilities

When echocardiography was introduced in the 1950's, it was only capable of generating single echographic lines of the heart. As time went by, multiple features were developed and added to this clinical tool. Nowadays, the capabilities integrated into echocardiography allow not only seeing the structures of heart, but also measuring the tissue motion

(myocardium) and quantifying the blood flowing in and out of the LV. In order to outline the current capabilities exhibited by echocardiography, the most frequently used echocardiographic applications are presented in the following paragraphs [17]:

M-mode: The M-mode imaging application provides a 1D view of the heart. A single echographic line is acquired by insonifying the heart always in the same region; subsequently, these lines are displayed one after the other as a function of time. The temporal resolution of the M-mode application is relatively higher in comparison to the other echocardiographic tools; this is because the target of the ultrasound beam is always located at the same spot.

B-mode (2D-imaging): The B-mode imaging application provides two-dimensional images of the heart. It is considered the backbone of echocardiography, making it possible to visualize moving structures in real time. The B-mode echocardiographic images display cross-sectional views of the heart; these images can be used to determine the presence of abnormal anatomy or non-conventional movements of the cardiac structures.

Continuous-wave (CW) Doppler: This technique uses the Doppler principle to measure the frequency shift encountered between the transmitted ultrasound waves and reflected echoes. The spectral representation of ultrasound echoes enable identifying velocity fluctuations on the blood stream; on the other hand, the continuous-wave Doppler approach is limited to measuring mean velocities through the ultrasound beam (no spatial resolution can be attained with this technique).

Pulsed-wave (PW) Doppler: It was developed to solve the boundaries featured by the continuous Doppler approach. This technique uses ultrasound pulses instead of continuous ultrasound beams. This method can estimate the blood-flow velocity at a specific depth, providing hemodynamic information through specific anatomical structures. Among other applications, PW Doppler can be used to establish ventricular in-flow patterns and intracardiac shunts.

Color Doppler (Color-flow mapping): The color Doppler imaging tool goes a step further than the pulsed-wave Doppler technique by providing colourful images of the intraventricular blood flow. Red and blue scale colors are displayed when blood flows towards or away the ultrasound transducer respectively. Color Doppler provides valuable information when specific anomalies such as regurgitations, valves sclerosis or cardiac shunt are present.

Color M-mode: This technique combines the working principle of the color Doppler technique with the display scheme of the M-mode approach. Color Doppler lines are displayed one after the other vs. the examination elapsed time. As for the M-mode technique, color M-mode exhibit a high temporal resolution because of the static focusing transmission strategy but as the brightness M-mode approach its applications are limited. The propagation velocity and the pressure gradient are the main two examinations that exploit color M-mode.

Contrast echocardiography: This technique uses contrast agents such as agitated saline or synthetic micro-bubbles to enhance the reflectivity of the blood-flow inside the cardiac chambers. The contrast agents utilised during this examination are injected intravenously.

Tissue Doppler (TDI) and strain imaging: These two modalities facilitate keeping track of the myocardium strains and velocities. The tissue Doppler imaging technique utilises the same principles exploited by the pulsed-wave color Doppler method, but significant adjustments are necessary to estimate slowly tissue motion in real time [18]. Cardiac strain imaging uses block matching algorithms to calculate myocardial velocities and deformations; currently, this procedure can be only executed offline [19].

2.2.4 Conventional echocardiography limitations and improvement opportunities

The numerous functions featured by Echocardiography justify its popularity in the cardiac imaging field [20]. However, conventional echocardiography only detects cardiac dysfunction when patients start deteriorating. Considering that half of the population affected by heart diseases exhibit a normal systolic function, researchers are interested in finding a way to early diagnose cardiac pathologies. Recent studies have demonstrated that abnormal diastolic features can be detected using vector blood velocity (VBV) imaging techniques. The advantage of the VBV imaging method over color Doppler is its ability to estimate not only the axial but also the transverse blood velocities (two different velocity components). Multiple VBV imaging approaches have been recently used to describe the human cardiac hemodynamics [4]. Imaging techniques such as Echo-PIV, phase-contrast CMR, and *color Doppler* VFM, have made it possible to obtain the first vector blood velocity charts from within the LV; these preliminary results along with the advantages featured by ultrasound imaging have motivated interest to develop ultrasound based tools to characterize the cardiac blood-flow.

Being capable of characterizing the blood dynamics of the heart could empower cardiologist to better and earlier diagnose patients suffering from cardiac disorders. Furthermore, therapies available to treat heart disorders could dramatically increase their effectiveness if addressed during early symptomatic stages. It is also worth noting that two of the imaging modalities used so far to characterize the cardiac blood-flow utilize B-mode and color Doppler echocardiography. The previous fact is the drive for the future echocardiography challenges, among them the two improvements that are subject of this research: a higher temporal resolution and a broader unambiguous Doppler velocity range. Boosting these echocardiography features would positively impact techniques such as echo-PIV and *color Doppler VFM*, which would result in earlier and more accurate diagnosis.

2.3 Vector blood velocity imaging techniques

Cardiac vector blood velocity imaging techniques allow visualizing blood flow maps inside the cardiac chambers. So far, the three main cardiac vector blood velocity imaging schemes are: CMR, already used in the clinical setting and it is considered the gold standard to carry out quantitative examinations of the cardiac blood flow [3]; Echo-PIV, it has been used in research studies to quantify and characterize the normal vortex in the cardiac LV [21]. *Color Doppler VFM*, it is completely non-invasive since only B-mode and color Doppler echocardiographic images are used to estimate two-dimensional velocity maps. Color Doppler CFM has been used to carry out measurements of the vortex in the cardiac blood flow [13]. The existing vector blood velocity techniques are described in the following paragraphs.

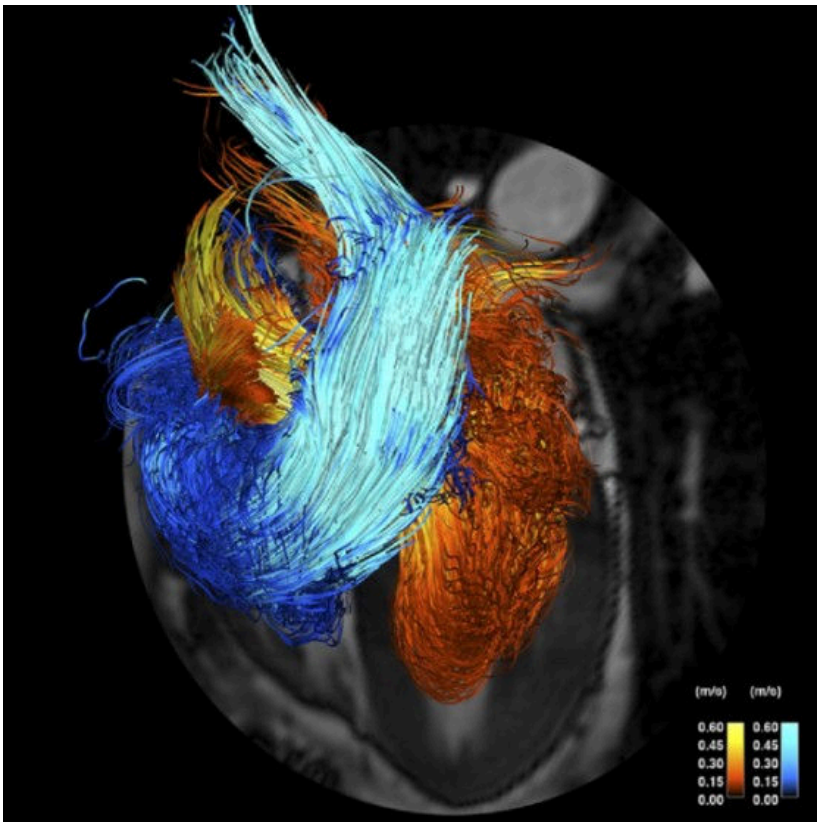

Fig. 2.6 - *Cardiac magnetic resonance path lines:* Color flow stream represent blood particles velocities in different phases of the cardiac cycle [4].

2.3.1 Cardiac magnetic resonance (CMR)

The CMR imaging technique can resolve blood flow velocities in any direction in the *Cartesian* coordinate system. This means the three velocity components of a particle can be estimated [4]. This technique does not use contrast agents, therefore it is considered completely non-invasive. The principle utilized to resolve the velocity maps relies in the measurement of bipolar gradients, the phase of the recorded signals changes as a function of blood velocity; such an association can be exploited to estimate the blood velocity. Although 3D blood velocities can be measured by means of CMR, several heart beats are usually combined to draw better quality data. ECG is then required to match all sets of data used to obtain one velocity estimate; also, respiratory gating is used to synchronize the acquired data.

The CMR imaging technique is popularly known as 4D–CMR; this is because it resolves the three velocity components throughout a time line [3]. Currently CMR offers a spatial resolution of 3 mm^3 and a temporal resolution of 20 fps. In average a procedure can be performed in about 20 minutes. The 2D or 3D velocity fields are usually represented by streamlines and path lines because of the intuitively delivered interpretation (see Fig. 2.6). Quantitative measurements are commonly applied on 2D views extracted from the 3D data. Parameters such as relative pressure field and turbulent kinetic energy are calculated using these velocity fields.

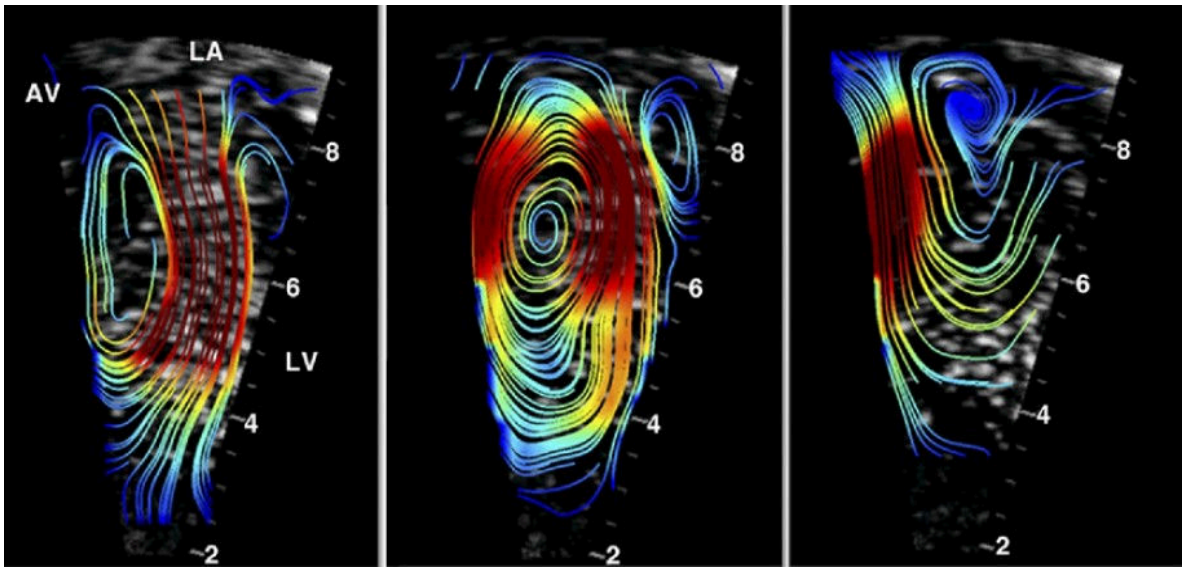

Fig. 2.7 - *Cardiac blood flow stream lines obtained using echo-PIV* [4].

The 4-D CMR velocity acquisition technique is capable of displaying the multidirectional blood flow that is supposed to be consistent from heart-beat to the next one. An important inconvenience of the CMR technique is the high cost of the MRI equipment, which ranges in the millions of dollars per device; additionally, CMR entails a complex instrumentation, one single examination can take about 25 min. Reconstructed movies are not delivered in real time, but rather obtained off-line by averaging hundreds of heart cycles, and therefore not small beat to beat variations can be determined.

2.3.2 Echocardiography particle image velocimetry (Echo–PIV)

Echo PIV is based on the particle image velocimetry (PIV) approach, which is a common and well known technique to estimate flow fields. PIV uses speckle tracking algorithms to estimate particle displacements from one frame to another in an image sequence [4]. This is accomplished by illuminating with a laser a flow seeded with particles, while the event is recorded by one or several cameras. Recorded images are post processed to track particles displacement frame to frame. Actually the PIV technique does not track particles displacement, but rather displacement patterns generated by a group of particles. In echo-PIV, B-mode echocardiography images are used to identify the blood flow streamlines by following the contrast agent displacement. The clinical implementation of the echo-PIV technique requires micro-bubbles to be injected in the bloodstream. Echo-PIV has been successfully employed in experimental and clinical studies. Cardiac blood flow streamlines obtained using echo-PIV are illustrated in Fig 2.7.

Even though echo-PIV seems very attractive because it utilizes B-mode echocardiographic images, it is also the cause for the main drawback related to this vector flow imaging scheme; since PIV uses sets of images to estimate the displacements, a high temporal resolution is most desirable to obtain accurate results. Current frame rates in echocardiography machines range from 50 to 100 frames per second. Such a temporal

resolution might not always be high enough to provide a proper input to the echo-PIV technique.

Another impairment featured by the echo-PIV technique is the use of contrast agents, *e.g.* micro-bubbles contrast agent side effects are not fully known yet. The last statement implies that echo-PIV should not be used in healthy patients, since any change on their condition could be attributed to its employment

2.3.3 Doppler ultrasound vector flow mapping (VFM)

Developed in the 80's, color Doppler ultrasound is an inexpensive and easily performed blood flow imaging technique. Although its accessibility and versatility, color Doppler only estimates axial velocities (lateral or angular velocities component are not estimated). Regardless this limitation, color Doppler has thrived as a diagnostic tool to detect abnormal cardiac blood flow behaviours.

Color Doppler VFM has been introduced as an alternative to estimate 2D blood velocities. VFM should be performed in a three chamber view to optimize its results; in the three chamber view the out of plane blood velocity are comparatively small all along the cardiac cycle, therefore the blood flow can be thought as two-dimensional. The VFM technique obtains the radial velocity component in the 2D cross sectional view, which combined with the color Doppler axial velocity, deliver the true 2D velocities at every range cell. The following techniques can achieve this same goal using different principles:

1. The *color Doppler VFM* approach introduced by Garcia *et al* [13] uses the color Doppler axial velocities and the boundary conditions imposed by the myocardial wall to find the angular velocity component using the mass conservation principle. The results obtained combining the mass conservation assumption and the boundary conditions obtained from speckle tracking enhance the accuracy of this technique.
2. The other *color Doppler VFM* approach has been introduced by Ohtsuki *et al* [22]. This approach assumes the flow along a radial line can be decomposed into a laminar motion and a vertical component with zero mean; the radial velocity component is estimated assuming that the vertical component satisfies the mass conservation equation along each radius.

2.3.4 Velocity vector flow imaging techniques remarks

The recently introduced cardiac blood flow imaging techniques allow for the visualization and analysis of multidirectional blood flow inside the heart. The importance of these techniques resides on their ability to provide further insights to a range of heart diseases by characterizing, verifying and interpreting the normal/abnormal cardiac blood flows. Three different approaches are available to perform cardiac blood flow - velocity vector imaging at this time; two of these techniques are ultrasound based while the other one uses MRI imaging. Table 2.1 presents a comparative summary of these three imaging techniques.

Table 2.1 : Comparison among cardiac blood flow visualization technologies

Cardiac blood flow visualization techniques	Phase Encoded CMR	Echocardiography	
		Echo-PIV	Color Doppler - VFM
Resolution and coverage relative to all 3D of space	Good spatial resolution in all 3D or in 2D in shorter acquisition times; unrestricted access	Good spatial resolution in 2D planes, and in multiple planes if required	High spatial resolution in 2D;good resolution in 3D
Coverage relative to all 3-directional components of velocity	All 3 can be acquired, or 2, or 1, through a plane placed in any orientation	Both in-plane components represented but not the throughplane	Only the 1 component directed to or from the transducer is currently measurable clinically
Temporal resolution	Typically 20–50 ms, each phase is calculated from acquisition from many heart cycles	High temporal resolution (4–20 ms), allows assessment of velocity fields even during brief isovolumetric contraction and relaxation phases over few heartbeats	Good temporal resolution in 2D (4–20 ms), relatively low in 3D
Scan time	Long (5–20 min) for a dataset covering all 3D and all 3-directional components but seldom real-time	Both scan time and offline analysis can be done over few heartbeats in minutes	Rapid scan times, real-time visualization
Breath-Holding	Breath-hold used for short, unidirectional velocity acquisitions, or diaphragm navigation for long acquisitions during free breathing	Imaging relatively easier during breath-hold but also possible during respiration	Not required
Low-velocity accuracy	Low velocities are measurable but less accurate if high velocities also have to be measured	Well-visualized	May be underestimated or affected by noise
High-velocity accuracy	Measurable up to the chosen VENC limit, but only where a stream or jet core is wide enough to include whole voxels	May be underestimated	Well-resolved within aliasing limit
Application	Flow visualization and measurement of volume flow through all cardiac chambers and large vessels	Flow visualization through all cardiac chambers, aortic flow evaluation may require use of transesophageal echocardiography	
Implanted devices	Metal stents or valve rings cause local artifacts; most pacemakers rule out MRI	Flow can be visualized through implanted cardiac devices, and in the presence of pacemakers and defibrillators	

Echo-PIV = echocardiography particle imaging velocimetry; CMR = cardiac magnetic resonance imaging; VENC = velocity encoding.

2.4 Color Doppler VFM - limitations and motivation

Color Doppler VFM assumes the cardiac blood flow is two-dimensional; such a supposition induces an error of about 15% on the velocity estimates in comparison to CMR. Given that cardiac blood velocities can only be approximated to be two-dimensional in the three chamber view, accuracy of the color Doppler VFM technique strongly depends on the echocardiography operator. The accuracy of color Doppler VFM is also depends on the quality of the color Doppler velocity information used as an input. The low temporal resolution and potential aliasing displayed by color Doppler represent an important drawback to the color Doppler VFM approach.

Although the young state of the color Doppler VFM technique, such an approach remains an interesting option to map the intraventricular hemodynamics. The current momentum reached by ultrafast ultrasound should help solving flaws as the low frame rates obtained with color Doppler echocardiography.

The motivation of the research project summarized in this report was to assess an ultrafast echocardiography approach and extend the Nyquist velocity range. We hope that enhancing these two echocardiography features will have a positive impact on the color Doppler VFM technique.

In this chapter, the anatomy and hemodynamics of the heart have been portrayed. Also, the echocardiography and other cardiac imaging techniques have been introduced, among these the echo PIV and color Doppler VFM, which are two vector flow imaging techniques that could benefit from higher echocardiography frame rates; particularly, the color Doppler VFM technique could benefit from an extended color Doppler velocity range, and at the same time could complement the lack a vector flow imaging application in echocardiography.

The next chapter introduces ultrasound imaging and its functioning principles. Notions such as, piezoelectricity, beamforming, radiofrequency signal demodulation, Doppler velocity estimation and other ultrasound related topics might be useful for readers that are not familiar with ultrasound imaging. The technical background presented in the following chapter occasionally addresses specifically the cardiac echo approach; this is the case for the section that introduces phased array transducers, which are solely used in echocardiography. All the other concepts presented in chapter 3 are generally extensible to any ultrasound imaging application.

Bibliography

[1] F. Mehregan, *et al.*, "Doppler vortography: A color Doppler approach to quantification of intraventricular blood flow vortices," *Ultrasound in medicine & biology,* vol. 40, pp. 210-221, 2014.

[2] O. College. Available: http://www.quickiwiki.com/en/Heart

[3] M. Markl, *et al.*, "Comprehensive 4D velocity mapping of the heart and great vessels by cardiovascular magnetic resonance," *Journal of Cardiovascular Magnetic Resonance,* vol. 13, pp. 1-22, 2011.

[4] P. P. Sengupta, *et al.*, "Emerging trends in CV flow visualization," *JACC: Cardiovascular Imaging,* vol. 5, pp. 305-316, 2012.

[5] S. Cimino, *et al.*, "*In vivo* analysis of intraventricular fluid dynamics in healthy hearts," *European Journal of Mechanics-B/Fluids,* vol. 35, pp. 40-46, 2012.

[6] S. D. Solomon, *Essential Echocardiography: A Practical Guide With DVD*: Springer Science & Business Media, 2007.

[7] I. Edler and K. Lindström, "The history of echocardiography," *Ultrasound in medicine & biology,* vol. 30, pp. 1565-1644, 2004.

[8] S. White. (16/02/2015). *Transesophageal Echocardiography (03/09/2004 ed.)*. Available: http://www.sw.org/HealthLibrary?page=Transesophageal%20Echocardiography

[9] W. L. Henry, *et al.*, "Report of the American Society of Echocardiography Committee on nomenclature and standards in two-dimensional echocardiography," *Circulation,* vol. 62, pp. 212-217, 1980.

[10] *Atlas of Echocardiography*. Available: http://www.yale.edu/imaging/echo_atlas/views/apical_2c.html

[11] C. M. Otto and A. S. Pearlman, "Textbook of clinical echocardiography," 2004.

[12] R. B. Thompson and E. R. McVeigh, "Fast measurement of intracardiac pressure differences with 2D breath-hold phase-contrast MRI," *Magnetic resonance in medicine,* vol. 49, pp. 1056-1066, 2003.

[13] D. Garcia, *et al.*, "Two-dimensional intraventricular flow mapping by digital processing conventional color-Doppler echocardiography images," *Medical Imaging, IEEE Transactions on,* vol. 29, pp. 1701-1713, 2010.

[14] D. Tipster, "Mitral Regurgitation Diagnosis," ed, 2015.

[15] M. Lewandowski, *et al.*, "Research & Medical Doppler platform," *Acoustics 2012 Nantes,* 2012.

[16] A. C. Perrino and S. T. Reeves, *A practical approach to transesophageal echocardiography*: Lippincott Williams & Wilkins, 2008.

[17] N. J. Ashley EA. (2004). *Cardiology Explained*. Available: http://www.ncbi.nlm.nih.gov/books/NBK2215/

[18] H. Hasegawa and H. Kanai, "High-frame-rate echocardiography using diverging transmit beams and parallel receive beamforming," *Journal of Medical Ultrasonics,* vol. 38, pp. 129-140, 2011.

[19] H. Blessberger and T. Binder, "Two dimensional speckle tracking echocardiography: basic principles," *Heart,* vol. 96, pp. 716-722, 2010.

[20] C.-m. Tam, "Application of Echocardiography in Clinic Practice," *Medical Bulletin,* vol. 12, 2007.

[21] G.-R. Hong, *et al.*, "Characterization and quantification of vortex flow in the human left ventricle by contrast echocardiography using vector particle image velocimetry," *JACC: Cardiovascular Imaging,* vol. 1, pp. 705-717, 2008.

[22] S. Ohtsuki and M. Tanaka, "The flow velocity distribution from the Doppler information on a plane in three-dimensional flow," *Journal of visualization,* vol. 9, pp. 69-82, 2006.

Chapter 3

Ultrasound imaging background

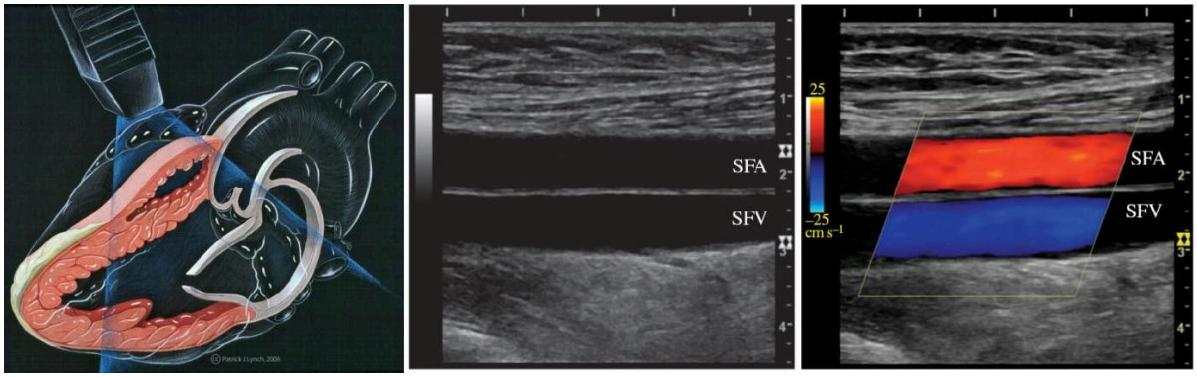

Fig. 3.1 – *Left panel:* Ultrasound echocardiography examination. *Center Panel:* B-mode image of the superficial femoral artery and superficial femoral vein. *Right panel:* Doppler ultrasound image of the femoral artery and vein.

Ultrasound imaging has been used for over half a century. The Austrian neurologist Dr. Karl Theo Dussik was the first to apply ultrasound as a medical diagnostic tool; back in the 1940s, Dr. Dussik used ultrasound to image the human brain, nowadays, ultrasound is the most widely used medical imaging technology. Ultrasound is completely portable and reasonably inexpensive when compared to other imaging modalities, *e.g.* MRI or CT scan. Additionally, ultrasound uses non-ionizing radiation and it can perform a wide variety of real time dynamic imaging examinations, from obstetrics to cardiovascular assessments [1, 2]. The working principle of ultrasound imaging allows carrying out examinations such as echocardiography (see Fig. 3.1 – left panel), B-mode vascular imaging (see fig. 3.1 – center panel) and color Doppler imaging (see fig. 3.1 - right panel). When conducting color Doppler imaging, B-mode images are combined with red and blue images to represent the dynamic transit of blood. Most ultrasound systems can currently perform both B-mode and color Doppler imaging in real time [3].

This chapter introduces the technical aspects of ultrasound imaging. The piezoelectric principle is introduced in the first section. Afterwards, the properties of echocardiography phased array transducers are presented. In the next section, a basic explanation of the interaction between ultrasound and soft tissues is given. Following, the conventional ultrasound image formation method and some ultrasound signal processing tactics are described. Ultrasound imaging quality quantification is explained in the next section. Finally, the various Doppler ultrasound imaging methods are addressed, *e.g.* continuous wave Doppler, pulsed Doppler and color Doppler imaging.

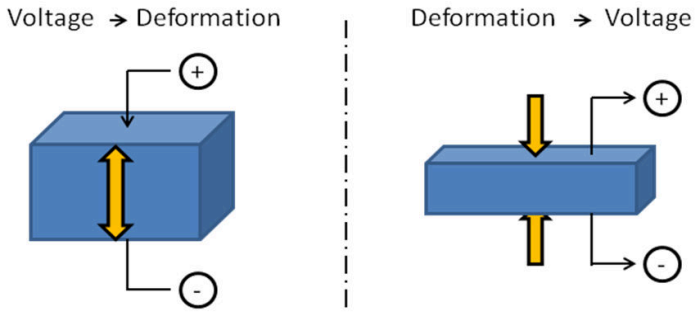

Fig. 3.2 - *The piezoelectric effect*. *Left panel*: Piezoelectric materials deform upon the application of a voltage over opposing faces. *Right panel:* Piezoelectric materials generate a voltage when opposing faces experience mechanical strain.

3.1 The piezoelectric effect (Ultrasound wave generation-acquisition)

Piezoelectricity is the underlying working principle of ultrasound imaging. This particular property of some specific materials consists in a reversible process that converts electricity into mechanical strain and vice versa (see Fig. 3.2) [4]. The Greek meaning of piezoelectricity is *electricity resulting from pressure*. Piezoelectricity was discovered to be a property of quartz crystals by Jacques and Pierre Curie in 1880; nowadays multiple materials have been confirmed to display such a property, *e.g.* synthetic ceramics such as barium titanate and lead zirconate titanate (PZT), which is indeed the most common piezoelectric material used nowadays due to its elevated piezoelectric coefficient.

The electromechanical interaction that takes place in piezoelectric materials is crucial for ultrasound imaging. Piezoelectric materials can be used to generate acoustic waves or to detect acoustic echoes [5] (see Fig. 2.3). Piezoelectric materials can be tailored in different geometries depending on their intended application; particularly, ultrasound imaging frequencies are required to be in the MHz range. Piezoelectric elements are used in ultrasound imaging to transmit mechanical waves (ultrasound pulses) into the soft tissues and also to record echoes reflected from the heterogeneities in the medium.

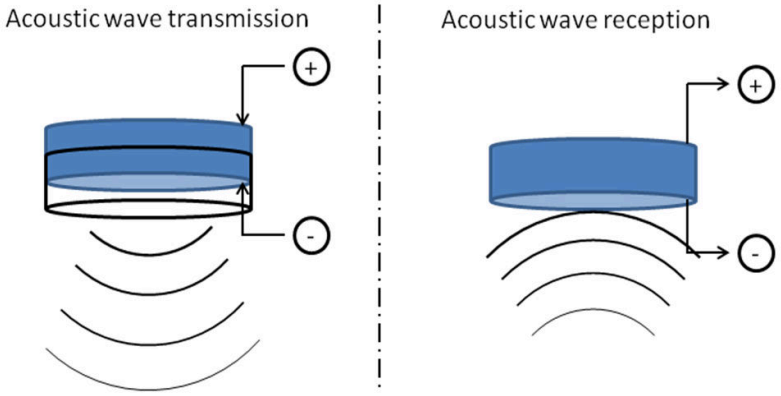

Fig. 3.3 - *Piezoelectric materials are suitable either to transmit or record mechanical ultrasound waves. Left panel:* A piezoelectric disc transmits an ultrasound mechanical wave upon an electric stimulus. *Right panel:* A piezoelectric disc generates an electric current while it vibrates due to the impact of a reflected echo over one of its faces.

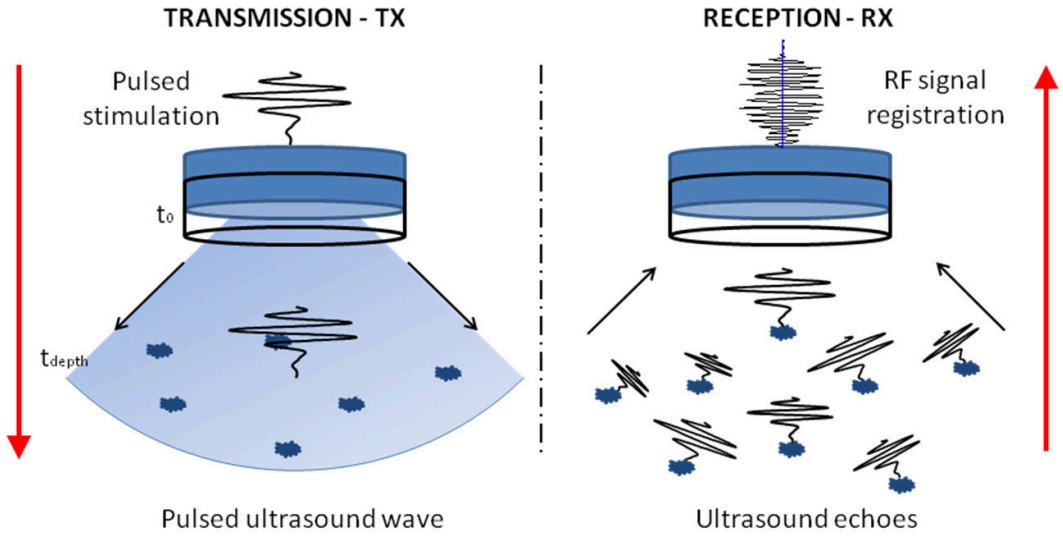

Fig. 3.4 – *Left panel:* Mechanical waves can be transmitted using piezoelectric elements. This is done by exiting with electric currents two opposed faces on the piezoelectric element. *Right panel:* Mechanical waves can be detected using piezoelectric elements. Oscillations induced by external waves (*e.g.* ultrasound echoes) result in electrical currents produced by the piezoelectric element.

The oscillation of a piezoelectric element occurs when an electric impulse is applied to its opposite faces; the electric impulses used in ultrasound imaging feature a Gaussian shape and their duration ranges in the nanosecond range. Oscillations stemming from the piezoelectric elements create acoustic waves that propagate through the surrounding medium. Following to the ultrasound wave transmission, reflected echoes return from the medium and hit back the piezoelectric element; the reflected echoes trigger oscillations and therefore the electrical voltages are generated due to the piezoelectric effect. The electrical voltages generated by the piezoelectric element enables to record echoes as digital radiofrequency signals (see Fig. 3.4 – right panel).

3.2 Ultrasound imaging linear arrays

Ultrasound array transducers are composed of multiple piezoelectric elements. Ultrasound array transducers can be classified according to their application: *vascular, abdominal, cardiac,* among others. The three ultrasound linear arrays that are available in the clinical setting are:

Linear probes (vascular array): ultrasound linear probes exhibit high frequencies (~5.5 MHz) and large footprints (~4 cms). These linear probes are well suited to image shallow structures such as superficial vessels.

Curvilinear probes: ultrasound curvilinear probes feature wide footprints (~5 cms) and low frequencies (~2.6 MHz). These linear probes are special to perform deep scan in the abdominal area, *e.g.* used to conduct liver, renal and obstetrics scans.

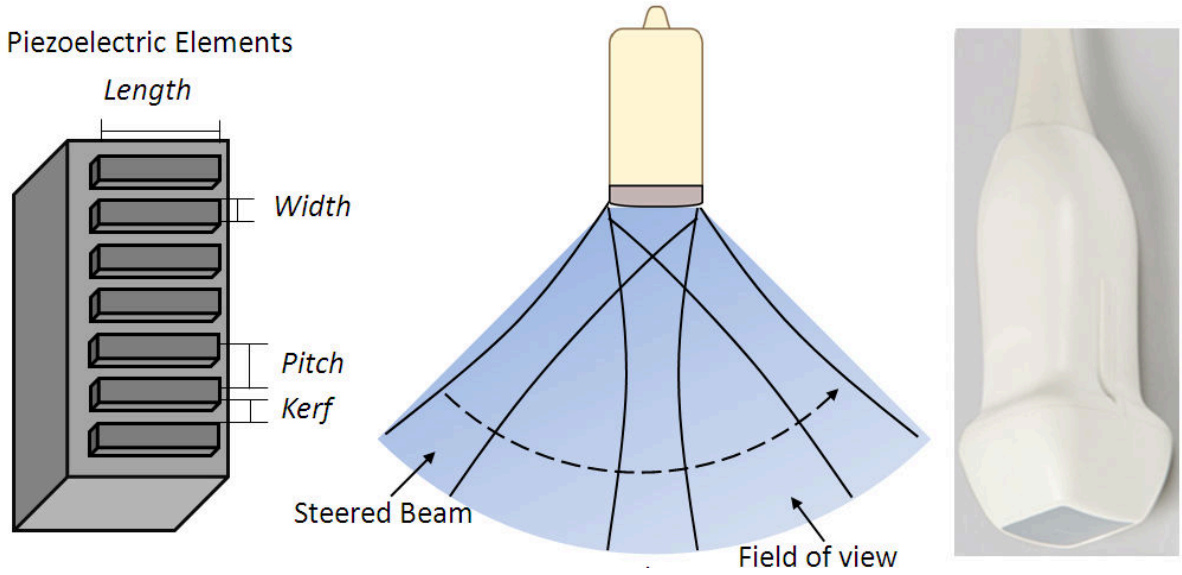

Fig. 3.5 – *Phase arrays. Left panel:* Linear array geometrical properties. *Center panel:* Steered ultrasound beams generated by a phased array transducer. *Right panel:* Cardiac phased array probe.

Phased array probes: phased arrays are especially suited to scan deep into the heart (~15 cms). They feature small footprints (~2 cm) to allow ultrasonic energy pass through the intercostal gaps (see Fig. 3.5 – right panel) and their center frequency is rather low (~2.5 MHz).

Linear arrays geometrical properties have to be considered to accomplish an optimal design: the piezoelectric elements geometry (length, height and width) define the central frequency of the ultrasound probe (see Fig. 3.5 – left panel). Also, the pitch and the kerf (defined by the elements arrangement) are key properties to establish the spatial resolution and steering capabilities of an ultrasound transducer (see Fig. 3.5 – center panel).

Phased arrays and curvilinear arrays generate sectorial images (see Fig. 3.5 – center panel). Phased array can be electronically triggered to transmit steered ultrasound beams (see Fig. 3.5 – center panel); the steering capability allows to insonify sectorial ROIs through the ribs, therefore the importance of phased arrays for echocardiography imaging.

3.2.1 Phased arrays delay law

Ultrasonic phased arrays incorporate multiple piezoelectric elements that can be independently activated. Microseconds lags are introduced between the excitation of piezoelectric elements (delay-laws) to modify the final phased array radiation pattern (RP); the delay law in Fig. 3.6 activates the two elements in the middle first, then a hyperbolic sequence is followed to activate the elements located towards the extremes. As opposed to the eight elements included in Fig. 3.6, actual phased arrays incorporate 64 to 128 elements.

3.2.2 Single elements and phased arrays radiation patterns

As it was previously explained, phased arrays radiation patterns can be modified by tailoring the delay laws; furthermore, phased arrays radiation patterns evolve as they travel

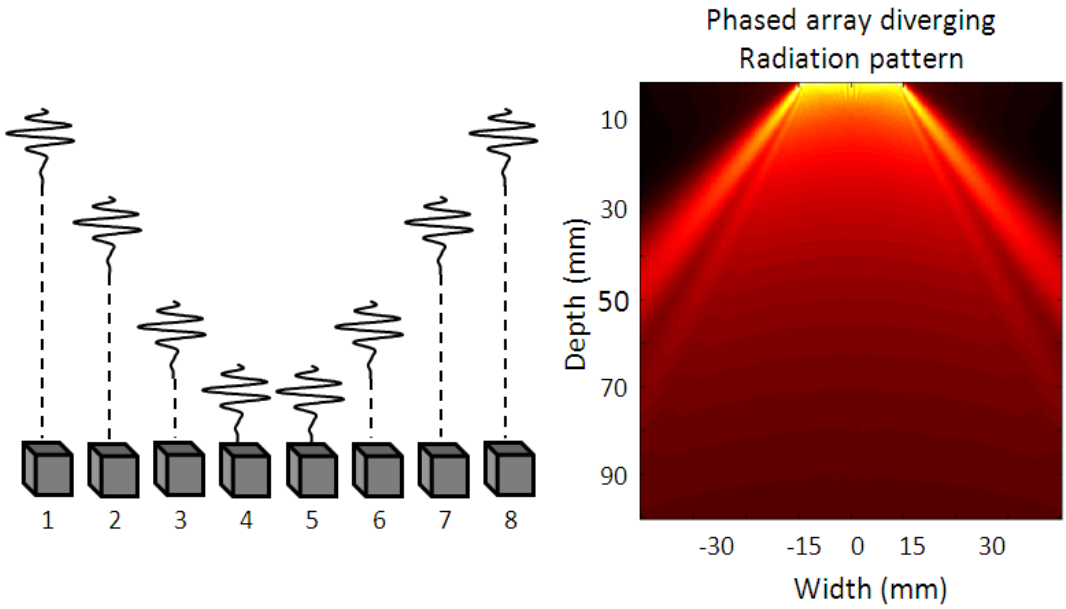

Fig. 3.6 – *Left panel:* delay law applied to 8 piezoelectric elements in a phased array. *Right panel*: Diverging RP of a phased array with 64 elements. The simulation was conducted using the model proposed by Wooh *et al*, see equation (3.3).

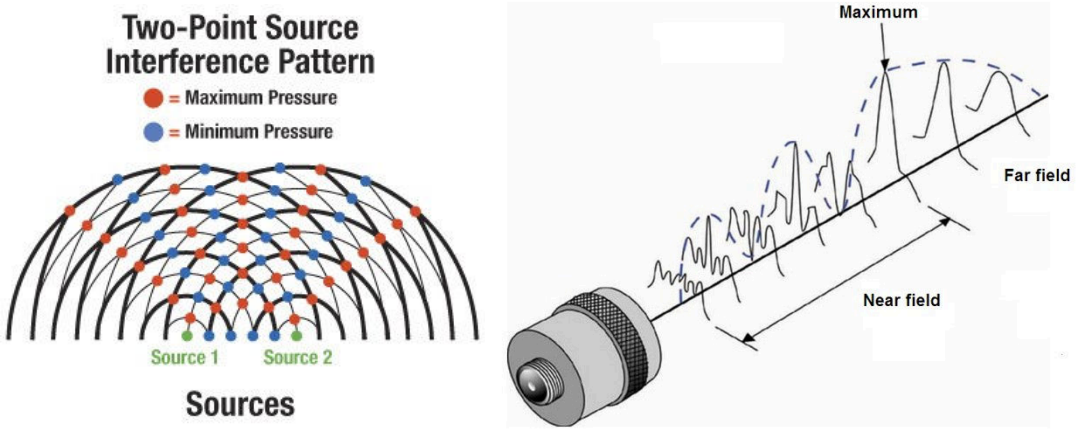

Fig. 3.7 – *Left panel:* Constructive and destructive interactions encountered between two waves simultaneously transmitted. *Right panel:* Near and far field regions in a single piezoelectric transducer radiation pattern (source: http://www.physicsclassroom.com and https://www.nde-ed.org).

through the medium. The radiation pattern development obeys to the constructive and destructive interference among the ultrasound waves emitted by each piezoelectric element in the phased array (see Fig. 3.7 – right panel).

As per phased arrays, single piezoelectric elements also feature their own radiation pattern (see Fig. 3.7 – right panel). The radiation pattern *near field* involves the spatial region where abrupt intensity variations occur (see Fig. 3.7 – right panel); on the other hand, the radiation pattern *far field* concerns the spatial region where acoustic pressure smoothly declines (see Fig. 3.7 – right panel). A precise method to simulate the far field radiation pattern of single piezoelectric element has been proposed by Selfridge *et al* [6],

$$p(r,\theta) = \frac{p_0 \omega}{i(\lambda)^{1/2}} e^{2j\pi r/\lambda} D_b(\theta), \tag{3.1}$$

where p is the pressure value of the RP at a given polar coordinate (r, θ), w and λ are respectively the angular frequency and the wavelength of the propagating wave, and $D_b(\theta)$ is the angular response of the single element in the far field. The angular response can be defined as,

$$D_b(\theta) = \frac{sin\left(\pi\omega/\lambda sin(\theta)\right)}{\pi\omega/\lambda sin(\theta)} cos\theta, \tag{3.2}$$

The model proposed by Selfridge *et al* was used in chapter four to investigate phased arrays steering capabilities when diverging radiation patterns are transmitted. Selfridge model can be used to estimate a phased array radiation pattern, this is done by summing up the radiation patterns of independent piezoelectric elements lined up one next to the other as in a phased array.

Additionally, the model proposed by Wooh *et al* in equation (3.3) [7-10] was implemented to simulate phased arrays acoustic pressure fields (see Figs. 3.6 and 3.9). In the frequency domain, the 2D pressure distribution generated in the *far field* by a 1-D uniform linear array is given by (see Eq. 4.14 p 77 in [10])

$$P(r,\theta,\omega,t) = \sum_{n=1}^{N} W_n e^{i\omega\Delta\tau_n} \left[\rho c v_0(\omega) \sqrt{\frac{2}{i\pi}} kb\, D_b(\theta) \frac{e^{ikr}}{\sqrt{kr}} e^{-ikx_n sin\theta} \right] e^{-i\omega t}, \tag{3.3}$$

where $i = \sqrt{-1}$, t is time, ω is the angular frequency, ρ is the medium density and $k = \omega/c$ is the wavenumber. In this equation, it is assumed that the N individual elements act as pistons whose normal velocity in the frequency domain is $v_0(\omega)$. The weights W_n applied to these N elements represent the apodization values. Because no apodization was considered in our study, $W_n = 1, \forall n$. The function $D_b(\theta)$ is the directivity function of an individual element of width $2b$ and is described later (Eq. 8). The delay laws $\Delta\tau_n$ for circular diverging beams are given by Eq. (3.2) and x_n $(n = 1 \ldots N)$ is the centroid location of the n^{th} element.

In order to simulate the radiation patterns and pressure field of phased array with the models previously described, each element was discretized into N number of segments to calculate its individual far field radiation pattern or pressure field; afterwards, the linear array radiation patterns or pressure fields were obtained by superposing the results corresponding to each single element.

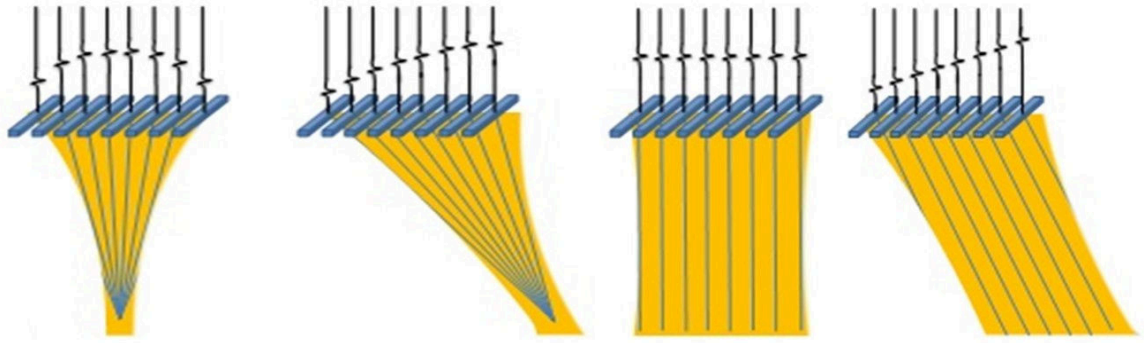

a. b. c. d.

Fig. 3.8 – *Schematic representation of non-steered and steered ultrasound beams. Panel a:*Transmission of a non-steered focused ultrasound beam. *Panel b:*Transmission of a steered focused ultrasound beam. *Panel c:* Transmission of a non-steered plane wave. *Panel d:* Transmission of a steered plane wave (source: www.ultrasonix.com).

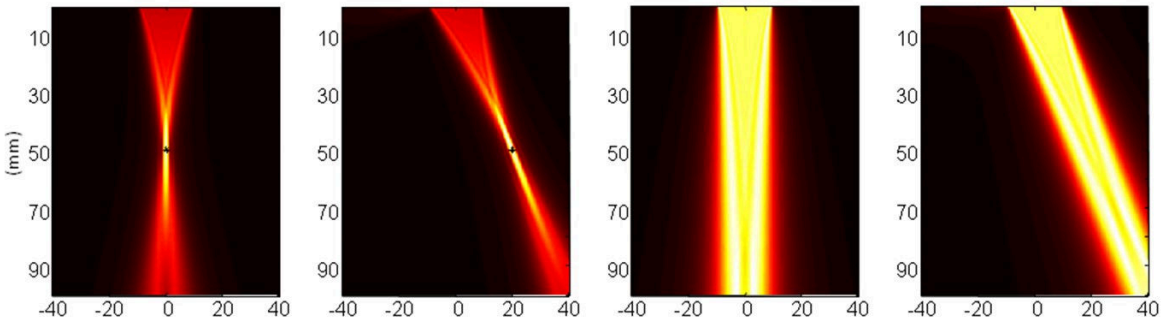

a. b. c. d.

Fig. 3.9 – *Simulation of non-steered and steered ultrasound pressure fields. Panel a*: Transmission of a non-steered focused ultrasound beam . *Panel b:* Transmission of a steered focused ultrasound beam. *Panel c:* Transmission of a non-steered plane-wave. *Panel d:* Trans of a steered plane wave.

3.2.3 Phased arrays beam steering

The piezoelectric elements of a phased array are depicted as linearly arranged blue blocs in Fig. 3.8. Transmission of mechanical waves with many piezoelectric elements is feasible by introducing delay laws. The sequential excitation principle facilitates to control the directivity of the resulting radiation pattern. The use of different delay laws during the transmission event can create diverse ultrasound RP, *e.g.* a delay law may result in a convergent ultrasound radiation pattern (see Fig. 3.8 – panel a). Phased arrays can also transmit oriented ultrasound beams by using non-symmetric delay laws (see Fig. 3.8 – panel b); the technique of transmitting oriented ultrasound beams is known as beam steering; in conventional echocardiography the sectorial ROI is swept by transmitting steered ultrasound beams (see Fig. 3.5 – panel b).

Controlling the delay laws seeded to the phased array results in different types of ultrasound fields; as an illustration, a plane wave can either be transmitted parallel to the range direction or in a steered orientation (see Fig. 3.8 - panel c and d). As with plane waves, diverging ultrasound waves can be transmitted and steered.

The phased array steering capability is bounded by the appearance of undesirable high intensity ultrasound beams known as grating lobes. The phased arrays steering limits have been extensively investigated in order to avoid grating lobes [11]. It has been proved that reducing the phased array pitch enhances steerability; the pitch in phased arrays is half the wavelength of the ultrasound system ($\Delta x = \frac{\lambda}{2}$), this feature provides a wide steering range. For instance, if the phased array pitch and center frequency are known, then the steering range can be estimated with equation (3.4) (only valid for plane wave transmissions) [11].

$$\beta_{max} = sin^{-1}\left(\frac{\lambda}{\Delta x} - 1\right) \tag{3.4}$$

The following example is presented to give an idea of a phased array steerability: if the pitch is assumed to be $\Delta x = 0.3$ mm and the wavelength is supposed to be $\lambda = 0.6$ mm (2.5 MHz center frequency, which is typical in cardiac phased arrays), then the steering range is $[-60°: 60°]$. Formula (3.4) assumes the transmission of plane waves, so it cannot be extended to establish the steering limits for other radiation patterns, *e.g.* focused or divergent ultrasound beams.

3.3 Ultrasound waves interaction with soft tissues

Understanding the interaction of ultrasonic energy with human tissues is of great importance to generate ultrasound images. Parameters such as propagation velocity, acoustic impedance and attenuation need to be considered in order to process recorded ultrasound echoes (digitized RF signals). The topics mentioned before are reviewed in the following paragraphs.

3.3.1 Ultrasound propagation velocity and acoustic impedance

The wave propagation velocity is the speed at which an ultrasound wave moves through a given material. The wave propagation velocity is affected by both the mass density ρ and the medium compressibility k,

$$c = \sqrt{\frac{1}{k\rho}} \tag{3.5}$$

Ultrasound waves generate oscillatory movements in the medium particles as they propagate; in this regard, materials with heavier particles will require more energy to start and keep conveying ultrasound waves. The compressibility of a material determines how easy it can be deformed. The ultrasound propagation velocity is affected by compressibility because of the material ability to transfer energy, *e.g.* bone or steel; given that energy can be transferred with very small particles movements, ultrasound waves travel faster through these materials.

Since medical ultrasound imaging aims to image the human body, it is important to know the ultrasound propagation velocity through soft tissues. Given that the ultrasound propagation velocity differs in mediums such as liver, fat, amniotic fluid and other soft tissues, an average propagation velocity is used in clinical ultrasound machines; this value is widely accepted to be 1540 m/s.

The acoustic impedance is another important property for the ultrasound interaction with a given medium. Such a property indicates the resistance of particles in the medium to be disturbed by ultrasonic waves. The specific acoustic impedance of a medium can be written in terms of its density and ultrasound propagation velocity:

$$Z = \rho c \tag{3.6}$$

3.3.2 Ultrasound waves attenuation

Ultrasound waves get attenuated as they travel through a given medium. The main factors responsible for ultrasound energy attenuation in heterogeneous mediums are:

Waves scattering: Incoherent process in which mechanical waves are deviated from its original transmission path.

Energy absorption: Makes reference to the kinetic energy that is converted into heat due to mechanical wave's expansion and rarefaction through the conducting medium [12].

The center frequency of the ultrasound probe plays an essential role on ultrasound attenuation. Energy attenuates in shorter distances as the ultrasound wave center frequencies increases; in this context, the ultrasound probe frequency must be chosen depending on the depth to be scanned. Attenuation follows an exponential trend dependent on the scanned depth and the wave center frequency, therefore the ultrasound amplitude decay model is,

$$\mathrm{A}(r, f_c) = \mathrm{A}_0 e^{-\alpha f_c r/8.7} \tag{3.7}$$

where A is the amplitude decay at a certain depth, r is the travelled depth, f_c and A_0 are the wave central frequency and the original amplitude, α is the attenuation coefficient ($\alpha = a f_c$) in which a is the *material frequency-dependent attenuation*; in soft tissues and blood, typical values of a are respectively 0.7 and 0.2 dB/MHz/cm.

3.4 Ultrasound imaging using the pulse-echo principle

The "pulse-echo" principle is the basis of ultrasound imaging. Small ultrasound bursts are transmitted into the tissue and then the backscattered echoes are recovered to produce images. The following paragraphs give a general explanation of how ultrasound images are reconstructed.

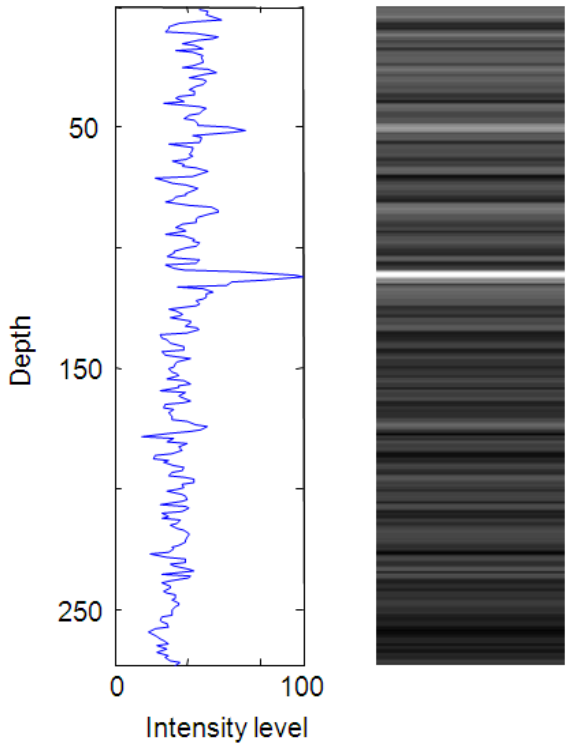

Fig. 3.10 – Echographic *A-line. Left-panel:* The envelope of an echo signal is presented as a function of depth. *Right panel:* The envelope of an echo signal is presented as a gray-scale column.

3.4.1 *A-Lines, B-mode* and *color Doppler* ultrasound

The A-line

The A-line is the most basic form of echographic image; echo-signals are recorded following the ultrasound beam transmission. The envelope of the echo-signal is then displayed in a grey level column; pixels are depicted light or dark according to the intensities of the signal envelope (see Fig. 3.10).

B-Mode imaging

B-mode images are obtained putting together multiple A-lines reconstructed one at a time. In cardiac imaging, the sectorial ROI is swept with steered focused ultrasound beams that are transmitted one after the other [13]; putting together a B-mode image requires transmitting about one hundred ultrasound beams to generate the same number of A-lines.

Color Doppler ultrasound imaging [1, 14, 15]

It is an ultrasound modality to detect velocities and blood flow direction. In cardiac applications it helps in visualizing the blood dynamics within the heart. Further explanation on the reconstruction of Doppler images is given in section 3.5.

3.4.2 Time gain compensation

Time gain compensation (*TGC*) is the first process that takes place on the received echo signals. Such a process aims to rectify the attenuation experienced by the transmitted ultrasound pulses. Received echoes are amplified depending on the depth they emanate from. In order to create a *TGC* function, the two following two assumptions are made:

1. The attenuation coefficient is a constant from start to finish of the ultrasound path, $\mu(x) = \bar{\mu}$. As long as there are no bones in the path, this approximation happens to be very precise.
2. The propagation velocity through the soft tissue is a constant, $c(x) = \bar{C}$. T he very little variations make of this a reasonable assumption.

The compensated signals obtained with the *TGC* gain function can be written as,

$$S_N(t) = X(t)\, TGC_N(t) \tag{3.7}$$

Where $X(t)$ are the recorded signals before compensation and $TGC_N(t)$ is the gain compensation function. The ideal *TGC* function can be defined as,

$$TGC(t) = \frac{1}{\left[\prod_{n=0}^{N-1} T_{(n-1,n)} T_{(n,n-1)}\right]} e^{+\bar{\mu}\bar{C}t} \tag{3.8}$$

where $\prod(t)$ are empirical continuous gain functions set by the user. The ideal *TGC* parameters are already preset in clinical ultrasound machines; however modifications can be performed in real time by the operator to optimize the image quality.

3.4.3 Ultrasound Image formation (Beamforming)

Ultrasound systems use the "pulse-echo" principle to create B-mode images (B stands for brightness). The image formation process involves both the transmission and reception stages. During the transmission stage, a pulsed ultrasound beam is transmitted using a linear array (see section 3.2. for an explanation); such a process is known as *transmit-beamforming*.

Pulsed ultrasound beams travel through the tissue at the ultrasound propagation velocity; part of the wavefront energy is reflected back to the transducer (echoes) due to the heterogeneities of the medium, some energy continues to penetrate deeper and some energy gets attenuated. The echoes reflected back to the transducer are recorded as RF signals by each piezoelectric elements; high intensity values in the RF signal are the result of highly reflective features in the tissue (see Fig 3.11 – panel a.) [16]. Reflected waves (echoes) can be observed when RF data are observed as an image, usually 64 to 128 RF signals are simultaneously recorded with a phased array (see Fig. 3.11 – panel b).

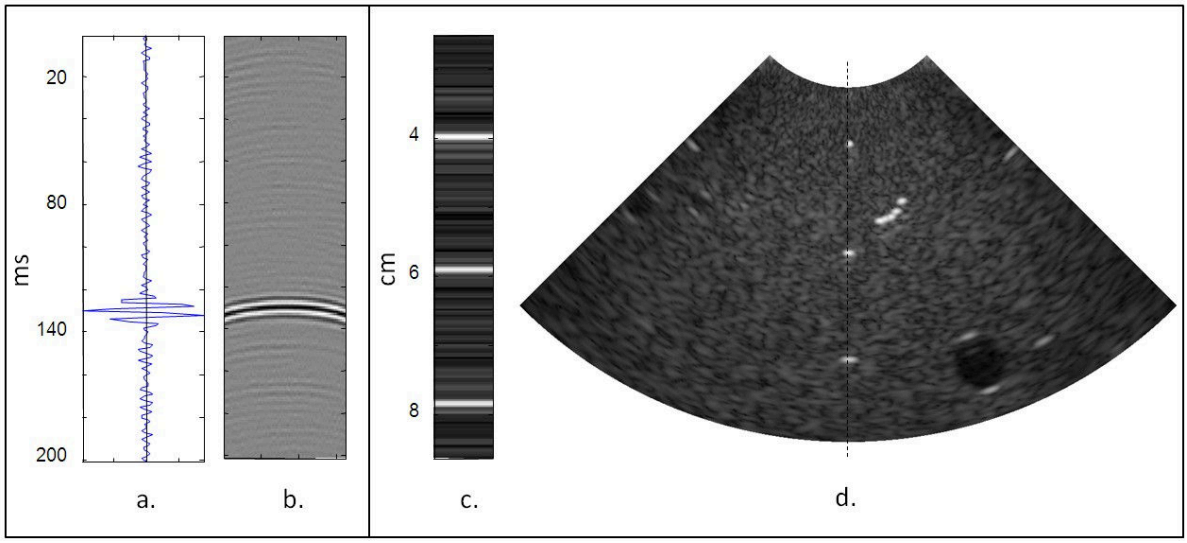

Fig. 3.11 – Beamforming process. *Panel a:* Single ultrasound RF signal. The high intensity echo in the RF signal corresponds to a highly reflective feature into the tissue. *Panel b:* RF signals ensemble. The image depicts echo-waves that are recorded by a phased array. *Panel c:* A-line. Echo-signals are delayed and summed to create A-lines. *Panel d:* B-mode sectorial image. Successive A-lines are put together to generate a B-mode sectorial image.

In conventional echocardiography a phased array transmits steered convergent wavefronts to sweep the interrogated ROI (see Fig. 3.5 – panel b). After each pulsed beam is transmitted, echoes are recorded and processed to create one single A-line; in this order of ideas the transmission and reception process needs to be iterated multiple times to generate one complete B-mode image.

Ultrasound transducers are used both to transmit pulsed ultrasound beams and record reflected echoes. In echocardiography, the transmission and reception processes last between one hundred to three hundred milliseconds (ms) depending on the interrogated depth. Transmission of ultrasound pulses takes a very small fraction of time within the whole transmission/reception process (less than one ms); on the other hand, reception of reflected echoes is performed all along the process. The reception time required to interrogate a given depth can be calculated with the following expression:

$$t = \frac{2r}{c} \tag{3.9}$$

where t is the recording time of echo signals, r is the interrogated depth and c is the ultrasound propagation velocity. The time provided by equation (3.9) includes both the time elapsed by the transmitted wavefront to reach a given depth in the interrogated ROI and the time elapsed by the echoes to travel back to the transducer; this round trip is known as *time of flight*. In pulsed ultrasound systems, the *time of flight* delimits the *pulse repetition frequency* (PRF), which is the amount of pulses transmitted every second.

In the *beamforming* process the *time of flight* is used to retrieve the echoes stemming from each spatial location in the ROI (each pixel in the image); RF data are

inspected under the assumption that every pixel in the image is a scatter, and then echoes values are identified and summed up for every pixel in the image. Because of the sequence of actions performed during the image formation process, the *receive-beamforming* algorithm is known as *delay-and-sum.*

As explained before, conventional echocardiography generates one A-lines at a time (see Fig. 3.11 – panel c), therefore, the *delay-and-sum* algorithm has to be performed many times to be generate a complete B-mode image (see Fig. 3.11 – panel d).

3.4.4 RF signals demodulation into IQ components

In ultrasound imaging reflected echoes are digitized as amplitude modulated radio-frequency signals. In order to accomplish an adequate RF signals digitization, the sampling frequency has to be set to at least twice the maximal signal modulation frequency (as established by the Nyquist-Shannon theorem). Registered RF data are time gain compensated and then beamformed; afterwards, the resulting data can be converted into complex baseband in-phase and quadrature (IQ) signals. IQ signals significantly reduce data size while keeping all the spectral information originally contained in the raw RF signals; the smaller data volume simplifies the ultrasound images processing, in particular when conducting color Doppler estimations.

RF signals are bandpass signals with a symmetric spectral representation (see Fig 3.12 – left upper panel); the frequency f_c corresponds to the ultrasound array center frequency and W is the probe associated bandwidth [17]. The RF signals demodulation process into IQ components includes three basic steps [18]:

Down mixing:

The down mixing procedure relocates the center frequency of the bandpass signals around the origin. The resulting signal is called the complex envelope and it is defined as,

$$\tilde{X}(t) = X_+(t)\exp(-i2\pi f_c t) \tag{3.10}$$

where $\tilde{X}(t)$ is the complex envelope and X_+ is the pre-envelope or analytic signal defined as,

$$X_+(t) \triangleq X(t) + i\hat{X}(t) \tag{3.11}$$

where $\hat{X}(t)$ is the Hilbert transform of the bandpass signal $X(t)$.

Low pass filtering

After the center frequency has been relocated around the origin (see Fig. 3.11 – bottom right), the complex envelope is low pass filtered to keep only the spectrum centered on the zero frequency, this means the cut-off frequency is $f_{cut} = W/2$. During the low pass filtering procedure, half of the signal energy disappears because half of the original

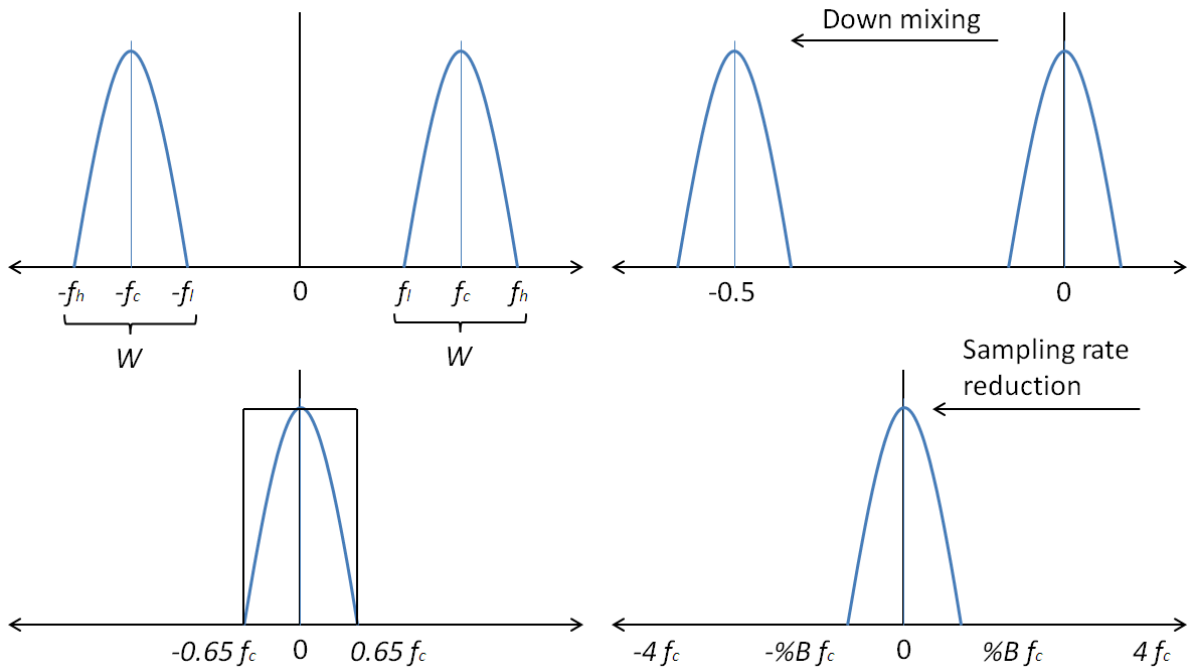

Fig. 3.12 – *Beamformed RF signal demodulation.* Original real beamformed RF signal spectrum (left-upper panel). Spectrum shifted to the origin (right-upper panel). Low pass filtered spectrum (left-lower panel). Re-sampled decimated spectrum (right-lower panel)

spectrum is removed. The resulting signals are multiplied by the square root of 2 to compensate for the energy lost.

Decimation

According to the Nyquist-Shanon theorem, the filtered complex envelope can be down sampled to twice the cut-off frequency used during the low pass filtering procedure. In ultrasound common bandwidths range between 60% to 70%, which allows decimating the complex envelope by a factor of 6; this means, only one sample out of six is kept, the rest are discarded. It is clear the decimation process is accountable for data volume reduction, which is one of the IQ demodulation advantages.

3.4.5 Compression and image display

In order to display an ultrasound image, the envelope $S(t)$ of the Beamformed signals must be extracted,

$$S(t) = \left|\tilde{X}(t)\right| \tag{3.12}$$

Once the envelope signal is available, a logarithmic compression is applied to compensate for the large difference in the amplitudes of reflected echoes from the scanned region. The

logarithmic compression reduces contrast irregularities among the regions in the image and permits to display both weak and strong intensity echoes in the same field of view. The logarithmic compression is performed as per the following equation,

$$B_{mode} = 20\log\big(S(t)\big) \tag{3.13}$$

Alternatively, some ultrasound machines use a gamma "γ" compression which has an equivalent effect in the B-mode images.

3.5 Temporal resolution (Frame rate)

The temporal resolution of an ultrasound imaging system is its ability to capture dynamic events, *e.g.* motion of the human heart. The temporal resolution of an ultrasound imaging system is usually quantified in frames per second (fps); in a conventional ultrasound system, the frame rate is established by the scanned depth, the ultrasound propagation velocity and the number of *A-lines* necessary to create one complete B-mode image,

$$\text{Frame Rate} = \frac{c}{2rN_{\text{A}}}, \tag{3.14}$$

Where N_{A} is the number of transmission per B-mode image (in conventional ultrasound imaging N_{A} is equal to the *A-lines* number required to create one B-mode image). The maximal ultrasound imaging frame rate is therefore delivered when the pulsed system reaches its maximum PRF.

3.6 Ultrafast ultrasound and coherent compounding

Ultrafast ultrasound is an alternative to increase the temporal resolution of ultrasound systems. Ultrafast ultrasound imaging uses non-focused ultrasound beams to insonify the interrogated field of view. In plane wave imaging, every transmitted wavefront gives rise to a whole image of the interrogated ROI; considering that only the image depth limits the pulsing cadency, plane wave imaging can reach very high frame rates, i.e. 15.000 fps in vascular imaging. On the other hand, since no focusing is performed on the range direction, substantially lower contrast and spatial resolution are evident drawbacks featured by this imaging approach. However, coherent compounding can be used to enhance both of these features; the coherent compounding scheme sums backscattered echoes gathered from multiple insonifications; the transmitted ultrasound fields differ on their orientation as illustrated in Fig. 3.13, which facilitates to generate de-correlated set of echoes that are subsequently combined to create an enhanced quality image.

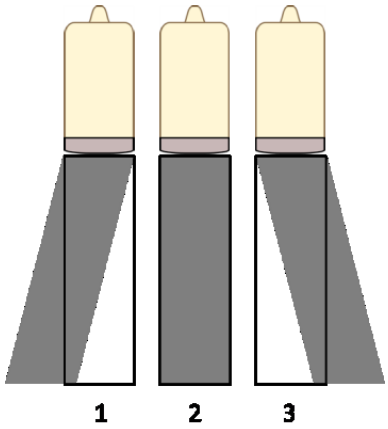

Fig. 3.13 – *Plane waves transmission.* Ultrasound plane waves can be emitted with a linear array by firing every element at the same time (fig. 3.8 – panel c). Steered plane waves can also be transmitted by linearly delaying pulsation of elements in the linear array, this induced phase lag results in tilted plane waves (Fig. 3.8 – panel d).

As the plane waves coherent compounding method involves beam steering, considerations have to be made regarding the angular steering range. Beam steering alters the impulse response of the system, also grating lobes can appear degrading image quality and introducing artefacts [11]. In order to make sure that the selected steering angles provide suitable impulse responses and avoid the appearance of grating lobes, linear array properties (pitch and central frequency) are taken into account to estimate such a steering range.

As echoes are summed, contrast and spatial resolution are progressively ameliorated. It has been shown in a previous research that combining about 10 oriented transmits can be enough to match the same image quality obtained with the conventional focused ultrasound technique [19]. The same approach can be applied using diverging waves. The implementation of this scheme generates sector shaped images reconstructed with a single transmit (see Fig. 3.14 – left and center images); coherently compounding of multiple single transmit images delivers an enhanced quality (see Fig. 3.14 – right image)

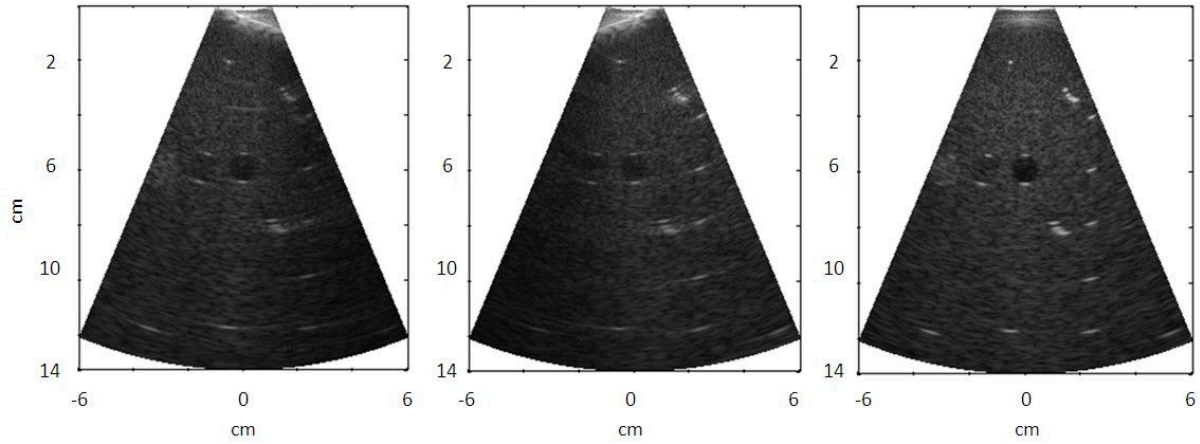

Fig. 3.14 – *Diverging waves images and coherent compounding.* Sectorial images obtained using single diverging transmits (steered and centered at left and middle images respectively). A sectorial image exhibits enhanced quality due to coherent compounding.

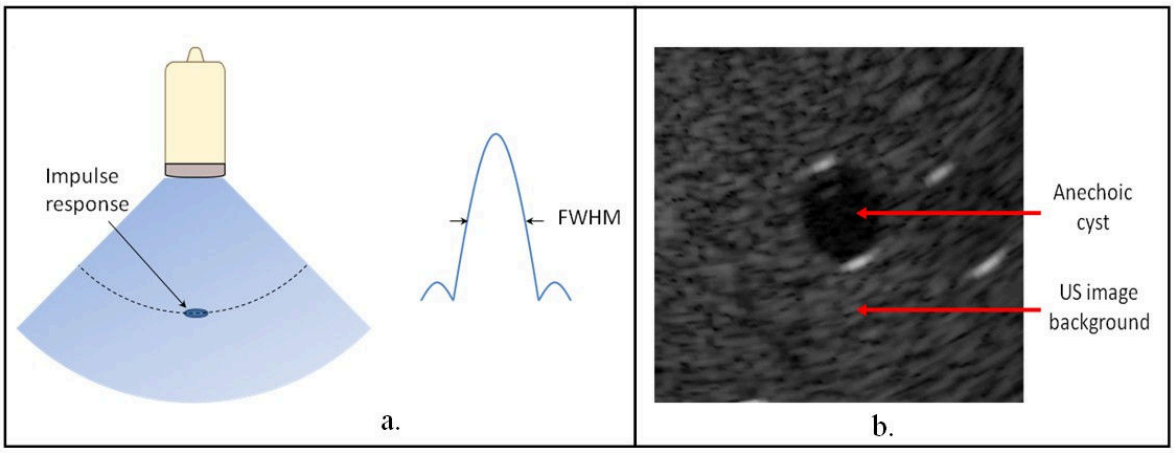

Fig. 3.15 - *Full width at half maximum (FWMH)*. Ultrasound system lateral resolution estimation (panel a). *Contrast to noise ratio (CNR)*. Contrast to noise ratio measured on anechoic cyst (panel b).

3.6.1 Ultrafast ultrasound motion artefacts

Coherent compounding is performed in ultrafast ultrasound to enhance image quality. Such a technique consists in averaging multiple B-mode images from the same ROI; therefore when moving structures exhibit big displacements between the first and last compounded images, motion artefacts are likely to appear in the compounded frame [20]. Multiple techniques have been proposed to correct motion aberrations stemming from coherent compounding [21-23]. A very simple way to reduce coherent compounding artefacts is to limit the amount of averaged frames (~5 to 9) and to utilize the maximal allowed pulse repetition frequency (PRF).

3.7 B-mode ultrasound image quality

Ultrasound images quality can be evaluated by measuring their lateral resolution and the contrast to noise ratio (CNR). The lateral resolution is the capacity of an imaging system to distinguish two points located one beside the other one. The lateral resolution is estimated by measuring the full width at half maximum (FWHM) of the ultrasound system impulse response; the impulse response is obtained by imaging a punctual reflector (this is usually done using a phantom with very fine threads). An image row crossing through the impulse response is used to estimate the lateral resolution the ultrasound imaging technique (see Fig. 3.15 – panel a).

The contrast to noise ratio or contrast resolution makes reference to the ability of the ultrasound system to detect anechoic objects upon strong echogenic off-axis features. The acoustic clutter generated by off-axis features reduces the detectability of anechoic features such as blood and vessels. The CNR of an ultrasound image is estimated using an anechoic cyst (see Fig. 3.15 – panel b) by applying the next formula,

$$\mathrm{CNR} = 20\log_{10}\frac{\left|\mu_{\mathrm{cyst}} - \mu_{\mathrm{bg}}\right|}{\sqrt{\left(\sigma^2_{\mathrm{cyst}} - \sigma^2_{\mathrm{bg}}\right)/2}}, \tag{3.15}$$

Where μ_{cyst} and μ_{bg} (σ^2_{cyst} and σ^2_{bg}) are the means (variances) of the gray scale intensities in the cyst and the background regions respectively.

3.8 Doppler ultrasound

The Doppler effect was postulated in 1842 by the Austrian physicist Christian Doppler. Such a prominent discovery was originally conceived for the astronomy field; however, latter on applications like Doppler ultrasound exploited this principle with diagnostic purposes [24]. The Doppler effect describes how the frequency shift experienced by a wave can be related to the velocity of a moving object. In the medical field, Doppler ultrasound imaging is used to determine the velocity of blood streams and cardiac structures, *e.g.* myocardium, valves, etc [25, 26].

The Doppler effect describes the frequency shift a wave experiences as it travels through a medium, such a frequency shift is therefore called Doppler frequency shift. A typical example of the Doppler effect is an ambulance that approaches a person: at the beginning, the person hears a high pitch, but then as the ambulance gets closer and passes through the person notices the pitch drops drown [27]. In Doppler ultrasound, the echoes reflected from moving particles can be processed to estimate the frequency shift taking place between the transmitted and reflected wave; such a frequency shift is then used to estimate the velocity of the object reflecting the echoes (see Fig. 3.16).

Independent of the wave nature, the Doppler frequency shift can be used to estimate the velocity of moving particles along the transmitted beam direction. If the angle between the particles trajectory and the transmitted beam is known, then the following equation can estimate the mean velocity of the irradiated particles,

$$V_{\mathrm{D}} = \frac{c\, f_{\mathrm{d}}}{2 f_{\mathrm{c}} \cos(\Theta)}, \tag{3.15}$$

where f_{d} is the Doppler frequency shift, c is the wave propagation velocity, f_{c} is the center frequency of the transmitted wave, Θ is the angle between the particle main trajectory and the wave beam and V_{D} is the mean Doppler velocity of the irradiated particles. Multiple ultrasound Doppler approaches techniques are used in the medical field:

Audible continuous wave Doppler: This technique uses continuous ultrasound (CW) to estimate the Doppler shift between a transmitted and received ultrasound beams. The Doppler shift falls within the audible frequencies range so it can be directly converted into audio. The Doppler shift sound allows users identify laminar or turbulent blood flows.

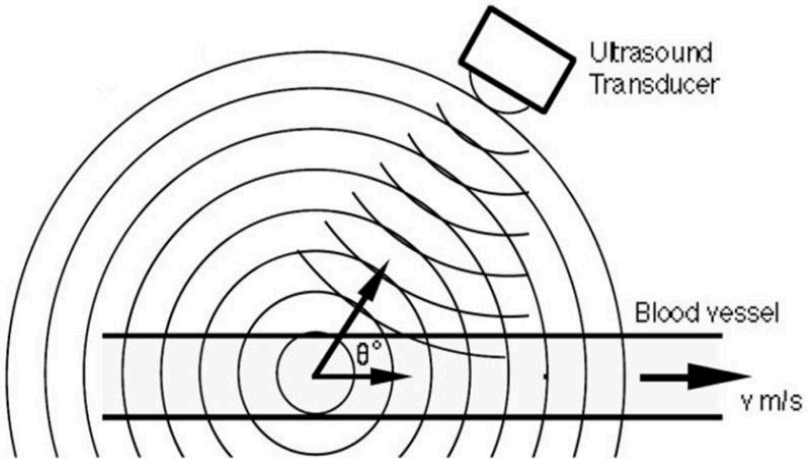

Fig. 3.16 – *Schematic working principle of Doppler ultrasound.* An ultrasound beam is transmitted towards the vessel, then ultrasound echoes are reflected back to the transducer. The registered echoes are processed to estimate the frequency shift between the transmitted wave and the reflected echoes [28].

Laminar flows produce a smooth and pleasant sound, whereas turbulent flows expose a harsh and rough sound.

Pulsed-wave (PW) spectral Doppler: This technique is conducted by transmitting pulsed ultrasound beams into the interrogated volume. The Doppler shift is represented graphically as a succession of spectrums vs time (see Fig. 3.17 left-panel). The PW spectral Doppler technique only measures the blood velocity at the *sample volume* location, which is a small region along a single *A-line* in the B-mode image (see Fig. 3.17 – left panel).

Color Doppler: As opposed to the two previous techniques, color Doppler uses PW ultrasound to measure velocities at multiple spatial locations. Color maps in red and blue scales represent blood velocities and their directions; color Doppler images are complemented by superimposing the color maps on B-mode images. A color flow map of the heart is presented in Fig. 3.17 – right panel.

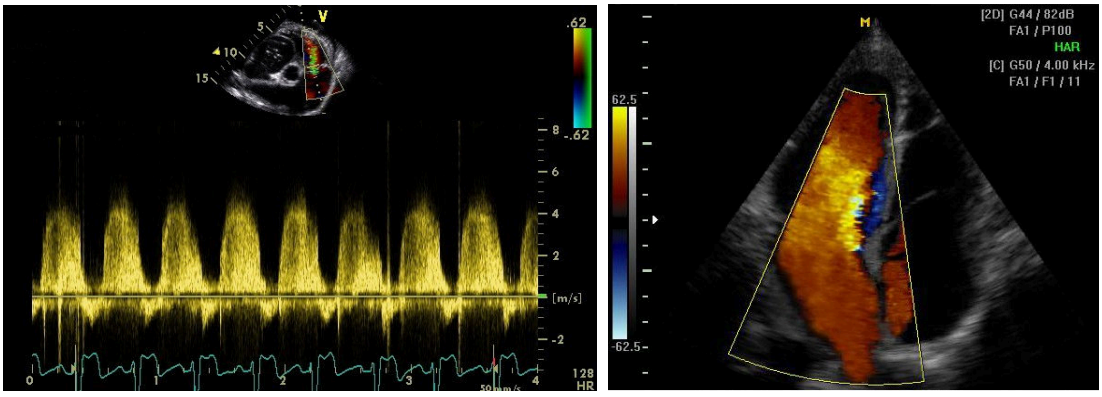

(a) PW spectral Doppler image (b) Color Doppler image

Fig. 3.17 – *Left panel:* Cardiac spectral Doppler image. *Right panel:* Cardiac color Doppler image.

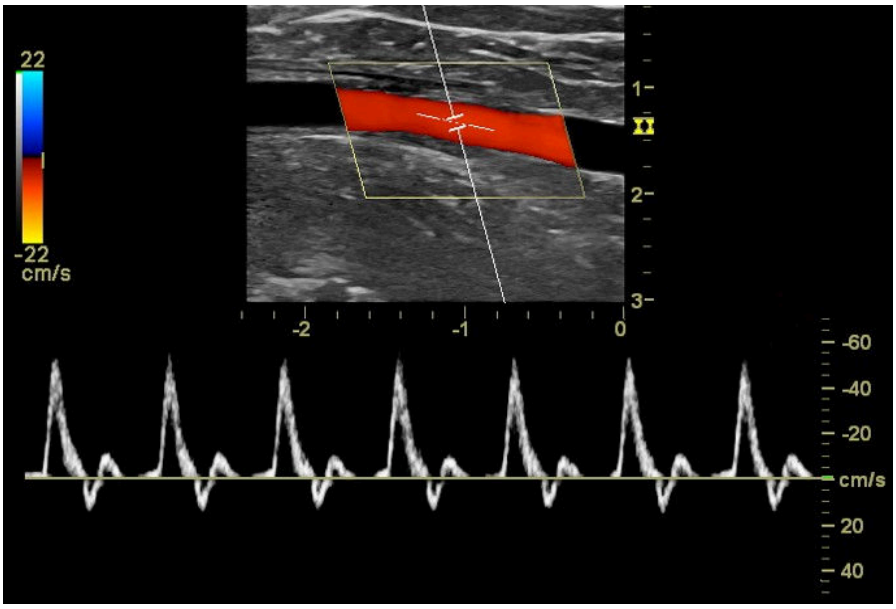

Fig. 3.18 – *Triplex mode PW ultrasound Doppler image.* Tripplex mode image (B-mode, color Doppler and spectral Doppler are presented in the same image). The sample volume can be identified as a marker inside the blood vessel, along the white line that crosses the B-mode image.

3.8.1 Ultrasound scattering by red blood cells

Scattering is known as a non-specular reflection mechanism; it takes places when an ultrasound wave traveling through a medium encounters reflectors of size equal or smaller to its wavelength, λ. When ultrasound is scattered, the incident wave is reflected in many different directions that do not obey the simple reflection laws, *e.g.* echoes from specular reflectors. Scattering occurs when ultrasound waves interact with very small structures in the body such as red blood cells present in the blood [1]. As an illustration of how scattering takes place in cardiac imaging, consider a phase array of central frequency $f_c = 2.5$ MHz and wavelength $\lambda = 0.6\,mm$; since the wavelength is much longer than the red blood cells diameter (~ 0.2 to 0.7 μm), scattering occurs when blood is reached by the ultrasound beams transmitted with this type of probe.

Although scattered echoes are much weaker that specular echoes, current ultrasound probes can digitize scattered echoes from red blood cells. The scattered echoes can then be used to perform blood flow velocity estimations using the following Doppler imaging techniques.

3.9 Pulsed-wave Doppler imaging (spectral representation)

Both continuous wave (CW) and pulsed-wave (PW) ultrasound beams can be used to conduct blood flow Doppler measurements in the cardiovascular system. As opposed to CW Doppler, PW Doppler provides anatomic information about where the velocity measurement is conducted (such a spot is known as the sample volume); in PW Doppler a B-mode image is used to select the sample volume (see image 3.18 – upper part), and

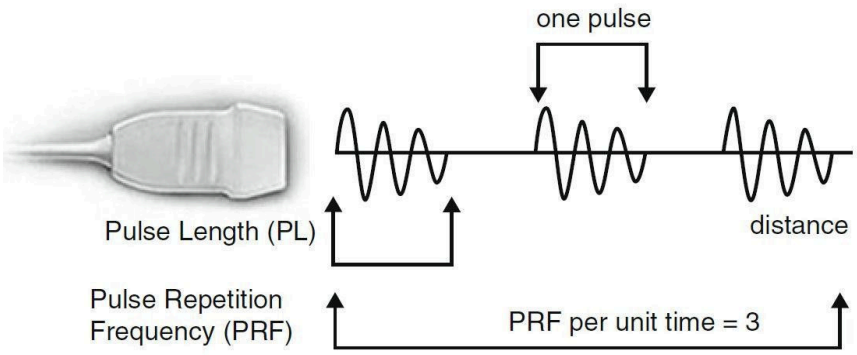

Fig. 3.19 - *Schematic representation of ultrasound pulse generation.* The image presents and scheme in which the PRF is equal to three, in other words, three pulses are transmitted every second. In a real setting, echocardiography probes transmit 1500 to 5000 pulses per second; this means the PRF ranges between 1.5 KHz to 5 KHz (by www.USRA.ca).

results are presented as a succession of spectrums that indicate the mean velocity at the sample volume (see image 3.18 – lower part).

As opposed to B-mode imaging where single pulses are transmitted, in PW Doppler three to four pressure trains are consecutively transmitted in every ultrasound beam (see Fig. 3.19). The amount of pulses intermittently transmitted every second corresponds to the pulsed system PRF (just as in B-mode imaging - see section 3.4.3).

Although the PW Doppler technique is supposed to use the Doppler effect to conduct velocity measurement, it does not estimate the Doppler frequency shift of every ultrasound pulse-echo; the PW Doppler technique actually estimates the mean frequency shift $\bar{f}$ along multiple reflected *A-lines*, therefore the mean particle Doppler velocity $\overline{V_{\mathrm{D}}}$ at a given depth of an *A-line* can be estimated with equation (3.16),

$$\overline{V_{\mathrm{D}}} = \frac{\bar{f}}{f_{\mathrm{c}}} \frac{c}{2\cos(\Theta)}, \tag{3.16}$$

PW Doppler signals are created by sampling the same *sample volume* in consecutive *A-lines;* in consequence, the sampling frequency of PW Doppler signals corresponds to the PRF of the ultrasound pulsed system (see Fig. 3.20). In Fig. 3.20 multiple samples have been collected at the same depth of an *A-line* to create a PW Doppler signal. The amount of samples in a PW Doppler signal is called *ensemble length* or *package size*.

In PW Doppler the mean frequency shift of Doppler signals is estimated by means of Fourier transform algorithms, *e.g.* the fast Fourier transform algorithm (FFT). In order to provide an acceptable spectral estimate, most Fourier transform approaches require a substantial amount of samples (the FFT requires at least 128 samples) which makes the process computationally expensive. Due to the time required to perform the Fourier transform algorithms, the PW Doppler technique is limited to measure velocities within a single sample volume at a time (see Fig. 3.18).

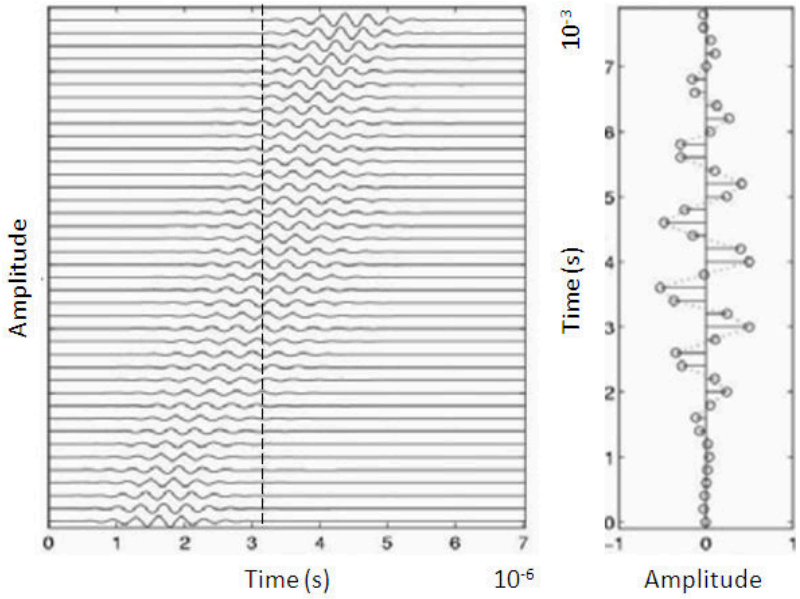

Fig. 3.20 - *Schematic representation of how PW Doppler signals are sampled and put together. Left panel:* The dashed line indicates the depth (*sample volume*) where samples have been collected in a succession of *A-lines*. *Right panel:* The dotted line represents a PW Doppler signal [28].

The following section presents the color Doppler technique which as the PW Doppler approach also transmits PW ultrasound beams. As opposed to the PW spectral Doppler method, color Doppler estimates the mean Doppler frequency using just few samples (~8 to 14 samples). Since the scheme used by color Doppler is much faster than the FFT algorithms, the color Doppler can estimate velocities in many sample volumes for the same image, and therefore display the results as colourful velocity maps.

3.10 Color Doppler imaging

The color Doppler technique uses PW ultrasound beams to estimate velocities in many sample volumes (multiple depths and *A-lines*). Specific transmit beamforming strategies make possible to generate multiple color Doppler lines, which put together create a color Doppler map. Color Doppler maps are superimposed in B-mode images to represent a complete anatomical blood flow view (the triplex mode image in Fig. 3.18 presents a blood vessel color Doppler map).

The phased shift approach introduced by Kasai *et al* [29] is currently the most widespread technique to perform color Doppler velocity estimations. The Kasai model exploits the fact that the Doppler signals mean angular frequency is equivalent to its phase shift,

$$\bar{\omega} = \Delta\varphi, \tag{3.17}$$

where $\bar{\omega}$ and $\Delta\varphi$ are respectively the mean angular frequency and the phased shift of the PW Doppler signals described in section 3.10. The autocorrelation expression used to estimate the mean angular frequency (phase shift) can be written in terms of the IQ complex signal [27],

$$\bar{\omega} = \frac{1}{T_{prf}} arctan\left[\frac{\sum_{i=1}^{N} Q(i)I(i-1) - I(i)Q(i-1)}{\sum_{i=1}^{N} I(i)I(i-1) - Q(i)Q(i-1)}\right], \tag{3.18}$$

where T_{prf} is the time repetition period (inverse of the pulsed system PRF). The use of equation (3.18) alleviates the computational expense of the velocity estimation process by using the demodulated IQ signals.

3.10.1 Color Doppler Clutter rejection filters (Wall filter)

When conducting color Doppler imaging, echoes stem both from red blood cells and slowly moving or stationary tissues. In order to conduct velocity estimations, the registered RF signals have to be filtered to eliminate the information coming from tissue motion; such a procedure is conducted to eliminate the bias that clutter frequencies may have on the blood flow velocity estimates.

The clutter filtering procedure is performed after RF signal are beamformed and before color Doppler velocities are estimated. The clutter filtering signal processing approach allows attenuating the low frequencies generated by slowly moving tissues that surround the blood flow, *e.g.* the heart and blood vessel [27].

Color Doppler signals comprise usually 8 to 14 samples only; such a limited amount of information represents a challenging scenario for clutter filters. The most common color Doppler clutter filters are presented in the following paragraphs; although, all of these filters satisfy the basic needs posed by color Doppler imaging, some of them have proved to be superior [30, 31]:

Finite impulse response filters (FIR)

FIR filter are time invariant and they exhibit the lowest computational complexity in comparison to others type of filters, *e.g. eigenvalues* based clutter filters. FIR filters are performed on present and past signal samples; the filtered signal is estimated performing the convolution sum in (3.19).

$$y(n) = \sum_{k=0}^{K} h(k)x(n-k), \tag{3.19}$$

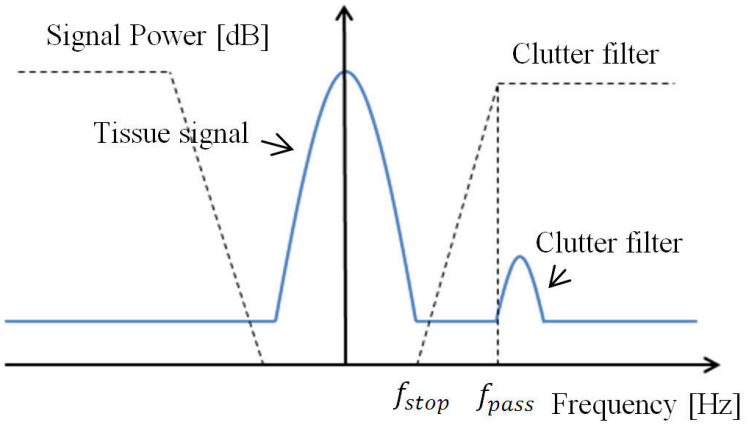

Fig. 3.21 – *Ultrasound Doppler clutter filtering representation*

Where $h(k)$ is the filter impulse response, $y(n)$ and $x(n)$ are respectively the output and input signals, K is the filter order, and n is the sample index (for pulsed Doppler it corresponds to the ensemble size). One limitation related to the FIR filters, is that the number samples in the filtered signal will always be $N - K$ since the first K samples are lost in the initialization process.

Infinite impulse response filters (IIR)

As opposed to FIR filters, IIR filters are performed using both present and past samples of the input signal. This feature limits IIR filters to being used off-line only. A proper initialization is required in IIR filter to guarantee stability or long transient responses. The output filtered signal from IIR filters can be written as per the following difference equation:

$$y(n) = -\sum_{k=1}^{K} a_k y(n-k) + \sum_{k=0}^{K} b_k x(n-k), \tag{3.20}$$

Polynomial regression filters

Regression filters are tailored under the hypothesis that the low frequency oscillations generated by slow moving tissue can be fitted by a polynomial function. The fitting polynomial function that approximates the clutter frequencies is subtracted from the original Doppler signal containing both the Doppler and clutter information. Polynomial regression filters can be implemented using the following affine models [30]:

$$y(n) = \left(\mathrm{I} - \sum_{k=0}^{K} \mathrm{b}_k \mathrm{b}_k^H \right) \mathbf{x}, \tag{3.21}$$

where **x** is the complex IQ Doppler signal (slow time samples, sampling frequency equals to the PRF of the pulsed system); *y* is the complex filtered output signal; I is the identity matrix, b_k are orthonormal basis vectors spanning the clutter signal subspace of dimension *k*+1, *k* is the filter order and *H* is the hermitian transposition.

Clutter filtering can also be adapted to conduct tissue motion color Doppler imaging; since this topic is not the focus of this report, no further explanation is provided, but the interested reader can find more information in an article published by Steinar *et al* that offers a complete illustration on this subject [32].

3.10.2 Color Doppler limitations

The two main limitations related to ultrasound color Doppler imaging are the Nyquist velocity and the low temporal resolution. As shown in section 3.10, the phase shift can be estimated using equation (3.18). The presence of the *arctan* function bounds the phase shift to the range $[-\pi, \pi]$, therefore the maximum absolute unambiguous velocity (Nyquist velocity) that can be estimated with this expression is,

$$V_{\mathrm{N}} = \frac{c\ PRF}{4f_{\mathrm{c}}}, \tag{3.22}$$

The phenomenon known as aliasing takes place when color Doppler is used to scan velocities over the Nyquist limit. As per the Shanon Nyquist theorem, aliasing can be avoided by setting an adequate sample rate but this one faces a physical limitation by the ultrasound propagation velocity and the scanning depth,

$$\mathrm{PRF}_{max} = \frac{c}{2r_{\mathrm{max}}}, \tag{3.23}$$

Another important limitation of ultrasound color Doppler imaging is its low temporal resolution (~15 to 30 fps). The low color Doppler frame rate is a consequence of the focused transmits beamforming approach; 8 to 14 transmits are needed to generate one single color Doppler line, this has a devastating impact in the overall frame rate of duplex or triplex imaging approaches.

In this chapter, the principles of ultrasound imaging have been introduced. The piezoelectric effect and some phased array properties such as the radiation pattern and steerability have been explained. Also the interaction of ultrasound waves and the B-mode

image formation process (beamforming process). Beyond the ultrasound principles, various Doppler ultrasound techniques were portrayed as well as some signal processing methods used in the color Doppler imaging modality.

Having introduced the basics of ultrasound B-mode and Doppler imaging, the next chapter presents the methodology to implement de ultrafast echocardiography method using diverging circular beams. In addition, the next chapter unveils the quantification carried out to assess the image quality of the ultrafast cardiac echo approach. Finally, some *in vivo* examples obtained with such a technique are also presented.

Bibliography

[1] D. H. Evans, *Doppler ultrasound: Physics, instrumentation, and clinical applications*: John Wiley & Sons, 1989.

[2] V. Mor-Avi*, et al.*, "Current and evolving echocardiographic techniques for the quantitative evaluation of cardiac mechanics: ASE/EAE consensus statement on methodology and indications: endorsed by the Japanese Society of Echocardiography," *Journal of the American Society of Echocardiography,* vol. 24, pp. 277-313, 2011.

[3] R. Aaslid*, et al.*, "Noninvasive transcranial Doppler ultrasound recording of flow velocity in basal cerebral arteries," *Journal of neurosurgery,* vol. 57, pp. 769-774, 1982.

[4] J. Baun, "Physical principles of general and vascular sonography," *San Francisco, Calif: California Publishing Co,* 2004.

[5] A. Manbachi and R. S. Cobbold, "Development and application of piezoelectric materials for ultrasound generation and detection," *Ultrasound,* vol. 19, pp. 187-196, 2011.

[6] A. Selfridge*, et al.*, "A theory for the radiation pattern of a narrow-strip acoustic transducer," *Applied Physics Letters,* vol. 37, pp. 35-36, 1980.

[7] A. C. Clay*, et al.*, "Experimental study of phased array beam steering characteristics," *Journal of nondestructive evaluation,* vol. 18, pp. 59-71, 1999.

[8] S.-C. Wooh and Y. Shi, "Optimum beam steering of linear phased arrays," *Wave motion,* vol. 29, pp. 245-265, 1999.

[9] S.-C. Wooh and Y. Shi, "A simulation study of the beam steering characteristics for linear phased arrays," *Journal of nondestructive evaluation,* vol. 18, pp. 39-57, 1999.

[10] L. W. Schmmer Jr, "Fundamentals of ultrasonic phased arrays," *Modern Physics Letters B,* vol. 22, pp. 917-921, 2008.

[11] O. T. Von Ramm and S. W. Smith, "Beam steering with linear arrays," *Biomedical Engineering, IEEE Transactions on,* pp. 438-452, 1983.

[12] J. T. Bushberg and J. M. Boone, *The essential physics of medical imaging*: Lippincott Williams & Wilkins, 2011.

[13] M. LEWANDOWSKI*, et al.*, "Research & Medical Doppler platform," *Acoustics 2012 Nantes,* 2012.

[14] S. Webb and M. A. Flower, *Webb's physics of medical imaging*: CRC Press, 2012.

[15] C. R. Hill*, et al.*, *Physical principles of medical ultrasonics*: Wiley Online Library, 2004.

[16] V. Chan and A. Perlas, "Basics of ultrasound imaging," in *Atlas of Ultrasound-Guided Procedures in Interventional Pain Management*, ed: Springer, pp. 13-19, 2011.

[17] S. A. Tretter, "Fundamentals of Quadrature Amplitude Modulation," in *Communication System Design Using DSP Algorithms*, ed: Springer, pp. 215-230, 2003.

[18] J. Kirkhorn, "Introduction to IQ-demodulation of RF-data," *IFBT, NTNU,* vol. 15, 1999.

[19] G. Montaldo*, et al.*, "Coherent plane-wave compounding for very high frame rate ultrasonography and transient elastography," *Ultrasonics, Ferroelectrics and Frequency Control, IEEE Transactions on,* vol. 56, pp. 489-506, 2009.

[20] M. Tanter and M. Fink, "Ultrafast imaging in biomedical ultrasound," *Ultrasonics, Ferroelectrics, and Frequency Control, IEEE Transactions on,* vol. 61, pp. 102-119, 2014.

[21] B. Denarie*, et al.*, "Coherent plane wave compounding for very high frame rate ultrasonography of rapidly moving targets," *Medical Imaging, IEEE Transactions on,* vol. 32, pp. 1265-1276, 2013.

[22] J. A. Jensen*, et al.*, "Synthetic aperture ultrasound imaging," *Ultrasonics,* vol. 44, pp. e5-e15, 2006.

[23] W. Jing and J.-y. Lu, "Motion artifacts of extended high frame rate imaging," *Ultrasonics, Ferroelectrics, and Frequency Control, IEEE Transactions on,* vol. 54, pp. 1303-1315, 2007.

[24] E. G. Grant*, et al.*, "Clinical doppler imaging," *American Journal of Roentgenology,* vol. 152, pp. 707-717, 1989.

[25] W. McDicken and T. Anderson, "The difference between colour Doppler velocity imaging and power Doppler imaging," *European Journal of Echocardiography,* vol. 3, pp. 240-244, 2002.

[26] P. N. Burns, "The physical principles of Doppler and spectral analysis," *Journal of clinical ultrasound,* vol. 15, pp. 567-590, 1987.

[27] D. H. Evans*, et al.*, "Ultrasonic colour Doppler imaging," *Interface Focus,* vol. 1, pp. 490-502, 2011.

[28] J. A. Jensen, *Estimation of blood velocities using ultrasound: a signal processing approach*: Cambridge University Press, 1996.

[29] C. Kasai*, et al.*, "Real-time two-dimensional blood flow imaging using an autocorrelation technique," *IEEE Trans. Sonics Ultrason,* vol. 32, pp. 458-464, 1985.

[30] H. Torp, "Clutter rejection filters in color flow imaging: A theoretical approach," *Ultrasonics, Ferroelectrics and Frequency Control, IEEE Transactions on,* vol. 44, pp. 417-424, 1997.

[31] A. P. Kadi and T. Loupas, "On the performance of regression and step-initialized IIR clutter filters for color Doppler systems in diagnostic medical ultrasound," *Ultrasonics, Ferroelectrics and Frequency Control, IEEE Transactions on,* vol. 42, pp. 927-937, 1995.

[32] S. Bjaerum*, et al.*, "Clutter filters adapted to tissue motion in ultrasound color flow imaging," *Ultrasonics, Ferroelectrics, and Frequency Control, IEEE Transactions on,* vol. 49, pp. 693-704, 2002.

Chapter 4

Ultrafast echocardiography using full aperture diverging beams

The low temporal resolution of the single line acquisition (SLA) echocardiography approach (~ 60 fps) represents an important limitation to conduct thorough cardiac examinations. Alternatively, ultrafast ultrasound exploits transmission of broadened beams to increase the effective frame-rate (even thousands of fps). In this chapter, coherently compounded images obtained from diverging circular beams (DCB) were investigated for ultrafast echocardiography purposes. *In vitro* experiments were conducted with the Verasonics scanner and a linear phased array (2.5 MHz, 64 elements). The on-axis lateral resolution and contrast to noise ratio (CNR) were quantified using a tissue mimicking phantom with 0.1 mm nylon threads and 10 mm diameter anechoic cysts. Furthermore, the off-axis lateral resolution was measured using a threads phantom (0.1 mm nylon threads). Coherently compounded images (13 images) obtained with the DCB technique featured comparable on-axis lateral resolution to that of the SLA approach (2.3 mm vs. 2.1 mm @ 8-cm-deep), and exhibited a matching on-axis CNR (about 10 dB @ 6-cm-deep). *In vivo* examinations validated the clinical feasibility of the DCB strategy (long and short axis views at 400 fps) and led the clinical specialists to conclude the DCB approach provides high-quality cardiac images that satisfy the clinical needs.

4.1 Introduction

Echocardiography is the most utilized imaging technique to assess the cardiac function; it is the only imaging modality that allows dynamic representations of the heart in real time. Throughout its existence, echocardiography has evolved by adding many features *e.g.* spectral and color Doppler, speckle tracking, tissue Doppler, etc.; in this manner, echocardiography has become an imaging tool that is now essential in the clinical setting. Nowadays, echocardiography is the gold standard to detect congenital paediatric diseases [1], non-invasive assessments of aortic and mitral regurgitations [2, 3], determining the LV ejection fraction [4], among others. These procedures can diagnose abnormalities of the cardiac performance, and therefore open doors for possible therapeutic and/or surgical treatments.

Conventional echocardiography creates sector-scan images by putting together *A-lines* that are created one at a time after transmitting focused ultrasound beams; such a method is knows as single line acquisition (SLA) echocardiography. In the conventional SLA echocardiography approach, the time needed to create one image depends on the maximal interrogated depth and the amount of lines comprised in one frame; this time can be estimated as in equation (3.14) [5].

Interrogated depths in echocardiography vary in between 10 to 15-cm, so in average frame rates of 40 to 80 fps are feasible. New quantitative echocardiographic methods claim

for higher frame rates, i.e. contrast echocardiography "echo VIP" [6, 7], speckle tracking [8, 9], VFM [10], among others; this chapter presents the methodology to conduct echocardiographic examinations at very high frame rates (400-800 fps) by implementing diverging beams. The ultrafast echocardiography image quality quantifications are also presented in this section.

The order of this chapter is described in this paragraph: before presenting the work done, a summary of former contributions on ultrafast echocardiography is portrayed. Afterwards, the ultrafast echocardiography methodology used in our study is introduced. Following, the results obtained are presented: extensive *in vitro* measurements were performed to evaluate the outcome of the implemented method and also *in vivo* validations were carried out.

4.1.1 Ultrafast ultrasound

Ultrafast ultrasound imaging exploits the use of broadened ultrasound beams to gather information from a broad region-of-interest. It can create images with fewer transmissions, hence much higher frame rates can be attained in comparison to the conventional successive focused ultrasound transmits scheme. Ultrafast ultrasound has been thoroughly described and implemented by Montaldo *et al*; plane wavefronts (PW) transmits and coherently compounding of multiple frames were proved to enhance image quality while drastically enhancing the temporal resolution [11]. Multiple applications have taken advantage of plane wave imaging and the high frame rates exhibited by this approach (up to 15000 fps), *e.g.* shear waves elastography imaging and vascular high frame rate color Doppler are two examples of the breakthrough PW imaging has produced in the ultrasound domain [11-13]. The time required to create one B-mode frame with ultrafast ultrasound is,

$$T_{image} = \frac{2rN_B}{c}, \tag{4.1}$$

where N_B is the number of compounded transmissions in one single B-mode frame.

4.1.2 High frame rate echocardiography

The heart being a moving object, demands a high temporal resolution to carefully follow its dynamics through the cardiac cycle. Methods to increase echocardiography temporal resolution have been investigated for decades. In the 80's a first effort was made by Shattuck *et al* to increase temporal resolution by a factor of four, their principle was to transmit broadened ultrasound beams, and reconstruct multiple lines out of the recorded data [14]. Hasegawa *et al* showed lately the potential of the using diverging transmit beams and parallel receive beamforming in echocardiography, with his approach Hasegawa achieved a frame-rate of 316 fps, but increased side-lobe level degraded the contrast of the B-mode images [15]. More recently, Omanski *et al* proved the potential of diverging waves to conduct ultrafast Doppler of the heart [16]. In his study, Omanski presented encouraging *in vivo* results obtained using diverging beams. In the same direction, Papadacci *et al* introduced a synthetic aperture technique for ultrafast echocardiography, in which diverging beams were generated with sub-apertures of the linear phased-array [17].

This article presents a thorough evaluation of the ultrafast echocardiography technique conducted by transmitting diverging circular beams with the full aperture of a linear phased-array. Many principles have been taken from former works in the same domain; nevertheless, our contribution strives in defining the boundaries and capabilities of this ultrafast imaging scheme, which up-to-date have not been fully investigated.

4.2 Methods

4.2.1 Plane wave imaging inspiration

Plane wave imaging has been successfully used in pediatric cardiac imaging [8] due to the possibility of transmitting ultrasound radiation through infants ribs and the small size of their heart. Plane wave imaging has also been used to conduct open chest sonograms of the heart [18], but transthoracic echocardiographic examinations in adults are not possible with this imaging technique; the small acoustic window encountered in mature patients requires the use of a small footprint transducer, therefore phased array transducers are utilized to conduct these type of procedures. Using plane wave with a phased array transducer provides a narrowed ROI, which does not correspond to the usual sectorial field of view essential in echocardiographic assessments. In the following sections, an analog approach to the one used by plane wave imaging is presented; in this case diverging circular beams help imaging sectorial fields of view at ultrafast frame rates.

4.2.2 Diverging circular beams transmission

The diverging circular beams approach investigated in this chapter has many analogies with the plane wave imaging technique. Both methods use the full aperture of a linear array to insonify the region of interest. Also, in both schemes the steered beam keeps a constant width regardless its steering angle. In plane wave the beam width corresponds to the aperture of the linear array, whilst in diverging circular beams, the beam width corresponds to the angular aperture of the sectorial image.

In plane wave, the orientation of wavefront is obtained by linearly delaying the transmission of each piezoelectric element, this introduces a linear phase lag among the waves generated by the linear array; in order to use an analog approach with diverging circular beams, a virtual source is considered behind the piezoelectric elements (see Fig. 4.1); knowing the virtual source spatial coordinates allows estimating the necessary delay law to transmit a diverging wave. If $\overrightarrow{z_0}$ is the spatial location of the virtual source (for a centered virtual source the x coordinate is zero) and $\overrightarrow{x_n}$ are the coordinates of every element in the phased array, then the time delays to generate a non-oriented diverging circular beam are given by equation (4.2) [18],

$$\tau_n = \frac{\|\overrightarrow{z_0} - \overrightarrow{x_n}\|}{c}, \tag{4.2}$$

where τ_n is the delay law and c is the ultrasound propagation velocity.

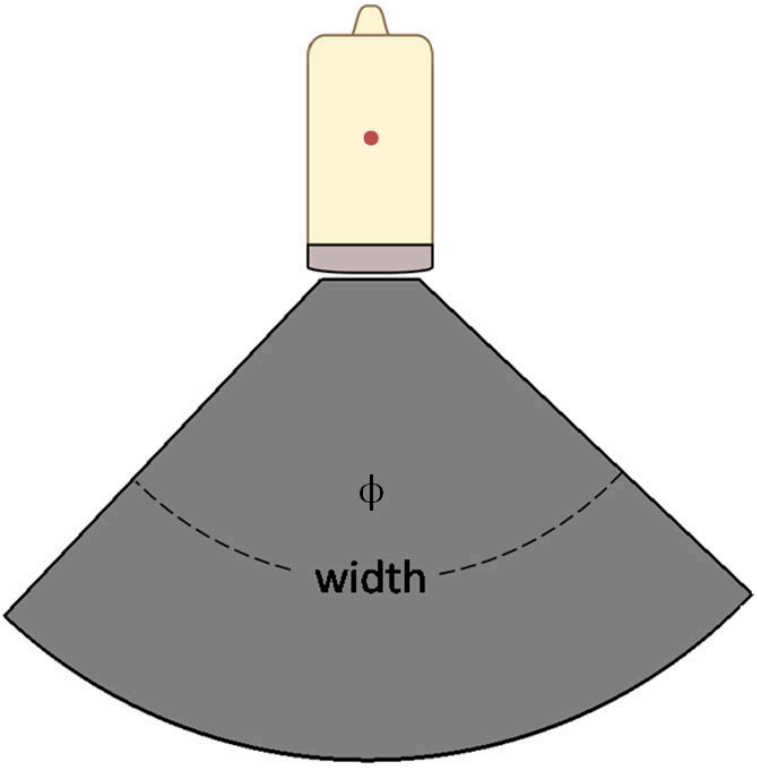

Fig. 4.1 – *Diverging circular beam transmission.* Ultrasound diverging circular beams can be transmitted with a phased linear array by supposing a virtual source behind the piezoelectric elements; positioning this virtual source allows to estimate the adequate time delays to trigger the phased array in a manner that the required diverging wave front can be obtained.

Consider now a steered diverging circular beam; the virtual source is now located at (x_0, z_0) (the virtual source x coordinate is no longer zero). Using a scalar notation, x_n is the position of each piezoelectric element, ϕ is the diverging circular beam angular width and β is the transmitted beam steering angle. The general virtual source coordinates x_0 and z_0, either centered or corresponding to an steered diverging beam, are given by:

$$z_0 = \frac{\Delta x(N-1)}{tan\left(\beta - \frac{\phi}{2}\right) - tan\left(\beta + \frac{\phi}{2}\right)}, \tag{4.3}$$

$$x_0 = z_0 tan\left(\left(\frac{\phi}{2} - \beta\right) + \frac{\Delta x(N-1)}{2}\right), \tag{4.4}$$

where Δx and N are respectively the pitch and the number of elements of the linear array. The delay law to generate a centered or steered diverging circular beam can be estimated using equation (4.5) once the virtual source coordinates x_0 and z_0 are known.

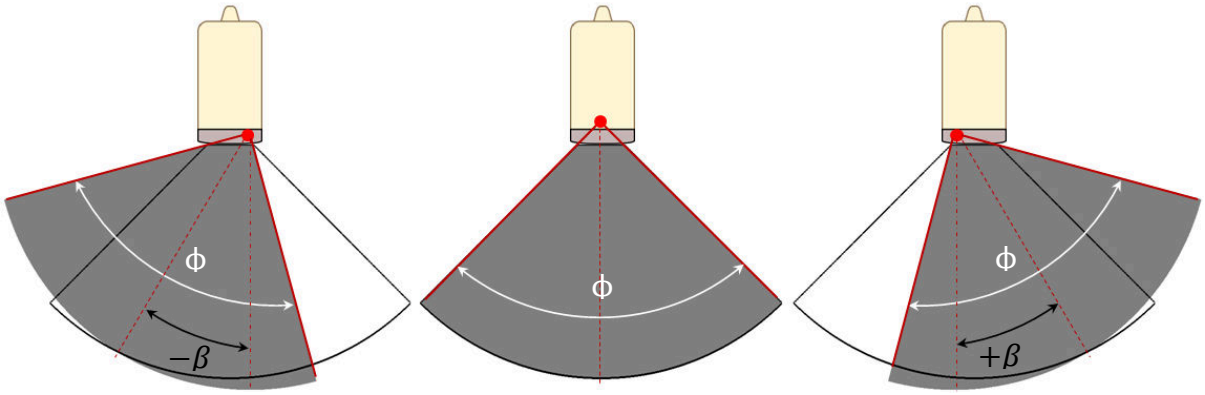

Fig. 4.2 – *Steered diverging circular beams.* Diverging circular beams in the left and right panels are steered at angles $-\beta$ and $+\beta$ with reference to the diverging circular beam presented in the center panel; all three ultrasound beams exhibit the same angular width ϕ.

$$\tau_n = \frac{\left\{\sqrt{(x_n - x_0)^2 + {x_0}^2} - min_n\sqrt{(x_n - x_0)^2 + {z_0}^2}\right\}}{c}, \tag{4.5}$$

Equation (4.5) provides the time delays to transmit steered diverging circular beams as illustrated in Fig. 4.2 - left and right panels. Also, the delay law to transmit a centered diverging beam can be obtained by making $\beta = 0$ (see Fig. 4.2, center panel).

As per plane waves transmission, the steering of diverging ultrasound beams modifies the impulse response of the ultrasound system with reference to none steered beams. The pulse-echo variations experienced by steered diverging circular beams were investigated by analysing their radiation patterns. In the following section, diverging circular beams radiation patterns are simulated in order to establish an adequate angular steering range.

4.2.3 Diverging circular beams radiation pattern simulation

In this section, the model proposed by Selfridge *et al* [19] was used to investigate the steered DCB radiation patterns transmitted by a phased array. Radiation patterns were simulated in the far field and the steering effect was assessed to establish an acceptable steering range for diverging circular beams. According to Selfridge *et al*, the two-dimensional far field radiation pattern of a single element can be written as,

$$p(r,\theta) = \frac{p_0 w}{j(\lambda)^{1/2}} e^{2j\pi r/\lambda} \frac{sin\left(\pi w/\lambda sin(\theta)\right)}{\pi w/\lambda sin(\theta)} cos\theta, \tag{4.6}$$

where p is the acoustic field pressure, w is the single element width, λ is the wavelength in the medium, r and θ are the polar coordinates where the pressure field is calculated. It is worth seeing that expression (4.6) establishes an angular response that is

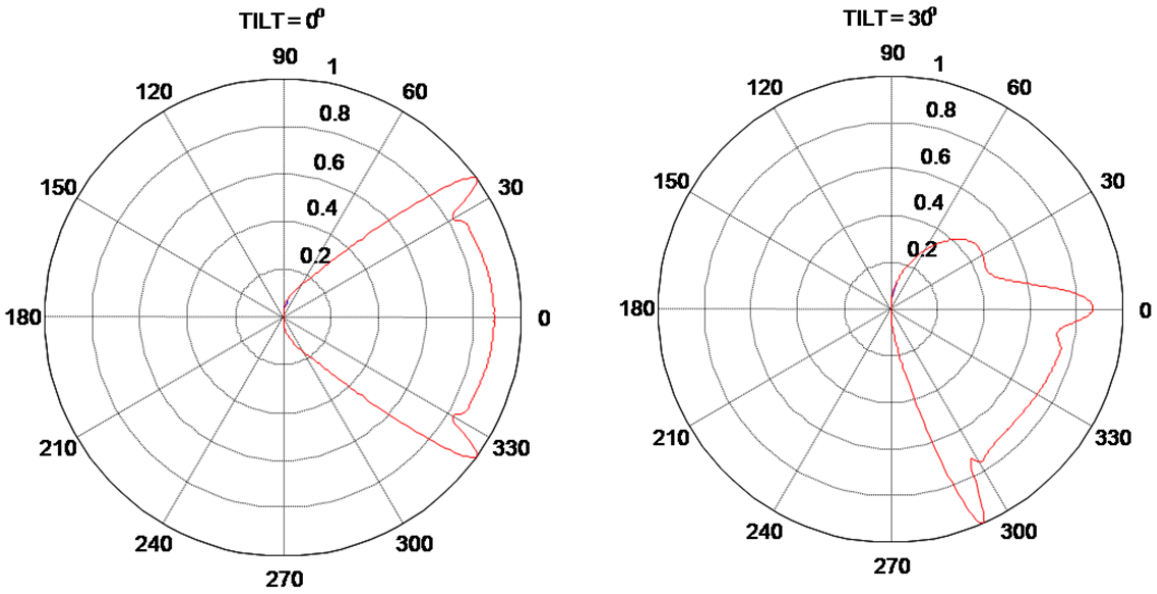

Fig. 4.3 – *Diverging circular beams radiation pattern.* Non-oriented ($\beta = 0°$) far-filed radiation pattern for a 90° width diverging circular beam, upper panel. Oriented ($\beta = 30°$) far-filed radiation pattern for a 90° width diverging circular beam, lower panel

non-zero only if $\theta \neq \frac{\pi}{2}$. Selfridge has shown that expression (4.6) accurately describes the pressure field of narrow strip acoustic transducer that emits an acoustic wave into a liquid, such a scenario can be interpreted as a piston surrounded by a soft baffle [19].

To estimate the radiation pattern generated by a phase array constituted of 64 piezoelectric elements, we added the angular responses of all individual elements at each spatial position where the radiation pattern was estimated. To perform accurate simulations, we also estimated the radiation pattern along a bandwidth of 60%; the simulation parameters matched the properties of the phased array used during the *in vitro* and *in vivo* experiments (ATL P4-2, 2.5-MHz central frequency, 64 elements, pitch = 0.32 mm). Expression (4.6) was used to obtain a non-steered ($\beta = 0°$) far field radiation pattern for a 90° wide ($\phi = 90°$) diverging circular wavefront (see Fig. 4.3 - upper panel). As expected, the angular response was found to be symmetrical with a spread homogeneous main lobe and two narrow side lobes.

Subsequently, estimation of steered radiation patterns was conducted by continuously increasing the steering angle β, both in the positive and negative directions. An additional side lobe was features by the steered radiation patterns as the steering angle increased; also, the pressure field started to be asymmetrical with reference to the steering axis (see Fig. 4.3 – lower panel).

4.2.4 Diverging circular beams steering delimitation

Considering the side lobe observed as diverging circular beams are steered, the following directivity parameter was introduced in order to establish an acceptable phased array steering range when transmitting such a kind of ultrasound beam:

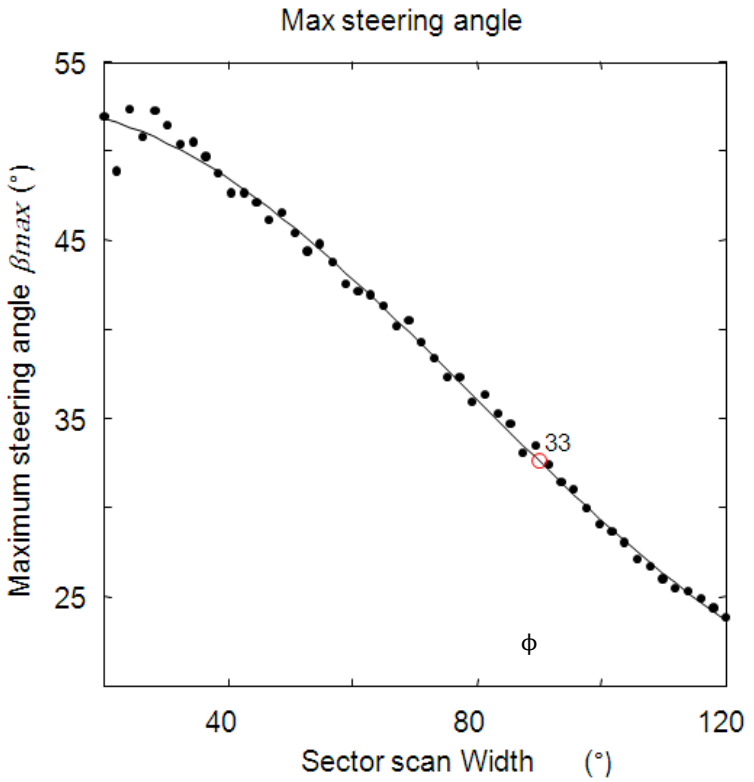

Fig. 4.4 – *Diverging circular beams maximum steering angle* β_{max} Maximum allowable steering angle for diverging circular beams in fuction of the sector-scan width ϕ.

$$dir(\beta, \phi) = \frac{\int_{\beta-\phi/2}^{\beta+\phi/2} P_{\mathrm{RMS}}^2(\theta)\mathrm{d}\theta}{\int_{-\pi/2}^{\pi/2} P_{\mathrm{RMS}}^2(\theta)\mathrm{d}\theta}. \tag{4.7}$$

Under purely geometrical assumptions, the area insonified by a steered diverging circular beam is delimited by the angles $(\beta - \phi/2, \beta + \phi/2)$ (see Fig. 4.2 – left and right panels). The directivity parameter given by equation (4.7) characterizes the amount of acoustic energy irradiated within the area previously described; a value of 1 reveals an "optimal" directivity. For example, the respective directivity parameters associated to the radiation patterns of Fig. 4.2 are: $dir(0^o, 90^o) = 0.97$ and $dir(30^o, 90^o) = 0.83$. For a given angular width ϕ, the corresponding maximal acceptable tilt (in terms of directivity) was determined from

$$\frac{dir\,(|\beta_{max}|,\phi)}{dir\,(0,\phi)} = 90\%. \tag{4.8}$$

Equation (4.8) was proposed under the expectation that non-tilted and tilted directivities would be similar at >90%. The arbitrary 90% threshold turned out to yield not-too-restrictive steering angles. The maximal steering angle $|\beta_{max}|$ decreases as the width ϕ

is increased. For a 90^{o}-wide sector, the maximal "acceptable" tilt with a P4-2 probe was estimated ro be 33^{o} (see Fig. 4.4). As an example, the steering range obtained for a 90° sector is $[-33°: +33°]$ (see Fig. 4.4).

As mentioned before, Fig. 4.4 shows that as the sector-scan width ϕ decreases, then the maximum steering angle β_{max} augments, so we propose the following formula to compute the steering range, if $\beta_{max} < \frac{\phi}{2}$, then the steering range will be given by,

$$\beta_{range} = \left[-\frac{(150-\phi)}{2} : \frac{(150-\phi)}{2}\right], \tag{4.9}$$

Additionally, if $\beta_{max} \geq \frac{\phi}{2}$, then the steering range simply becomes,

$$\beta_{range} = \pm\frac{\phi}{2}, \tag{4.10}$$

4.2.5 Experimental approach

This paragraph describes how the diverging circular beams imaging technique was implemented to generate B-mode images. All *in vitro* and *in vivo* experiments were conducted with the Verasonics research scanner (V-1-128, Verasonics Inc., Redmond, WA) and a cardiac phased array transducer (ATL P4-2, 2.5-MHz central frequency, 64 elements, pitch = 0.32 mm, 60% bandwidth); in both cases, raw RF data were acquired using no apodisation during the transmission or reception events and the sampling frequency was set to 10 MHz. RF data were time gain compensated, dynamically beamformed and subsequently demodulated into IQ complex signals. B-mode images obtained with the DCB technique were coherently compounded to enhance their quality, whereas images obtained using focused beams were built from 128 single *A-lines*. In both cases, B-mode images were gamma-corrected ($\gamma = 0.5$) to increase their brightness (except the images used to assess the lateral resolution).

4.2.6 Lateral resolution and CNR *in vitro* assessment

In vitro experiments were first conducted to quantify the lateral resolution and contrast to noise ratio (CNR) of the diverging circular beams technique. The lateral resolution was quantified by measuring the full width at half maximum (*FWHM*) of the impulse response (measured in *mm*). Additionally, the contrast to noise ratio (CNR) was estimated using equation (3.15).

Two different phantoms were used for measuring the image quality of the DCB technique; the first phantom was a tissue mimicking medium with 0.1-mm Nylon threads and 10-mm-diameter low scatter cist inclusions (GAMMEX 403 GS LE); such a phantom allowed estimating the *on-axis* lateral resolution and CNR at 8-cm and the 6-cm depth correspondingly (see Fig. 4.5).

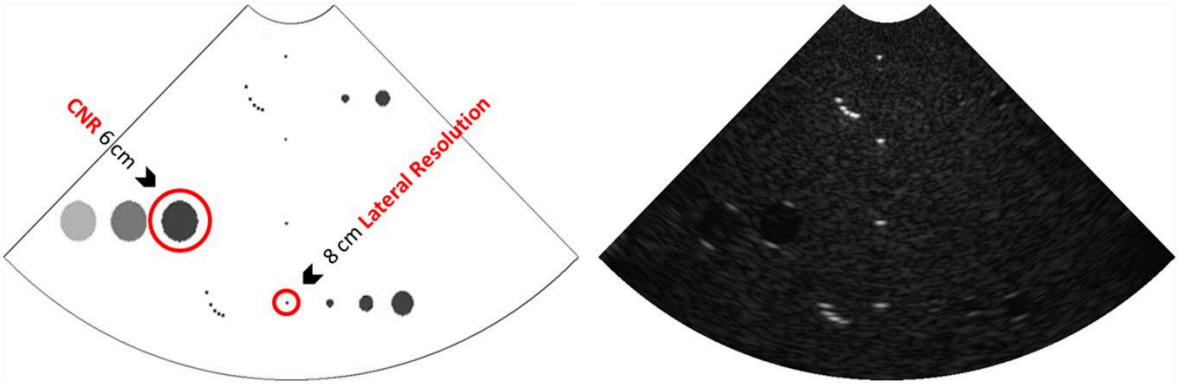

Fig 4.5 – *Tissue mimicking phantom (GAMMEX 403 GS LE).* Schematic chart of the tissue mimicking phantom showing the position of the 0.1-mm Nylon thread and the low scatter cyst inclusion used to measure the on-axis lateral resolution and CNR delivered by the diverging circular beams imaging technique (left panel). B-mode image of the tissue mimicking phantom obtained with the diverging circular beams imaging technique (right panel).

The second phantom was a homemade Nylon threads arrangement used to quantify the *off-axis* lateral resolution of the investigated imaging method (see Fig. 4.6). The second phantom featured multiple 0.1 mm Nylon threads disposed in assorted orientations (0°, 10°, 20°, 30° and 40°) and depths (4-cm, 6-cm and 8-cm). A propagating medium was provided by immersing the phantom into a reservoir filled with distilled water. In order to reconstruct images with the RF data recovered from this phantom, the ultrasound propagation velocity was assumed to be 1480 m/s.

The *on-axis* lateral resolution and CNR delivered by the ultrafast DCB technique were compared to those obtained with the focused SLA approach; the focus of the conventional SLA approach was set to the depth of the threads/cysts being evaluated. The ROI width impact on the *on-axis* lateral resolution was quantified using the GAMMEX phantom. The *off-axis* lateral resolution was evaluated using the threads phantom, and finally the lateral resolution and CNR in tilted images was assessed using the GAMMEX phantom (see section 4.4).

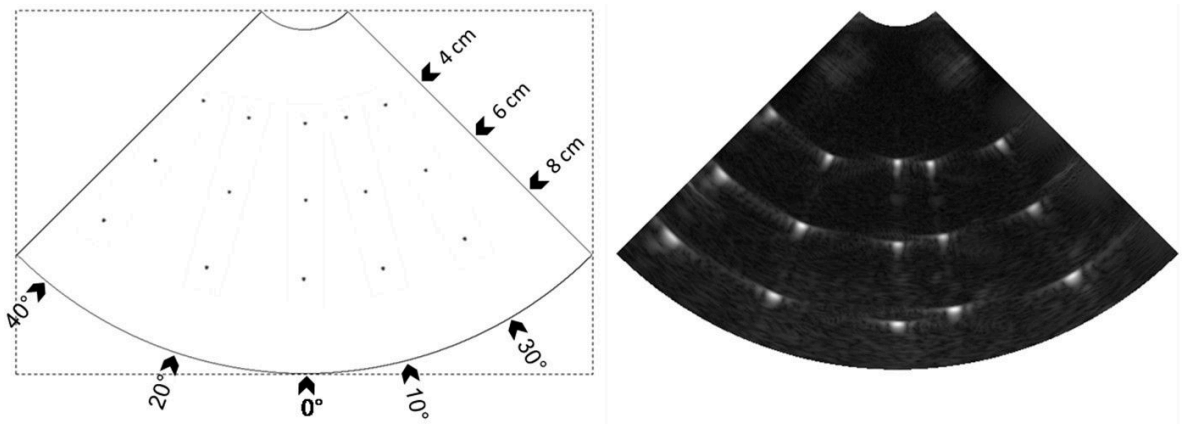

Fig 4.6 – *Nylon threads phantom.* Schematic chart of Nylon threads phantom immersed into water; each point represents the threads that were disposed in various orientations and depths (left panel). B-mode image of the Nylon threads phantom obtained with the diverging circular beams imaging technique (right panel).

4.2.7 *In vivo* examinations

In order obtain a qualitative assessment of the ultrafast B-mode echocardiography technique, *in vivo* acquisitions were performed on a 31 year old volunteer; for such an *in vivo* validation, the echocardiographic examinations were performed using the optimal parameter established with the *in vitro* results. Two main transthoracic views of the heart were captured to illustrate the capabilities of the diverging beams ultrafast echocardiography approach: an apical four-chamber view and a parasternal short axis (mitral valve level). A more detailed description of these figures is given in section 4.3.5.

4.3 Results

The *in vitro* and *in vivo* results delivered by the DCB echocardiography technique are presented in this section. The lateral resolution and CNR were quantified in the middle (*on-axis*) and in the sides (*off-axis*) of a B-mode image using various *in vitro* settings; the thorough assessment presented in the following paragraphs also considered variables such as the number compounding images, the steering range, the ROI width, the sector-scan depth and the tilt angle of the image (see section 4.4.). The results section is concluded by presenting a few *in vivo* examples that allow having a better grasp of the image quality offered by the ultrafast DCB echocardiography technique.

4.3.1 *In vitro* investigation *of the on-axis* lateral resolution and CNR

The *on-axis* lateral resolution and CNR of the DCB echocardiography approach were assessed using a GAMMEX phantom (see section 3.1). The phased array was properly positioned in order to generate the B-mode image presented on Fig. 4.5. – Right panel. The point circled in red was used as target to quantify the lateral resolution (see Fig. 4.5. Left – panel). During the acquisition procedure the Verasonics device parameters were set as following: the sector-scan width ϕ was set to 90°; the angular steering range of was set according to the analysis performed in section 2.3, $\beta_{range} = [-30°:+30°]$; a total of 91 steered diverging beams within the angular steering range were acquired.

The *on-axis* lateral resolution behaviour was inspected at 8 cm deep as a function of the compounded images number. To conduct such a study, steered images were added to the only non-oriented image (image obtained in the middle, $\beta = 0°$); all 91 images were progressively compounded by adding symmetrical pairs (*e.g.* $\pm 10°$… $\pm 15°$…$\pm 20°$ ... etc). The lateral resolution was measured in every resulting compounded image (see Fig. 4.7. black triangles line). As presented in Fig. 4.7, the lateral resolution continued to improve as images obtained from greater steered angles were coherently compounded; therefore, the next step was to reduce the total amount of compounded images to 31, 19 and 13 while maintaining the same steering range ($\beta_{range} = [-30°:+30°]$) (see Fig. 4.7, white stars, black stars and white triangles correspondingly). As shown in Fig. 4.7, although the amount of compound images was reduced, the lateral resolution still converged to the value obtained with all 91 images.

The *on-axis* lateral resolution delivered by both the ultrafast DCB and the focused SLA echocardiography techniques were compared. The Verasonics scanner was set up to aquire128 *A-lines* focused @ 8 cm deep. RF data were treated as described in section 4.2.5

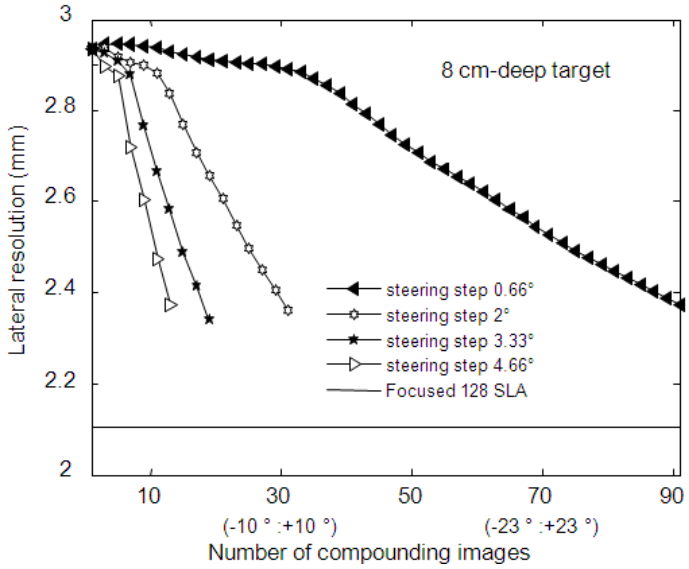

Fig. 4.7 – *On-axis lateral resolution comparison at 8 cm deep between the DCB the focused SLA echocardiography techniques.* The DCB *on-axis* lateral resolution was measured at 8 cm deep as a function of the compounded images number and the steering range. Four different lines (black triangles, white stars, black stars and white triangles) show the lateral resolution behaviour for different amount of compounded images and steering ranges. The continuous black line represents the *on-axis* lateral resolution displayed by the focused SLA approach at 8 cm deep.

to reconstruct a B-mode image; afterwards, the focused SLA technique lateral resolution was quantified (see Fig. 4.7. - black solid line). Results showed that the lateral resolution obtained with the ultrafast DCB and the128 SLA cardiac echo approaches are close, but the SLA lateral resolution is still superior to some extent: 2.37 mm vs 2.1 mm respectively (the lateral resolution of both techniques was quantified at 8 cm deep).

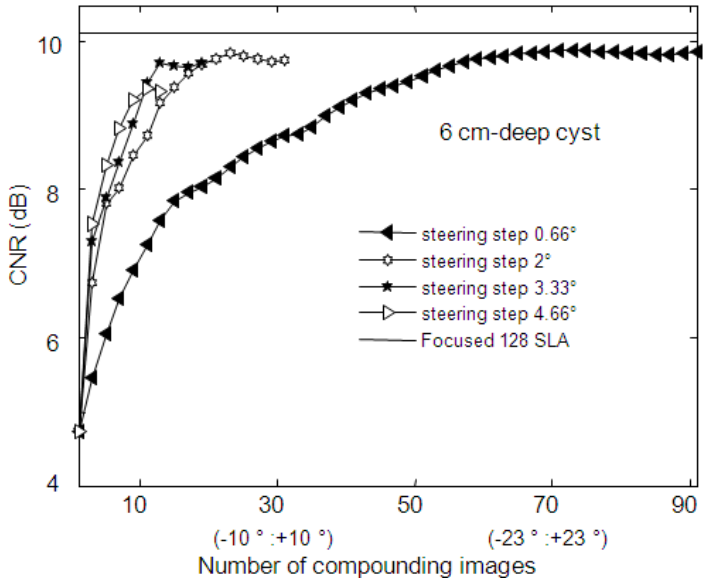

Fig. 4.8 – *On-axis CNR comparison at 6 cm deep between the diverging circular beams and the focused SLA techniques.* The *on-axis CNR* was measure at 6 cm deep as a function of the compounded images number and the steering range. Four different lines (black triangles, white stars, black stars and white triangles) show the *CNR* behaviour for different amount of compounded images and steering ranges. The continuous black line represents the *on-axis CNR* displayed by the focused *SLA* approach at 8 cm deep.

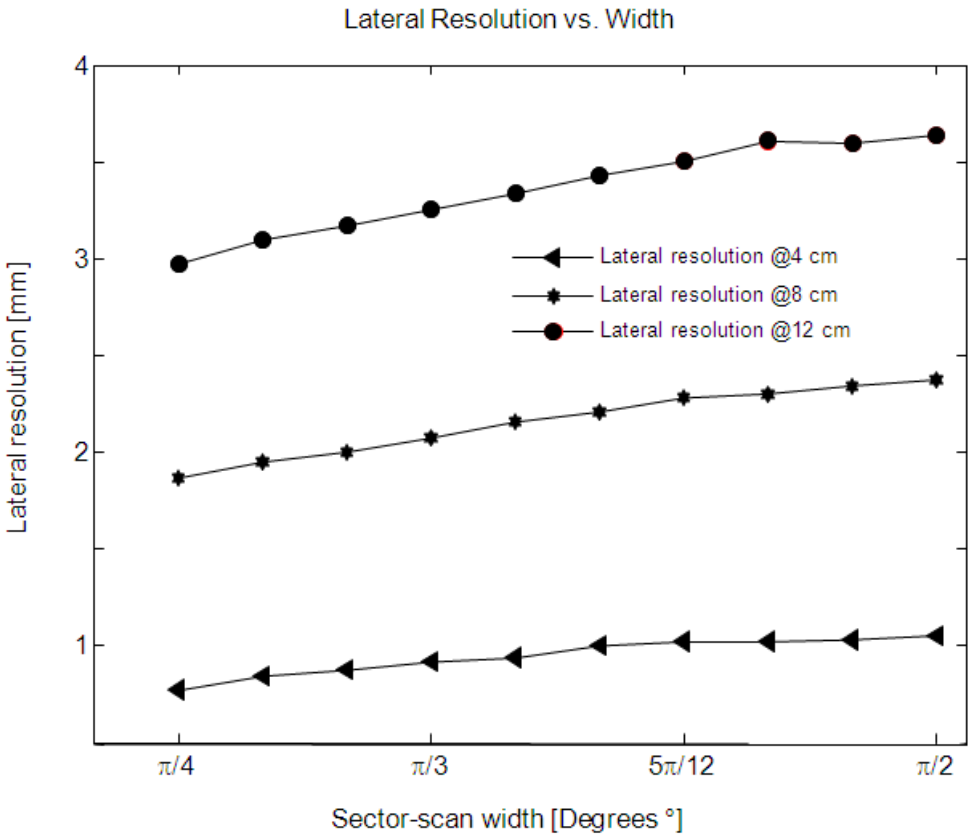

Fig. 4.9 – *On-axis lateral resolution as a function of the sector-scan width.* The *on- axis* lateral resolution was measured at 4, 8 and 12 cm deep as a function of the sector-scan width. The width of the transmitted diverging circular beams was varied between a range of [45°: 90°] with intervals of 5°. B-mode images were formed by compounding 13 images, in which the steering range was defined as explained in section 4.2.4.

As for the *on-axis* lateral resolution, the *on-axis* CNR behaviour was inspected as a function of the number of compounded images at 6 cm deep. The same beamforming strategies described before were used for both the DCB and the SLA focused techniques. The CNR measurement performed in the anechoic cyst in the GAMMEX phantom (see Fig. 4.5) are presented in Fig. 4.8.

As shown in Fig. 4.7, the CNR is enhanced as the number of compounded images increases (see Fig. 4.8 black triangles line). If the number of compounded images is reduced but the angular steering range is kept constant, the CNR still comes near to the CNR value featured by the focused SLA technique (see Fig. 4.8, solid line).

4.3.2 *On-axis* lateral resolution response to the sector-scan width

We have quantified the effect of the sector-scan width ϕ in the *on-axis* lateral resolution. For this experiment the phased array transducer has been aligned with the threads centered in the GAMMEX phantom (see Fig. 4.5). The targets located at 4, 8 and 12-cm-deep were imaged using 13 steered DCB; the number of compounded images was determined considering the results obtained in the previous section. The sector-scan width was varied from 45° to 90° with steps of 5°. The steering ranges were established with the formula proposed in section 4.2.4.

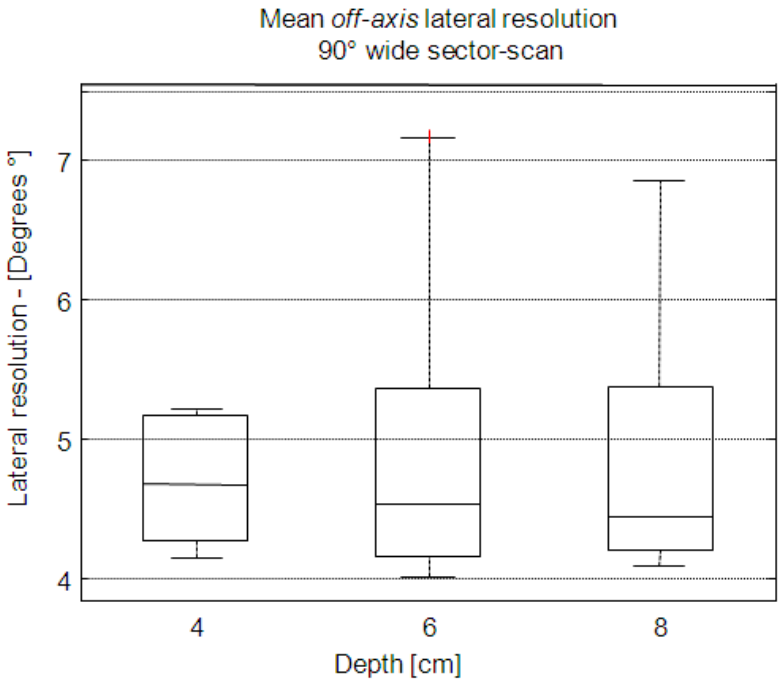

Fig. 4.10 – *Off-axis lateral resolution for a* 90° *wide B-mode scan.* The experiment was conducted using a threads phantom with targets located at 0°, 10°, 20°, 30° and 40° and 4, 6 and 8-cm-deep (see Fig. 4.6). In the boxplot, the *off-axis* lateral resolution is presented in degrees (rather than millimetres) to verify its variability as function of the targets location. Each B-mode frame was obtained compounding 13 images within a steering range of $[-30°:+30°]$.

The lateral resolution was measured at depths 4, 8 and 12 cm by progressively adding pairs of symmetrical images to the solely center image (see Fig. 4.9). As presented in the results, the lateral resolution was enhanced at all three different depths as the sector-scan became narrower (see Fig. 4.9).

4.3.3 *In vitro* investigation of the *off-axis* lateral resolution

The *off-axis* lateral resolution of the DCB imaging technique was investigated using the threads phantom described in section 3.1. The threads phantom immersed into distilled water was insonified with $\phi = 90°$ wide diverging beams; the purpose was to include in the same ROI all targets located at all different orientations (0°, 10°, 20°, 30° and 40°) and depths (4-cm, 6-cm and 8-cm). The angular steering range was set to $[-30°:+30°]$ according to the approach introduced in section 4.2.4, and the amount of coherently compounded images was 13. The experiment was conducted 10 times in order to account for measurements error; the mean *off-axis* lateral resolution at each depth is presented in the boxplot in Fig. 4.10. The lateral resolution was measured in degrees rather than millimetres, to witness the variability as a function of the target location (angular position and the depth in the B-mode image) (see Fig. 4.10).

The mean values corresponding to all three investigated depths (4, 6 and 8-cmm) are presented in Fig. 4.10; the lateral resolution at 4 cm deep exhibits the narrowest variability. The targets at 6 and 8 cm deep present a similar distribution but some outliers are also present at these depths. In general, Fig. 4.10 presents a regular trend for the lateral resolution and a small variation is observed as the targets location changes.

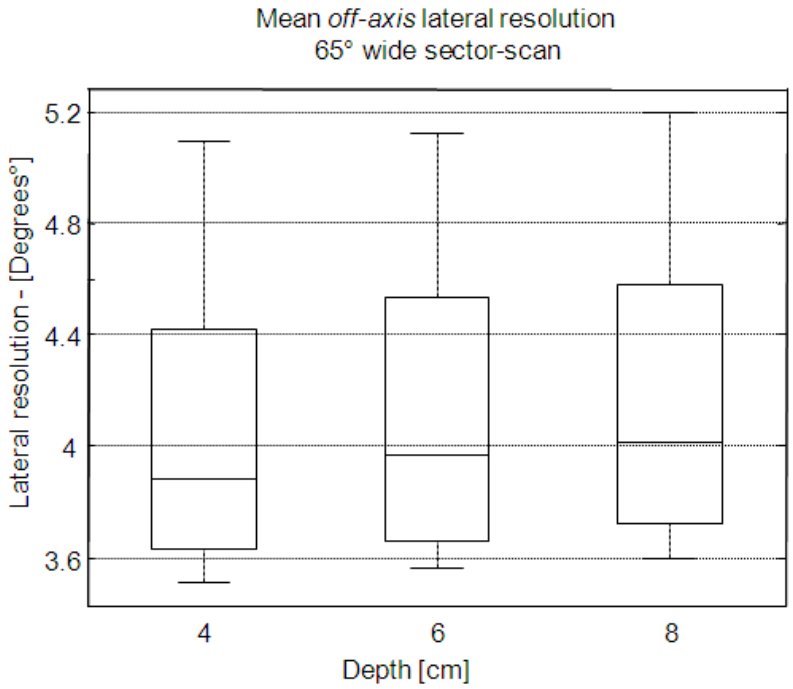

Fig. 4.11 – *Off-axis lateral resolution for a* 65° *wide B-mode scan.* The experiment was conducted using a threads phantom with targets located at 0°, 10°, 20° and 30° and 4, 6 and 8-cm-deep (see Fig. 4.6). In the boxplot, the *off-axis* lateral resolution is presented in degrees (rather than millimetres) to verify its variability as a function of the targets location. The boxplot presents the *off-axis* lateral resolution measured in a 65° wide sectorial scan. Each B-mode frame was obtained compounding 13 images within a steering range of $[-30°: +30°]$.

The same experiment described before was conducted by changing the ROI width ϕ to 65°; due to the narrower width used this occasion, only those targets located within the field of view (0°, 10°, 20° and 30°) were evaluated. The off-axis lateral resolution was quantified in degrees as for the previous *in vitro* experiment; the measurements were conducted 10 times in order to provide mean and deviation values (see Fig. 4.11). The mean lateral resolution range obtained using narrower diverging beams was $[3.6°: 4.6°]$; such a result suggest that as the DCB width decreases, more homogeneous lateral resolution can be obtained all over the image.

4.3.4 Tilted echocardiographic images using diverging circular beams

In conventional echocardiography, narrow tilted B-mode images allow assessing specific structures of the heart; such a tilting feature is conducted without physically rotating the phased-array, but rather using large steering angles. The tilted echocardiography images can be useful when mitral or aortic valves examinations are conducted, in such a case narrow sectorial scans, *e.g.* $\phi = [20°: 40°]$ satisfy the required field of view. In this order of ideas and given the DCB steering capability, we have investigated the image quality of tilted-images obtained with this imaging scheme. *In vitro* experiments have been conducted using the tissue mimicking GAMMEX phantom described in section 4.2.6 (see Fig. 4.5). The width selected for the tilted sectorial scans was $\phi = 20°$, and a total of 15 images were coherently compounded. The angular steering range was selected according to the criteria introduced in section 4.2.4, which in this case corresponded to $[-10°: 10°]$.

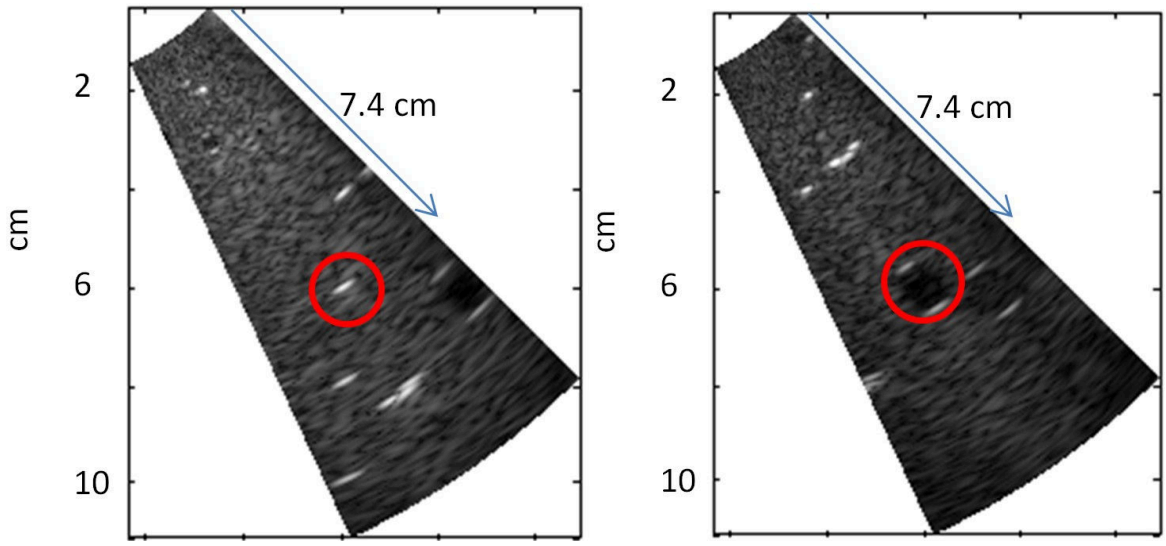

Fig. 4.12 –*Tilted B-mode images obtained using diverging circular beams.* 35° tilted B-mode images indicating the point and cyst used to quantify the lateral resolution and CNR.

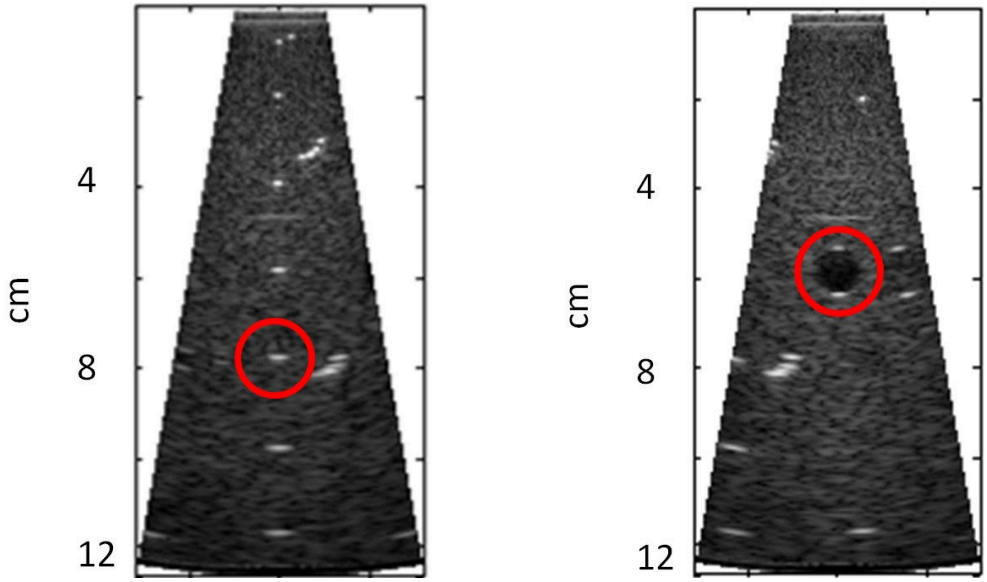

Fig. 4.13 – *Non-tilted B-mode images obtained using diverging circular beams.* Non-tilted and tilted B-mode images indicating the point cysts used to quantify the lateral resolution and CNR.

The tilting angle, which we call ψ, was set to 35°. It is worth noting that the tilting angle introduced in this experiment can be seen as an additional steering angle, so the actual angular steering range used to generate the tilted images was $[25°{:}\,45°]$ (the tilted image axis was then located at 35°, see Fig 4.12).

In order to evaluate the lateral resolution and CNR of the tilted-image, a non-tilted image featuring the same width and steering properties ($\phi = 20°$, $\beta_{range} = [-10°{:}\,10°]$) as the tilted image was used as reference. Since the radial location of the examined features (point target and cyst) was not exactly the same between the non-tilted and tilted images, an approximated comparison was performed. The obtained non-tilted and tilted B-mode images are presented in Fig. 4.13.

The red circles in the B-mode images presented in Fig. 4.13 indicate the features investigated to measure the lateral resolution and CNR (target points and cysts). In the non-tilted images, the lateral resolution and CNR were respectively measured at 6 and 8-cm-deep; in the tilted images, both the lateral resolution and CNR were quantified at 7.4-cm-deep.

The lateral resolution of the non-tilted and tilted images at radial positions of 8 and 7.4-cm-deep respectively are presented in Fig. 4.13. As for the previous lateral resolution experiments, the compounded images number effect was investigated (a maximum of 15 images were coherently compounded). The two lines presented in Fig. 4.13 exhibit very close lateral resolution trends; however, better results are displayed in the tilted case, which might be attributed to the shallower location of the evaluated point in such an image.

The CNR of the non-tilted and tilted images at radial positions of 8 and 7.4-cm-deep respectively are presented in Fig. 4.14. As for the previous lateral resolution experiments, the compounded images number effect was investigated (a maximum of 15 images were coherently compounded). The curve with stars dots in Fig. 4.13 represents the CNR measured in the non-tilted image; it can be seen that for a non-compounded frame, non-tilted images feature a higher CNR. Conversely, the CNR converges to very similar values as compounding is introduced (7 compounded images reach similar CNR).

The results presented in Figs. 4.13 and 4.14 suggest that tilted-images and non-tilted B-mode images delivered by the DCB imaging scheme feature comparable properties (lateral resolution and CNR). These results have been validated using steering range and maximal steering angle β_{max} introduced in section 4.2.4.

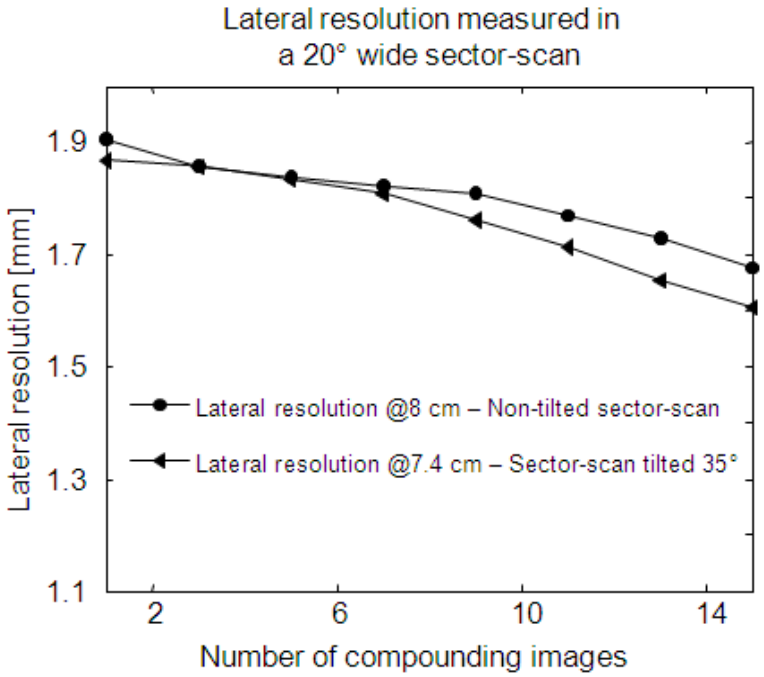

Fig. 4.14 – *Lateral resolution comparison between non-tilted and tilted B-mode images.* Lateral resolution comparison between non-tilted and tilted images obtained with the DCB imaging scheme. The lateral resolution was measured at 8 and 7.4-cm-deep in the non-tilted and tilted images respectively.

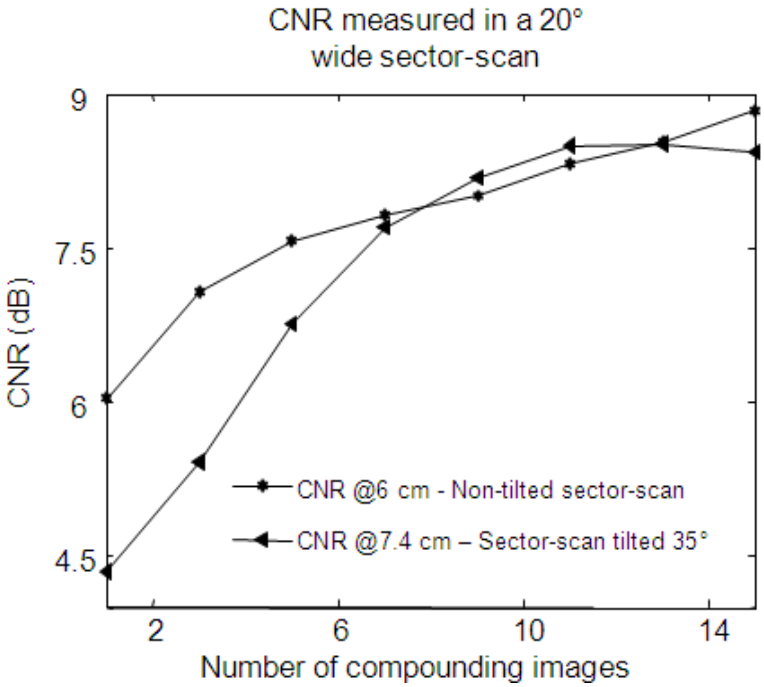

Fig. 4.15 – *CNR comparison between non-tilted and tilted B-mode images.* CNR comparison between non-tilted and tilted images obtained with the DCB imaging scheme. The CNR was measured at 8 and 7.4-cm-deep in the non-tilted and tilted images respectively.

4.3.5 *In vivo* results

The DCB ultrafast echocardiography approach was used to conduct an echocardiography examination on a 31 years old healthy volunteer. The four-chamber view presented in Fig. 4.15 was obtained with the ultrafast approach.

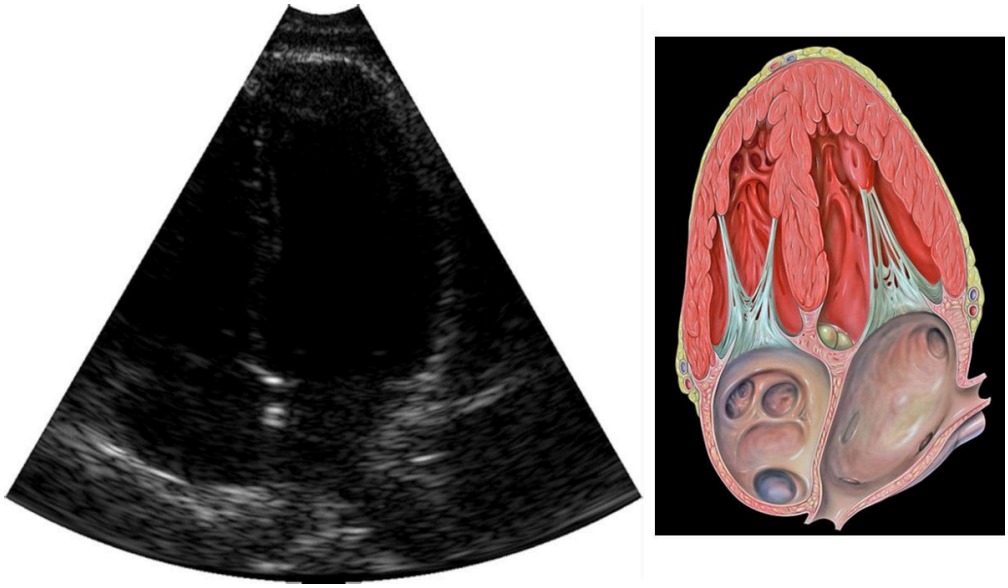

Fig. 4.16 – *Cardica four chambers view obtained in a healthy volunteer using the diverging circular beam (DCB) ultrafast echocardiography approach.*

The captured field of view features a depth of 15 cm, which allowed for a maximal PRF of 5.1 KHz. A total of 13 images were coherently compounded to generate each B-mode frame, resulting in an effective frame rate of 395 fps.

A short axis view was also obtained in the same volunteer using the ultrafast echocardiography technique. In such a case the maximal depth was to 10 cm which allowed increasing the frame rate to 7 KHz, therefore obtaining an effective frame rate of 538 fps. An image obtained in this *in vivo* examination is presented in Fig. 4.16.

Fig. 4.17 – *Cardiac short axis view obtained in a healthy volunteer using the diverging circular beam (DCB) ultrafast echocardiography approach.*

4.4 Conclusion

The ultrafast echocardiography approach using DCB displayed comparable lateral resolution and CNR to those exhibited by the conventional focused SLA echocardiography technique. *In vitro* results proved that the lower image quality resulting from the ultrafast ultrasound implementation in echocardiography can be compensated with the use of coherent compounding. Furthermore, the obtained image quality made it possible to perform *in vivo* echocardiographic examinations at much higher temporal resolutions (between 395 to 538 fps) compared to the conventional focused echocardiography approach (~ 60 fps).

In this chapter the DCB echocardiography approach has been thoroughly investigated. Image quality features such as the lateral resolution and CNR were quantified using multiples *in vitro* scenarios. Also, the DCB cardiac echo technique was used to conduct an

in vivo examination in a healthy volunteer; the obtained images were qualitatively assessed by a cardiologist as satisfactory.

In the following chapter the high frame rate of the DCB approach has been used to extend the non-ambiguous color Doppler Nyquist velocity range in echocardiographic images. The implemented methodology has been inspired by a radar application which we have validated *in vitro* and *in vivo*.

Bibliography

[1] L. Mertens and M. K. Friedberg, "The gold standard for noninvasive imaging in congenital heart disease: echocardiography," *Current opinion in cardiology,* vol. 24, pp. 119-124, 2009.

[2] P. Lancellotti*, et al.*, "European Association of Echocardiography recommendations for the assessment of valvular regurgitation. Part 1: aortic and pulmonary regurgitation (native valve disease)," *European Journal of Echocardiography,* vol. 11, pp. 223-244, 2010.

[3] P. Lancellotti*, et al.*, "European Association of Echocardiography recommendations for the assessment of valvular regurgitation. Part 2: mitral and tricuspid regurgitation (native valve disease)," *European Journal of Echocardiography,* vol. 11, pp. 307-332, 2010.

[4] M. A. Quinones*, et al.*, "A new, simplified and accurate method for determining ejection fraction with two-dimensional echocardiography," *Circulation,* vol. 64, pp. 744-753, 1981.

[5] J. Bercoff, "Ultrafast ultrasound imaging," *Ultrasound Imaging-Medical Applications. InTech,* 2011.

[6] P. P. Sengupta*, et al.*, "Left Ventricular Isovolumic Flow Sequence During Sinus and Paced RhythmsNew Insights From Use of High-Resolution Doppler and Ultrasonic Digital Particle Imaging Velocimetry," *Journal of the American College of Cardiology,* vol. 49, pp. 899-908, 2007.

[7] G.-R. Hong*, et al.*, "Characterization and quantification of vortex flow in the human left ventricle by contrast echocardiography using vector particle image velocimetry," *JACC: Cardiovascular Imaging,* vol. 1, pp. 705-717, 2008.

[8] S. Fadnes*, et al.*, "Shunt Flow Evaluation in Congenital Heart Disease Based on Two-Dimensional Speckle Tracking," *Ultrasound in medicine & biology,* vol. 40, pp. 2379-2391, 2014.

[9] A. Swillens*, et al.*, "Two-dimensional blood velocity estimation with ultrasound: speckle tracking versus crossed-beam vector Doppler based on flow simulations in a carotid bifurcation model," *Ultrasonics, Ferroelectrics and Frequency Control, IEEE Transactions on,* vol. 57, pp. 327-339, 2010.

[10] D. Garcia*, et al.*, "Two-dimensional intraventricular flow mapping by digital processing conventional color-Doppler echocardiography images," *Medical Imaging, IEEE Transactions on,* vol. 29, pp. 1701-1713, 2010.

[11] G. Montaldo, *et al.*, "Coherent plane-wave compounding for very high frame rate ultrasonography and transient elastography," *Ultrasonics, Ferroelectrics and Frequency Control, IEEE Transactions on,* vol. 56, pp. 489-506, 2009.

[12] J. Udesen, *et al.*, "High frame-rate blood vector velocity imaging using plane waves: simulations and preliminary experiments," *Ultrasonics, Ferroelectrics and Frequency Control, IEEE Transactions on,* vol. 55, pp. 1729-1743, 2008.

[13] J. Bercoff, *et al.*, "Ultrafast compound doppler imaging: providing full blood flow characterization," *Ultrasonics, Ferroelectrics and Frequency Control, IEEE Transactions on,* vol. 58, pp. 134-147, 2011.

[14] D. P. Shattuck, *et al.*, "Explososcan: A parallel processing technique for high speed ultrasound imaging with linear phased arrays," *The Journal of the Acoustical Society of America,* vol. 75, pp. 1273-1282, 1984.

[15] H. Hasegawa and H. Kanai, "High-frame-rate echocardiography using diverging transmit beams and parallel receive beamforming," *Journal of Medical Ultrasonics,* vol. 38, pp. 129-140, 2011.

[16] B.-F. Osmanski, *et al.*, "Ultrafast Doppler Imaging of Blood Flow Dynamics in the Myocardium," *Medical Imaging, IEEE Transactions on,* vol. 31, pp. 1661-1668, 2012.

[17] C. Papadacci, *et al.*, "High-contrast ultrafast imaging of the heart," *IEEE transactions on ultrasonics, ferroelectrics, and frequency control,* vol. 61, pp. 288-301, 2014.

[18] M. Couade, *et al.*, "*In vivo* quantitative mapping of myocardial stiffening and transmural anisotropy during the cardiac cycle," *Medical Imaging, IEEE Transactions on,* vol. 30, pp. 295-305, 2011.

[19] A. Selfridge, *et al.*, "A theory for the radiation pattern of a narrow-strip acoustic transducer," *Applied Physics Letters,* vol. 37, pp. 35-36, 1980.

Chapter 5

This chapter introduces the staggered multiple-PRF technique that was taken advantage of to extend echocardiography color Doppler Nyquist velocity. *In vitro* as well as *in vivo* experiments were conducted to validate such an approach; the results presented in this article prove the staggered PRF strategy succeeded to broaden the echocardiography unambiguous color Doppler velocity range without introducing significant errors. Multiple applications that can benefit of such an improvement are pointed out in this chapter.

Staggered multiple-PRF ultrafast color Doppler

Daniel Posada [1,2], Arnaud Pellissier [3], Boris Chayer [2,4], François Tournoux [2,3,4], Guy Cloutier [2,4,5], Damien Garcia [1,2,4,5]

[1] RUBIC, Research Unit of Biomechanics and Imaging in Cardiology

[2] CRCHUM, Research Center, University of Montreal Hospital, Canada

[3] Department of Echocardiography, CHUM, Montreal, University of Montreal Hospital, Canada

[4] LBUM, Laboratory of Biorheology and Medical Ultrasonics

[5] Department of Radiology, Radio-Oncology and Nuclear Medicine, and Institute of Biomedical Engineering, University of Montreal, Canada

Abstract **–** Color Doppler imaging is an established pulsed-ultrasound technique to visualize blood flow non-invasively. Ultrafast color Doppler, by emissions of plane or circular wavefronts, allows 10- to 100-fold increase in frame rates. Conventional and ultrafast color Doppler are limited by the range-velocity dilemma, which may result in velocity folding (aliasing) for large depths and/or large velocities. We investigated multiple-PRF emissions arranged in a series of alternating (staggered) intervals to remove aliasing in ultrafast color Doppler. We tested staggered dual- and triple-PRF ultrafast color Doppler 1) *in vitro* in a spinning disc and a free jet flow, and 2) *in vivo* in a human carotid and left heart. The in vitro results showed that the Nyquist velocity could be extended to up to 6 times the conventional limit. We found excellent agreements between the de-aliased and ground-truth velocities. Consistent de-aliased Doppler images were also obtained in both the human carotid and left heart. Our results demonstrated that staggered multiple-PRF ultrafast color Doppler was efficient for high-velocity high-frame-rate blood flow imaging.

Keywords – Staggered multiple-PRF, Ultrafast color Doppler, Nyquist velocity extension, De-aliasing

5.1 Introduction

Color Doppler ultrasound is the most widespread clinical imaging modality to analyze the blood circulation. It maps the blood flow, non-invasively and in real time, by transmitting uniformly spaced ultrasound pulses. Color Doppler ultrasound imaging has been used mainly as a qualitative instrument. Typical echocardiographic applications include *e.g.* visualization of valvular regurgitations, detection of septal defects, or guiding the position of the PW (pulsed wave) sample volume. Recent innovative tools have been introduced to make color Doppler more quantitative. For example, it can better decipher the intracardiac flow dynamics by using vector flow mapping or Doppler vortography – vector flow mapping enables reconstruction of 2D flow velocity fields in cardiac cavities [1;2], and Doppler vortography can assess the blood flow vortices [3]. These tools are potentially relevant since recent clinical papers reveal that the dynamics of the main intraventricular vortex may be related to the cardiac function [4;5]. The intracardiac flow is highly transient; to get a time-resolved flow analysis, successive cardiac cycles must be thus temporally registered to compensate for the low frame rates associated to conventional Doppler echo (typically < 20 fps for cardiac applications). Outcomes, however, can be affected due to beat-to-beat variability present in most patients. Another limitation for quantitative color Doppler techniques is the presence of aliasing (i.e. velocity folding) which must be corrected in post-processing [6]. Aliasing occurs when the flow information is sampled insufficiently. As Doppler velocity exceeds a certain magnitude, it is aliased (wrapped around) to the opposite side of the Doppler spectrum [7]. In the classical red-blue colormap, aliased velocities wrap around so that color information turns from red to blue or vice versa. With the purpose of optimizing quantitative color Doppler, we addressed these two issues. We investigated multiple-PRF emissions arranged in a series of alternating (staggered) intervals to remove aliasing. To attain high frame rates, staggered emissions were implemented in an ultrafast ultrasound scanner by emitting plane [8] or diverging [9] wavefronts. Before getting into the issue of staggered multiple-PRF ultrafast color Doppler, we briefly introduce ultrafast ultrasound and aliasing in the context of color Doppler imaging.

5.1.1 Ultrafast color Doppler

Conventional color Doppler reaches limited temporal resolutions because several series of focused beams are needed to generate one image. Plane wave emissions were proposed to override the frame rate limitation and broaden the clinical perspectives of blood flow ultrasound imaging [8;10]. Accurate flow imaging in the carotid arteries is one of the promising potentials of plane wave Doppler [11-13]. Diverging beams have also been proposed to exploit the benefits of ultrafast ultrasound in cardiac Doppler imaging [14-16]. Recently, ultrafast color Doppler has been extended to 3D in several physiological contexts [17]. It is likely that ultrafast color Doppler may supplant conventional color Doppler in the near future. The possibility to increase the frame rate tenfold indeed offers new opportunities in flow imaging.

5.1.2 Aliasing in color Doppler imaging

Both in conventional and ultrafast color Doppler imaging, a series of pulses is transmitted to estimate the velocity of moving scatterers. According to the Nyquist-Shannon sampling theorem, there is a maximum speed that can be determined without ambiguity. This speed limit is referred to as the Nyquist velocity (V_{N}):

$$V_{\mathrm{N}} = \frac{\mathrm{PRF}\,\lambda}{4}, \tag{5.1}$$

where PRF (pulse repetition frequency) is the number of ultrasound transmits per second (i.e. the fast-time sampling frequency), and λ is the wavelength associated to the transducer central frequency. Aliasing occurs when absolute Doppler velocities higher than the Nyquist velocity (Eq. 5.1) are folded back into the Nyquist interval. The time lag between two consecutive pulses (pulse repetition period, PRP = 1/PRF) also limits the maximum depth that can be imaged, since the PRP must be long enough to allow back-and-forth traveling of transmitted echoes. The color Doppler trade-off between the maximum range depth (r_{max}) and the maximum velocity can be expressed by the following range-velocity product:

$$r_{\mathrm{max}}\, V_{\mathrm{N}} = \frac{c\lambda}{8}, \tag{5.2}$$

where c is the speed of sound (~1540 m/s in soft tissues). For a given wavelength, Eq. (5.2) illustrates that it is generally impossible to measure high flow velocities without ambiguity in deep tissues. For instance, using a 2.5 MHz cardiac phased-array and a maximum range of 20 cm (as with an apical long axis view in an adult), a maximum speed of only 0.6 m/s can be measured. Typical mitral E-wave velocities are ~0.8 m/s and can be >1 m/s in patients with restrictive filling [18]. Aliasing is therefore prevalent in Doppler echocardiography.

5.1.3 Extending the Nyquist velocity

In this study, we took advantage of the high frame rate of ultrafast ultrasound to extend the Nyquist limit of color Doppler. We employed multiple-PRF schemes inspired from weather radars and staggered the period between pulses to disambiguate the Doppler fields; with this form of staggered PRF, pairs of pulses, transmitted with a fixed time lag between each pulse, are interleaved with other pairs transmitted with a slightly different interval (see fig. 5.1). By combining the resulting Doppler fields, it is possible to extend the Nyquist velocity several folds to produce a dealiased Doppler image. For this purpose, we developed an original and simple numerical method. In the following, we first describe the staggered multiple-PRF method and our dealiasing procedure. We then present *in vitro* results obtained in a spinning disk and in a free jet flow. We finally illustrate the efficacy of our approach using *in vivo* ultrafast Doppler data acquired in a human carotid and left heart.

5.2 Methods

5.2.1 Existing dual-PRF techniques

Several techniques have been proposed to extend the Nyquist velocity of pulsed-wave spectral (PW) Doppler in medical ultrasound imaging [19;20]. In particular, some works inspired by Doppler weather radars [21] have introduced the use of two different pulses. Emission of different pulses suitably combined can indeed lead to a several-fold increase in the actual Nyquist velocity [22]. Newhouse *et al*. [20] was the first to propose the use of two different PRFs to increase the range-velocity limit in PW Doppler. Nishiyama *et al*. and Nogueira *et al*. later proposed the use of staggered dual-PRF sequences to extend the non-ambiguous velocity interval [23;24]. Their methods were similar to the one proposed in the weather radar literature. In this technique, lag-one autocorrelation estimates are combined so that the velocity is obtained from the phase difference of the two [25]. Nitzpon *et al*. used another tactic and described a system equipped with a transmitter capable of generating pulses with two different carrier frequencies. This system produced two velocity estimates sequentially which were joined to measure blood velocities beyond the Nyquist limit [26;27].

The dual-PRF approaches were originally proposed in the 70's to solve the aliasing problem in weather Doppler radars [28]. Dual-PRF pulsing strategy is nowadays implemented in many types of meteorological radars. In this paper, we propose a multiple-PRF strategy, *i.e.* the number of different PRFs is not limited to 2. In the next "Theoretical background" subsection, we describe this multiple-PRF approach and explain how the additional PRFs must be chosen. We also put forward a new dealiasing procedure based on the estimation of the Nyquist numbers and provide a thorough theoretical description. This technique was tested with 2 and 3 staggered PRFs. The proposed method simply results in a lookup table, as explained below.

5.2.2 Theoretical background – Staggering the PRF to extend the Nyquist velocity

Aliasing occurs when the absolute value of the Doppler velocity exceeds the Nyquist velocity. The unambiguous Doppler velocity (V_{D}^{u}) is related to the measured Doppler velocity (V_{D}) by [29]:

$$V_{\mathrm{D}} = V_{\mathrm{D}}^{u} - 2\, n_{\mathrm{N}} V_{\mathrm{N}}, \tag{5.3}$$

where n_{N} is the Nyquist number (with $n_{\mathrm{N}} \in \mathbb{Z}$). The Nyquist number can be expressed as (see the demonstration in the appendix):

$$n_{\mathrm{N}} = \mathrm{floor}\left(\frac{V_{\mathrm{D}}^{u} + V_{\mathrm{N}}}{2\, V_{\mathrm{N}}}\right), \tag{5.4}$$

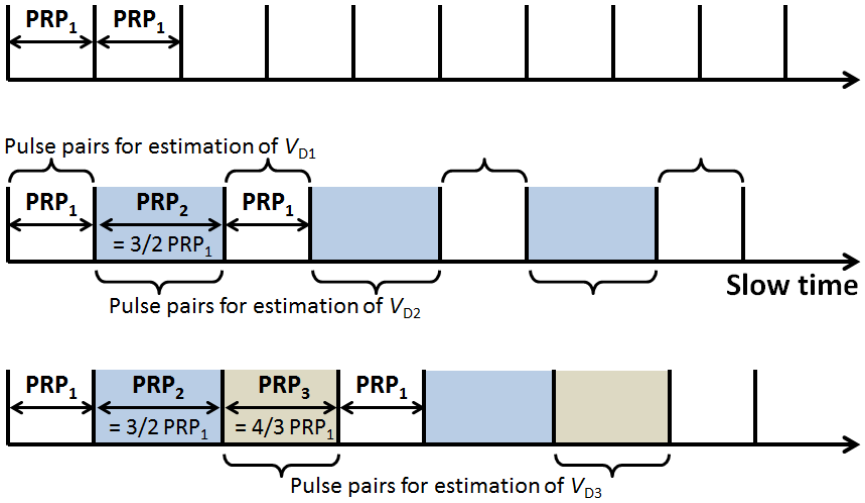

Fig. 5.1 – *Staggered multiple-PRF sequences.* The top sequence represents the conventional equally-spaced transmission strategy (PRP = pulse repetition period). The respective 2nd and 3rd sequences represent dual- and triple-PRF schemes; pairs of pulses are emitted with delay laws changing sequentially. These pulse pairs are used to generate several Doppler images (V_{D_i}), which are combined to disambiguate the Doppler velocity field.

where floor( ) denotes the largest previous integer. The Doppler velocity is aliased when $n_{\mathrm{N}} \neq 0$. Staggering two or more pulse repetition frequencies can help to determine the Nyquist number up to some extent, as we will see below. Fig. 5.1 illustrates three different pulsing sequences: the conventional equally spaced pulsing sequence, as well as staggered PRF sequences in which pulses are interlaced using two or three different PRFs. Sirmans *et al*. described how the staggered PRF mode can be used to broaden the unambiguous velocity interval [28]. Their method determines two Doppler velocities V_1 and V_2, the first one from the paired pulses delayed of PRP_1 (pulse repetition period #1) the second one from the paired pulses delayed of PRP_2 (pulse repetition period #2). To extend the unambiguous velocity range, one of the Doppler estimates is adjusted by an amount dictated by the Doppler velocity difference $(V_2 - V_1)$. We developed a derived approach and generalized this concept by seeking the Nyquist numbers. We here give an in-depth theoretical analysis and describe how the supplementary PRFs must be selected.

Let PRF_1 (pulse repetition frequency #1) correspond to the greater PRF. A typical value for PRF_1 can be selected according to the maximal range depth to avoid overlaid echoes:

$$\mathrm{PRF}_1 = \frac{c}{2\, r_{\max}}, \tag{5.5}$$

whose corresponding Nyquist velocity is deduced from Eq. (5.1):

$$V_{\mathrm{N}_1} = \frac{\mathrm{PRF}_1\, \lambda}{4}. \tag{5.6}$$

A staggered multiple-PRF approach can extend the Nyquist velocity given by (5.6). Although we used a dual- or triple-PRF strategy in this study, as illustrated in fig. 5.1, the following description remains valid for any number of interleaved PRFs. In addition to the main pulse repetition frequency PRF_1, supplementary smaller PRFs (PRF_i, with $i > 1$) are implemented to make the full emission sequence staggered (see fig. 5.1):

$$\mathrm{PRF}_i = \frac{p_i}{q_i}\mathrm{PRF}_1, \tag{5.7}$$

with p_i and q_i positive integers such that $p_i = q_i = 1$ if $i = 1$, and $p_i < q_i$ and $(p_i,q_i) = 1$ (i.e., relatively prime) otherwise. Note that we also have (from Eq. 5.1):

$$V_{\mathrm{N}_i} = \frac{p_i}{q_i}V_{\mathrm{N}_1}. \tag{5.8}$$

In a staggered multiple-PRF scheme, the extended Nyquist velocity $\left(V_{\mathrm{N_e}}\right)$ is the smallest velocity that verifies $V_{\mathrm{N}_e} = n_i V_{\mathrm{N}_i}$, $\forall\, i \geq 1$, where n_i is a positive integer [30]. According to (5.8), the extended Nyquist velocity is thus given by [30]:

$$V_{\mathrm{N_e}} = \mathrm{lcm}(p_2, \ldots, p_i, \ldots)\, V_{\mathrm{N}_1} \equiv k\, V_{\mathrm{N}_1}, \tag{5.9}$$

where lcm denotes the least common multiple. The particular case of a triple-PRF scheme, with $\mathrm{PRF}_2 = \frac{2}{3}\mathrm{PR}_1$ and $\mathrm{PRF}_3 = \frac{3}{4}\,\mathrm{PRF}_1$, provides a six-fold increase in the Nyquist velocity interval since equation (5.9) gives $V_{\mathrm{N_e}} = \mathrm{lcm}(2,3)\, V_{\mathrm{N}_1} = 6\, V_{\mathrm{N}_1}$. Equation (5.9) shows that the larger the integers p_i, the larger is the extended Nyquist velocity. In practice, however, they cannot be too large, as we will see later.

A multiple-PRF scheme gives rise to several Doppler velocities (V_{D_i}) which all verify equation (5.3):

$$V_{\mathrm{D}}^{u} = V_{\mathrm{D}_i} + 2\, n_{\mathrm{N}_i} V_{\mathrm{N}_i}, \tag{5.10}$$

where n_{N_i} and V_{N_i} are the corresponding Nyquist number and Nyquist velocity. To mitigate the effects of velocity ambiguities, we need to obtain the Nyquist numbers n_{N_i}. The unambiguous Doppler velocities can be resolved whenever their absolute values are less than the extended Nyquist velocity $V_{\mathrm{N_e}} = k\, V_{\mathrm{N}_1}$:

$$|V_{\mathrm{D}}^{u}| < k\, V_{\mathrm{N}_1}. \tag{5.11}$$

Applying equation (5.4), it can be shown that this remains true if the Nyquist numbers are bounded by (see the demonstration in the appendix):

$$\left|n_{\mathrm{N}_i}\right| \leq \mathrm{ceiling}\left(\frac{k\, q_i}{2\, p_i} - \frac{1}{2}\right), \tag{5.12}$$

where ceiling( ) denotes the smallest following integer. To disambiguate the Doppler velocity field, we need the Nyquist numbers n_{N_i} in (5.10). Combining equations (5.8) and (5.10) gives:

$$q_i \frac{V_{\mathrm{D}_i} - V_{\mathrm{D}_1}}{2V_{\mathrm{N}_1}} = n_{\mathrm{N}_1} q_i - n_{\mathrm{N}_i} p_i. \tag{5.13}$$

The right-hand side in (5.13) is an integer. But, in practice, the left-hand side is not an integer due to observational errors in the measured Doppler velocities. Equation (5.13) is thus rewritten as:

$$\mathrm{nint}\left(q_i \frac{V_{\mathrm{D}_i} - V_{\mathrm{D}_1}}{2V_{\mathrm{N}_1}}\right) = n_{\mathrm{N}_1} q_i - n_{\mathrm{N}_i} p_i, \tag{5.14}$$

where nint( ) denotes the nearest integer. In a multiple-PRF design with N_{PRF} PRFs related by (5.8), equation (5.14) leads to an undetermined system with N_{PRF} unknowns (i.e. the Nyquist numbers, n_{N_i}) and $(N_{\mathrm{PRF}} - 1)$ independent equations. The Nyquist numbers, however, are constrained by the inequality (5.12), which guarantees the uniqueness of the solution. Another constraint limiting their ranges is also given by (see the demonstration in the appendix):

$$\left|n_{\mathrm{N}_1} q_i - n_{\mathrm{N}_i} p_i\right| \leq \frac{1}{2}(p_i + q_i). \tag{5.15}$$

For example, let us illustrate a dual-PRF scheme with $\mathrm{PRF}_2 =$ ¾ PRF_1, *i.e.* $p_2 = 3$ and $q_2 = 4$. According to the expression of the extended Nyquist velocity (5.9), we have $k = 3$. The inequality (5.12) yields the ranges for the Nyquist numbers, which are in this case: $\left|n_{\mathrm{N}_1}\right| \leq 1$ and $\left|n_{\mathrm{N}_2}\right| \leq 2$. The different value combinations given by (5.14) under the additional constraint (5.15) are given in Table 5.1. A triple-PRF scheme with $\mathrm{PRF}_2 =$ ⅔ PRF_1 and $\mathrm{PRF}_3 =$ ¾ PRF_1 (*i.e.* $p_2 = 2$, $q_2 = 3$ and $p_3 = 3$, $q_3 = 4$) provides 33 possible combinations given in Table 5.2 in the appendix.

Table 5.1 – Lookup table for the Nyquist numbers. This table illustrates how equation (5.14) is used to determine the Nyquist numbers. It represents a dual-PRF scheme with $p_2 = 3$ and $q_2 = 4$. The expression of the first column (Eq. 5.14) is calculated, for each pixel, from the Doppler velocities V_{D_i}. Each value is paired with a unique combination of Nyquist numbers $(n_{\mathrm{N}_1}, n_{\mathrm{N}_2})$. See also Table 5.2 in the appendix for an illustration of a triple-PRF scheme.

$\mathrm{nint}\left(q_2 \frac{V_{\mathrm{D}_2} - V_{\mathrm{D}_1}}{2V_{\mathrm{N}_1}}\right)$	$\boldsymbol{n_{\mathrm{N}_1}}$	$\boldsymbol{n_{\mathrm{N}_2}}$
-3	0	1
-2	1	2
-1	-1	-1
0	0	0
1	1	1
2	-1	-2
3	0	-1

This example shows how our dealiasing process works: i) Calculate the first term of equation (5.14), at any pixel, from the Doppler images V_{D_i} $(i \geq 2)$; ii) Determine the corresponding Nyquist numbers (n_{N_i}) using a lookup table (such as Table 5.1, see also Table 5.2 in the appendix); iii) Deduce the unambiguous Doppler velocity using a weighted mean issued from expression (10):

$$V_{\mathrm{D}}^u = \frac{\sum_i \frac{p_i}{q_i} V_{\mathrm{D}}^u}{\sum_i \frac{p_i}{q_i}} = \frac{\sum_i \frac{p_i}{q_i} (V_{\mathrm{D}_i} + 2\, n_{\mathrm{N}_i} V_{\mathrm{N}_i})}{\sum_i \frac{p_i}{q_i}}. \tag{5.16}$$

Theoretically, the larger the integers p_i, the better is the Nyquist interval extension (see Eq. 5.9). Large p_i, however, can lead to erroneous Nyquist numbers, as we will now explain. Relating the measured Doppler velocities (V_{D_i}) to the expected Doppler velocities $(\widetilde{V_{\mathrm{D}_i}})$ by $V_{\mathrm{D}_i} = \widetilde{V_{\mathrm{D}_i}} + \epsilon_i$, where ϵ_i is the measurement error, equation (5.14) becomes:

$$\mathrm{nint}\left(q_i \frac{\widetilde{V_{\mathrm{D}_i}} - \widetilde{V_{\mathrm{D}_1}} + \epsilon_i - \epsilon_1}{2V_{\mathrm{N}_1}}\right) = \mathrm{nint}\left(q_i \frac{\widetilde{V_{\mathrm{D}_i}} - \widetilde{V_{\mathrm{D}_1}}}{2V_{\mathrm{N}_1}} + q_i \frac{\epsilon_i - \epsilon_1}{2V_{\mathrm{N}_1}}\right) = n_{\mathrm{N}_1} q_i - n_{\mathrm{N}_i} p_i. \tag{5.17}$$

Since, by definition, $\left(q_i \frac{\widetilde{V_{\mathrm{D}_i}} - \widetilde{V_{\mathrm{D}_1}}}{2V_{\mathrm{N}_1}}\right)$ is an integer $(= n_{\mathrm{N}_1} q_i - n_{\mathrm{N}_i} p_i)$, this equation remains true as long as

$$\max\left|q_i\frac{\epsilon_i-\epsilon_1}{2V_{\mathrm{N}_1}}\right| < 0.5 \text{ i.e., } \max|q_i(\epsilon_i-\epsilon_1)| < V_{\mathrm{N}_1}. \quad (5.18)$$

The variance of the Doppler velocity estimate is proportional to the pulse repetition frequency [31]. Therefore, assuming from equation (5.8) that $\epsilon_i \sim \sqrt{p_i/q_i}\,\epsilon_1$, we obtain the sufficient condition

$$\left(\sqrt{p_i q_i}+q_i\right)\max|\epsilon_1| < V_{\mathrm{N}_1}. \quad (5.19)$$

Inequality (5.19) shows that, for a given error distribution ϵ_1, both p_i and q_i cannot be too large to ensure the validity of expression (5.14) in most conditions. Because $p_i < q_i$ and $(p_i,q_i) = 1$ (for $i > 1$), it is convenient to choose $q_i = p_i + 1$. In our experimental studies, we used the ratios $p_i/q_i = 2/3$ and 3/4. These values are common in Doppler radar and usually do not exceed 6/7 [30].

5.2.3 In vitro analysis – spinning disc and free jet flow

We first tested staggered multiple-PRF ultrafast color Doppler on a 10-cm-diameter tissue-mimicking disc. This disc was mounted on a step motor which allowed control of its rotational speed [32]. The composition of the tissue-mimicking disc was agar 3%, Sigmacell cellulose powder 3%, glycerol 8% and water. The phantom rotated at angular velocities ranging from 9 to 270 revolutions per minute, which gave a maximum outer speed of ~1.5 m/s. The disc was insonified with diverging wavefronts transmitted by a phased-array transducer (see "Ultrasound sequences" subsection for details).

The spinning disc is an ideal Doppler phantom whose ground-truth Doppler velocities can be easily determined. To obtain more realistic Doppler data, we completed the *in vitro* analysis with a free water jet flow generated by a sharp-edged circular orifice plate (inner diameter of ~13 mm). A low-concentration cornstarch suspension mimicked the backscattering effect of red blood cells. The set-up included a controllable centrifugal pump and an electromagnetic flowmeter. The flow rate was varied from 1.6 to 2.5 liters per minute (maximum speed of 0.52 m/s). The phased-array transducer was positioned parallel to the jet and the flow was directed towards the transducer.

The maximum velocity amplitudes obtained in our *in vitro* experiments for the spinning disc and free jet flow were 1.5 and 0.5 m/s, respectively. We deliberately chose these upper limits due to the technical restrictions of the two experimental set-ups. To create significant aliasing, we thus reduced the principal PRF of the ultrasound sequences (see "Ultrasound sequences" subsection for details).

5.2.4 *In vivo* validation – ventricular filling & carotid artery

To test the *in vivo* feasibility of staggered multiple-PRF ultrafast color Doppler, we scanned the left heart of a 31-year-old healthy volunteer with a 2.5-MHz phased-array transducer (ATL P4-2). To obtain a 3-chamber view, we carried out ultrafast acquisitions along the long-axis view from the apical position. We also scanned the common carotid artery of a

34-year-old healthy volunteer using a 5-MHz linear-array transducer (ATL L7-4). The transmit beamforming protocol for the carotid was similar to the one used in the *in vitro* experiments and the *in vivo* cardiac application, except that plane wavefronts were emitted instead of circular beams [8]. The ultrasound sequences are described in the next paragraph. The volunteers signed an informed consent form approved by the local ethics committee. Given that the heart and carotid artery of the two volunteers were healthy (no cardiac anomalies and no carotid stenosis), the reference PRF_1 was intentionally set to a relatively low value to induce substantial aliasing in the single-PRF Doppler images.

5.2.5 Ultrasound sequences – dual- and triple-PRF emissions

We used a Verasonics research scanner (V-1-64, Verasonics Inc., Redmond, WA) to carry out the *in vitro* and *in vivo* experiments. Two different transducers were employed depending on the application. For the *in vitro* set-ups and the cardiac examination, a 2.5-MHz phased-array transducer (ATL P4-2, 64 elements, pitch = 0.32 mm) was used to transmit diverging circular wavefronts using a full aperture. Diverging wavefronts were transmitted by a virtual source located behind the ultrasound transducer [9]. The location of this source was defined by the angular width and tilt of the ROI as well as the aperture of the transducer (see fig. 5.2). The angular widths were 90^o and 30^o for the LV and the *in vitro* flow jet, respectively. For the *in vivo* vascular examination a 5-MHz linear-array transducer (ATL L7-4, 128 elements, pitch = 0.298 mm) was used to transmit plane wavefronts.

To perform Duplex scanning, eleven tilted transmits were emitted using short ultrasound pulses (1 wavelength) to create B-mode images; subsequently, an ensemble of long ultrasound pulses (6 wavelengths) was emitted at two or three staggered PRF (see fig. 5.1) to provide color Doppler estimates. No compounding was performed for the Doppler modes (tilting angle fixed at zero). The reference PRFs (PRF_1, Eq. 5.7) were intentionally set below the maximum possible PRF (Eq. 5.5) to generate significant single or double folding (aliasing) in the color Doppler fields.

The *in vitro* rotating disc was imaged using a staggered triple-PRF pulsing sequence with $PRF_1 = 2666$ Hz, $PRF_2 = ⅔\ PRF_1 = 1777$ Hz, and $PRF_3 = ¾\ PRF_1 = 2000$ Hz (Fig. 5.1, 3rd sequence). The corresponding extended Nyquist velocity (Eq. 5.9) was $6\ V_{N_1} = 6\times0.4 = 2.4$ m/s. The free jet flow was insonified using a dual-PRF scheme with $PRF_1 = 2000$ Hz and $PRF_2 = ⅔\ PRF_1 = 1333$ Hz (Fig. 5.1, 2nd sequence) whose extended Nyquist velocity was $2\ V_{N_1} = 2\times0.3 = 0.6$ m/s. When conducting the *in vivo* experiments, the left heart was insonified with a staggered dual-PRF scheme with $PRF_1 = 1500$ Hz and $PRF_2 = ⅔\ PRF_1 = 1000$ Hz (Fig. 5.1, 2nd sequence), which gave an extended Nyquist velocity of $2\ V_{N_1} = 2\times0.25 = 0.50$ m/s. The carotid artery was imaged using a staggered dual-PRF scheme with $PRF_1 = 1$ kHz and $PRF_2 = ⅔\ PRF_1 = 666$ Hz which gave an extended Nyquist velocity of $2\ V_{N_1} = 2\times0.23 = 0.46$ m/s.

The RF data were sampled at 10 MHz and dynamically focused in reception by using a diffraction summation (delay-and-sum) technique programmed on GPU. No apodization was used either in transmission or reception. The beamformed RF signals were then time-gain compensated and IQ-demodulated. We beamformed and post-processed the RF data offline.

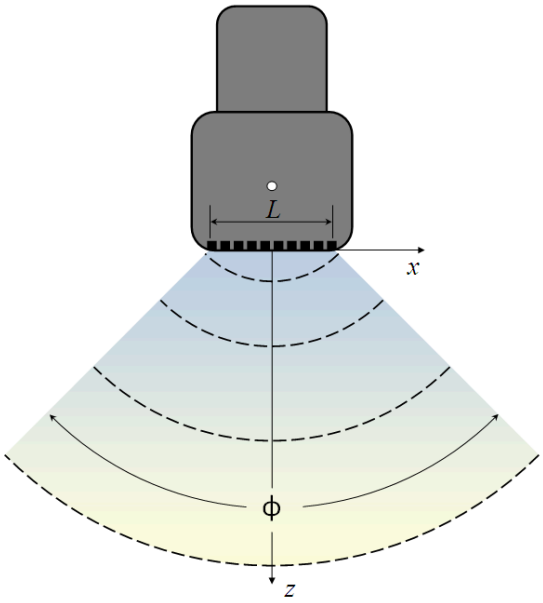

Fig. 5.2 – *Diverging circular wave transmit.* The virtual source (white dot) is located behind the ultrasound phased-array transducer. Transmit delay laws applied to the piezoelectric elements are defined by the angular width ϕ of the region-of-interest (shaded zone) and the transducer aperture *L*.

5.2.6 Doppler velocity estimation

The Doppler velocities were estimated from the IQ (in-phase/quadrature) signals after clutter filtering. Clutter filtering was necessary *in vivo* only. Clutter mostly refers to strong tissue echoes that might interfere with blood Doppler signals. Polynomial regression and FIR or IIR (finite/infinite response) filters are the most common (and simplest) clutter rejection filters [33]. The FIR and IIR linear filters, in their basic forms, require the signals to be uniformly sampled, and are not adapted for our multiple-PRF schemes. Other filters based on conversion into principal components (eigenfilters) also work with regularly-spaced signals only [34]. To eliminate the clutter, we high-pass filtered the IQ signals using orthogonal polynomial regressions, which can easily deal with irregularly sampled signals. Instead of using a fixed polynomial order [35], and to make the polynomial regression filter adaptive, we selected different orders for each single slow-time ensemble: we chose the polynomial orders, in the interval [1,10], which minimized the small-sample version of the Akaike's information criterion [36], given by

$$\mathrm{AIC_c} = n\left\{\ln\left(\frac{\mathrm{RSS}}{n}\right) + \frac{n+m+1}{n-m-3}\right\}. \qquad (5.20)$$

In Eq. (5.20), n corresponds to the sample length (ensemble length), m is the degree of the fitting polynomial being assessed, and RSS is the sum of squares of the residuals between the original data and the polynomial model. We give further details in the discussion.

Two (dual-PRF) or three (triple-PRF) Doppler fields (V_{D_1}, V_{D_2} and V_{D_3}) were then estimated from the filtered beamformed IQ signals using the 2D auto-correlator proposed by Loupas *et al*. [37]. We calculated each Doppler field independently using the pulse pairs corresponding to the respective pulse repetition periods PRP_1, PRP_2 and PRP_3 (see fig. 5.1). In the *in vitro* experiments the staggered slow-time sequences were composed of a packet of 39 (dual-PRF) or 58 (triple-PRF) receive pulses, which corresponded to 19 pulse pairs for each individual PRF. In the *in vivo* experiments the staggered slow-time sequences were reduced to 29 (dual-PRF) transmitted pulses, which corresponded to 14 pulse pairs for each individual PRF. This choice guaranteed an adequate frame rate given that the reference PRF was intentionally decreased. We then deduced the left hand side terms of Eq. (5.14) and determined the related Nyquist numbers (n_{N_i}) using a look-up table (see Table 5.1 and Table 5.2 in the appendix). The unambiguous Doppler field was finally deduced from equation (5.16). Some few remaining errors were removed by basic median filtering. The power Doppler fields were also determined *in vivo* from the complete slow-time sequences. Power Doppler was used to define the regions of interest of the color Doppler images.

5.3 Results

5.3.1 In vitro spinning disc

Although large aliased areas were present in the single-PRF Doppler fields (see fig. 5.3, right column), the triple-PRF approach allowed full disambiguation of the Doppler velocities (see fig. 5.3, bottom left). For each rotational speed, we compared the Doppler velocity at location of peak radial velocity (white cross on fig. 5.3) with the ground-truth maximum speed given by ωR, where ω and R stand for the angular velocity and the radius of the disc.

With a single PRF (PRF_1 = 2666 Hz), as expected from Eq. (5.1), a first aliasing occurred at ~0.4 m/s, and a second at ~(0.4 + 2×0.4) = 1.2 m/s (see fig. 5.4, diamonds). A dual-PRF approach (with PRF_1 = 2666 Hz, and PRF_2 = ⅔ PRF_1 = 1777 Hz) extended the unambiguous velocity to twice the original velocity range (see fig. 5.4, empty dots), as predicted by Eq. (5.9). Because the extended Nyquist velocity was 2.4 m/s (see "*Ultrasound sequences*"), no aliasing occurred with the triple-PRF approach within the velocity range of the experiments (Fig. 5.4, full dots). The absolute global error in the whole Doppler velocity field, as given by the RMSE (root-mean-square error), increased linearly with the rotational speed (Fig. 5.5, diamonds) but remained small (< 0.04 m/s) in comparison with the maximum velocities. The RMSE normalized to the mean of the observed values (NRMSE) decreased exponentially and was smaller than 8% (Fig. 5.5, dots).

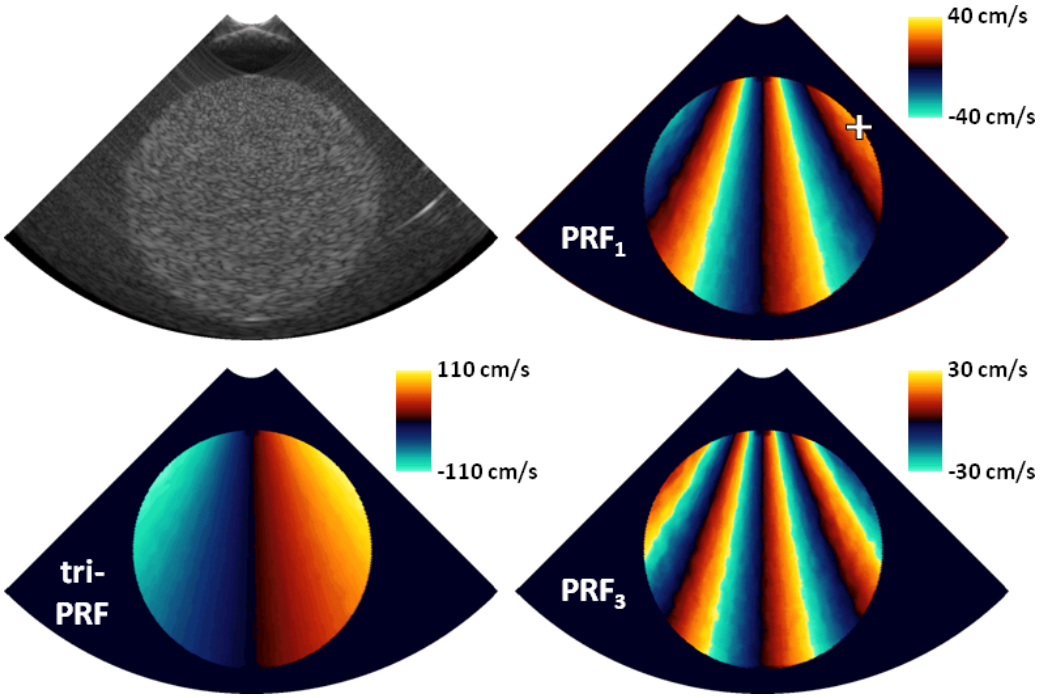

Fig. 5.3 – *Triple-PRF ultrafast Doppler in the spinning disc. Top-left*: B-mode image obtained using diverging circular beams with a six-cycle pulse. *Right column*: masked color Doppler images corresponding to the pulse pairs emitted at PRF_1 (2666 Hz) and PRF_3 (2000 Hz), respectively. *Bottom-left*: disambiguated color Doppler image using the triple-PRF approach.

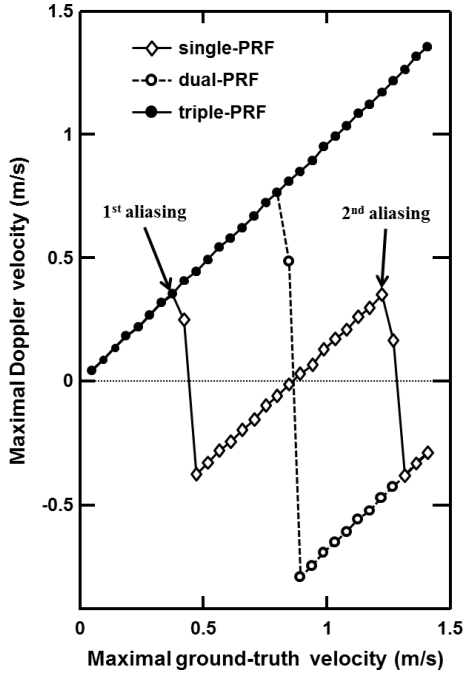

Fig. 5.4 – *Ultrafast Doppler in the spinning disc: maximal velocities; Doppler vs. ground-truth***.** The "maximal" Doppler velocity is the Doppler velocity at location of peak radial velocity (white cross on fig. 5.3). The diamonds represent the Doppler velocities measured in the spinning disc with a conventional single-PRF approach (at PRF_1 = 2666 Hz). Aliasing occurred above 0.4 and 1.2 m/s (see also fig. 5.3, top-right image). The empty dots depict the dual staggered PRF scheme (2^{nd} sequence in fig. 5.1), where the second PRF_2 was ⅔ PRF_1 = 1777 Hz. Aliasing occurred above 0.8 m/s. The full dots illustrate the Doppler velocities with the triple-PRF approach. No aliasing was present.

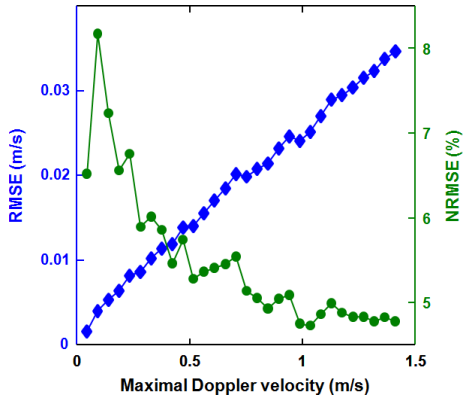

Fig. 5.5 – *Ultrafast Doppler in the spinning disc: total errors.* Global root-mean-square error (RMSE, diamonds) and normalized RMSE (NRMSE, solid circles) returned by the triple-PRF approach (see fig. 5.3, bottom-left).

5.3.2 In vitro flow jet

The dual-PRF approach allowed full disambiguation of the Doppler velocities in the free flow jet (Fig. 5.6). For a free jet generated by a sharp-edged thin orifice plate, the velocity at the vena contracta (i.e. the maximum jet velocity) is approximately given by:

$$V_{\max} = \frac{Q}{0.6\,A}, \tag{5.21}$$

where Q is the flow rate and A represents the aperture area [38]. We compared this theoretical velocity (ideal velocity) against the maximum Doppler velocity issued from the dual-PRF ultrasound sequence (Fig. 5.7). A high precision was obtained (coefficient of determination $r^2 = 0.97$). However, likely due to experimental uncertainties (plate thickness, probe alignment, inaccuracy in orifice area and flow, observational errors, smoothing...), we observed some inaccuracy. Indeed, a linear regression did not return the identity line: we had $y = 0.43\,x + 0.27$ instead.

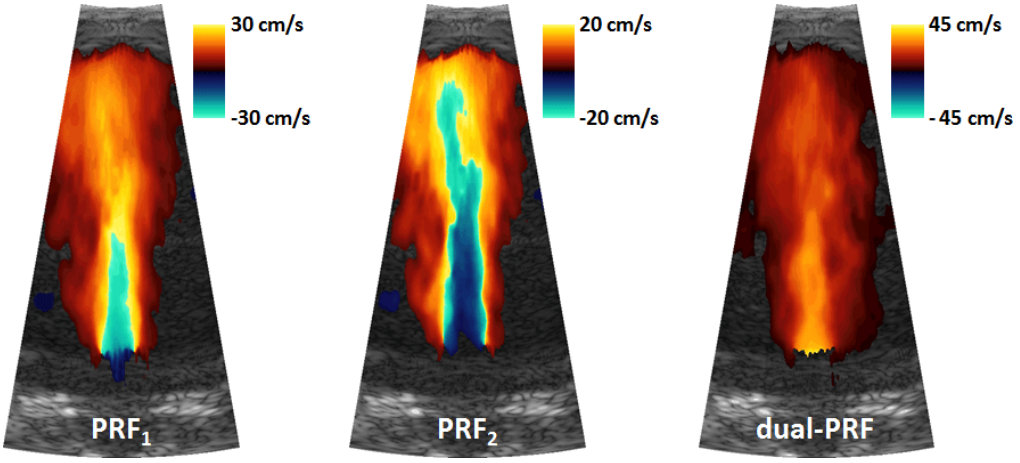

Fig. 5.6 – *Dual-PRF ultrafast Doppler in the free flow jet. Left and Middle*: color Doppler images corresponding to the pulse pairs emitted at PRF_1 (2000 Hz) and PRF_2 (1333 Hz), respectively. *Right*: disambiguated color Doppler image using the dual-PRF approach.

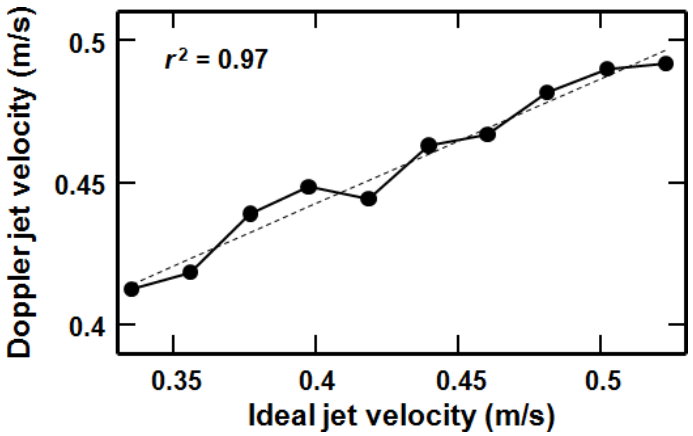

Fig. 5.7 – *Jet velocity: Doppler vs. ideal.* A determination coefficient of $r^2 = 0.97$ was observed between the maximum Doppler velocity and the ideal jet velocity estimated from Eq. (5.21).

5.3.3 *In vivo* left ventricle filling and common carotid artery blood flow

The dual-PRF approach was also effective *in vivo*, both in the left heart during early filling (Fig. 5.8) and the common carotid artery (Fig. 5.9). Since we decreased the maximum PRF (i.e. PRF_1) intentionally (see subsection 5.2.4 "*In vivo validation*"), significant aliasing was present in the single-PRF Doppler images. As expected, aliasing was more pronounced with PRF_2 because PRF_2 was smaller than PRF_1. Although aliasing was present in the single-PRF Doppler fields (Fig. 5.8 and 5.9), the dual-PRF approach doubled the Nyquist velocity and allowed full disambiguation of the Doppler velocities. These results show that the staggered multiple-PRF approach is well adapted to ultrafast color Doppler, both with planar and circular ultrasound beams.

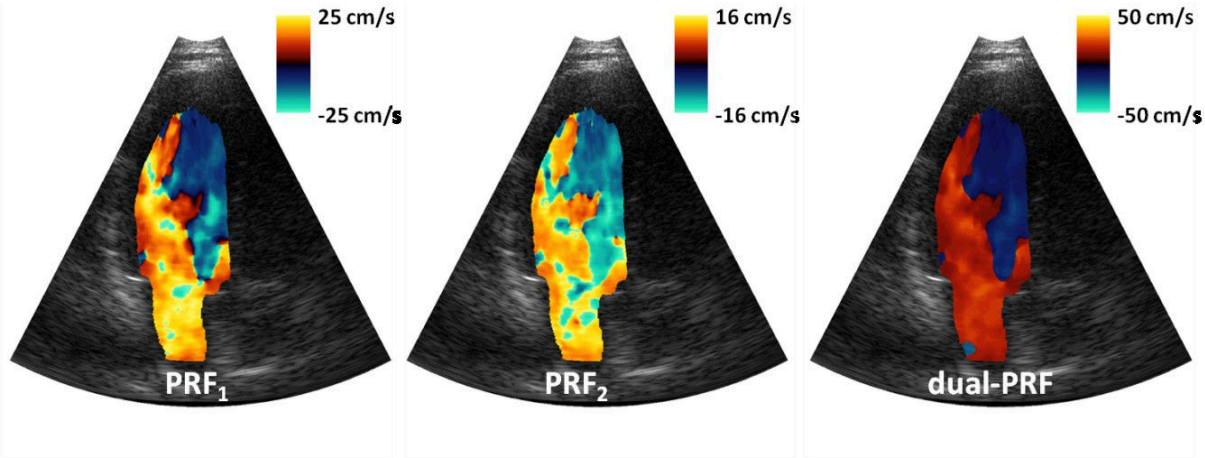

Fig. 5.8 – *Color flow maps of the LV filling (tree chamber view) with the staggered multi-PRF ultrafast technique. Left*: Aliased color Doppler map obtained with a single-PRF transmission scheme, with $PRF_1 = 1.5$ kHz. *Middle*: idem, with $PRF_2 = 1$ kHz. *Right*: De-aliased color Doppler map obtained with a staggered dual-PRF transmission scheme ($PRF_1 = 1.5$, $PRF_2 = 1$ kHz).

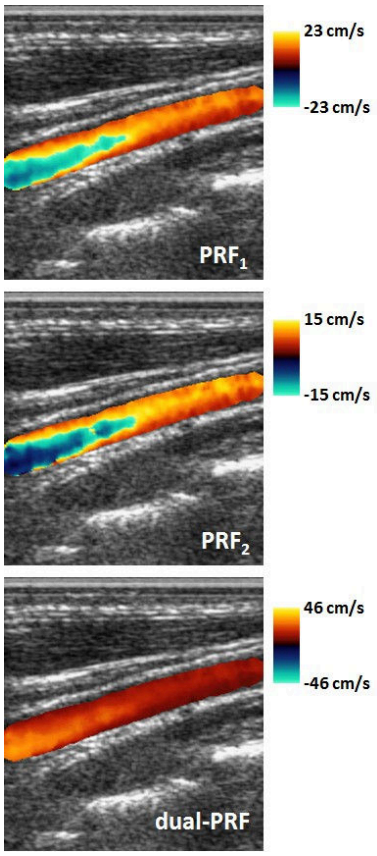

Fig. 5.9 – *Color flow maps of the common carotid artery with the staggered dual-PRF ultrafast technique with plane waves. Top*: Single-PRF aliased color Doppler map, with PRF_1 = 1000 Hz. *Center*: idem, with PRF_2 = 666 Hz. *Bottom*: De-aliased color Doppler estimate obtained using staggered dual-PRF (1000 and 666 Hz) and plane waves.

5.4 Discussion

An advantage of ultrafast over conventional color Doppler is obviously the large number of available frames. This quality allowed us to implement an effective technique for getting unambiguous color Doppler. Our *in vitro* and *in vivo* investigations showed that ultrafast color Doppler can indeed be conveniently adapted to dual- or triple-PRF schemes. The Doppler Nyquist velocity can be thus extended to ranges that will be free from aliasing in the clinical setting. Of important note, the implementation of the staggered multiple-PRF approach would have been limited with conventional ultrasound imaging because of the longer ensemble size required to obtain several velocity estimates. This would have further reduced the relatively low frame rate given by conventional color Doppler. The availability of a larger number of frames also allows the use of larger slow-time ensembles for better Doppler velocity estimates. As a consequence, the optimal degrees of the fitting polynomials for clutter reduction must be higher than the orders conventionally used (2 or 3). In this section, after mentioning some limitations, we briefly discuss how multiple-PRF schemes affect the effective frame rate and why it is needed to adapt the orders of the fitting polynomials for clutter reduction.

5.4.1 Limitations

We showed that staggered multiple-PRF schemes in ultrafast color Doppler return non-aliased Doppler images, as long as blood speed does not exceed the extended Nyquist velocity (Eq. 5.9). Using the ⅔−¾ triple-PRF scheme tested in the spinning disc, it was possible to sextuple the original Nyquist given by Eq. 5.6. In all our configurations, we removed aliasing successfully, both *in vivo* and *in vitro*. To work correctly, however, the flow must be quasi-stationary during the time required to register one multiple-PRF slow-time ensemble. This situation is not encountered in highly spatially and/or temporally fluctuating flows such as in valvular regurgitation or stenosis. Regurgitant jets are turbulent jets which can contain high-velocity and high-acceleration components [39]. This may result in rapidly varying aliased Doppler velocities, in which case, the multiple-PRF staggered method would be defective. Further *in vitro* analyses would be necessary to determine the practical limits of this technique.

5.4.2 Frame rate reduction due to of the staggered multi-PRF transmission scheme

Although the Nyquist velocity can be extended by using staggered multiple-PRF schemes, adding one or two additional smaller-PRF sequences unavoidably reduces the effective frame rate of ultrafast color Doppler. The frame rate reduction due to the multiple-PRF approach may become significant and should be taken into account, especially when scanning deep regions. The frame rate reduction mainly depends upon: 1) the number of compounded transmits to generate a high-quality B-mode frame for duplex imaging, and 2) the ensemble length of the multiple-PRF sequence. Let N_{D} represent the number of image pairs to obtain each Doppler field. The ensemble length is thus $(2N_{\mathrm{D}}+1)$ or $(3N_{\mathrm{D}}+1)$ for a dual- or triple-PRF scheme, respectively. Let N_{B} denote the number of transmissions to generate one compounded grayscale image. The time required to produce one duplex image is thus

$$T_{\mathrm{duplex}}\,(n_{\mathrm{PRF}}) = \left(N_{\mathrm{B}} + N_{\mathrm{D}} \sum_{i=1}^{n_{\mathrm{PRF}}} \frac{q_i}{p_i}\right) \mathrm{PRP}_1, \tag{5.22}$$

with n_{PRF} equals 1, 2 or 3, for single-, dual- or triple-PRF emission, respectively. We now consider a staggered dual- or triple-PRF transmission scheme with: 1) PRF_2 = ⅔ PRF_1 and/or PRF_3 = ¾ PRF_1, 2) an ensemble length fixed to $N_{\mathrm{D}} = 19$ pulses for each single-PRF (see "Methods" section 5.2.3 and 5.2.4) $N_{\mathrm{B}} = 11$ (according to [14]). These dual- and triple-PRF transmission sequences lead to 1.9- and 2.8-fold decreases in frame rate in comparison to the single-PRF color Doppler scheme. In color Doppler echocardiography, with PRF_1 ~ 5000 Hz, this would lead to respective duplex frame rates of about 85 (dual-) and 60 fps (triple-) instead of 165 fps (single-PRF).

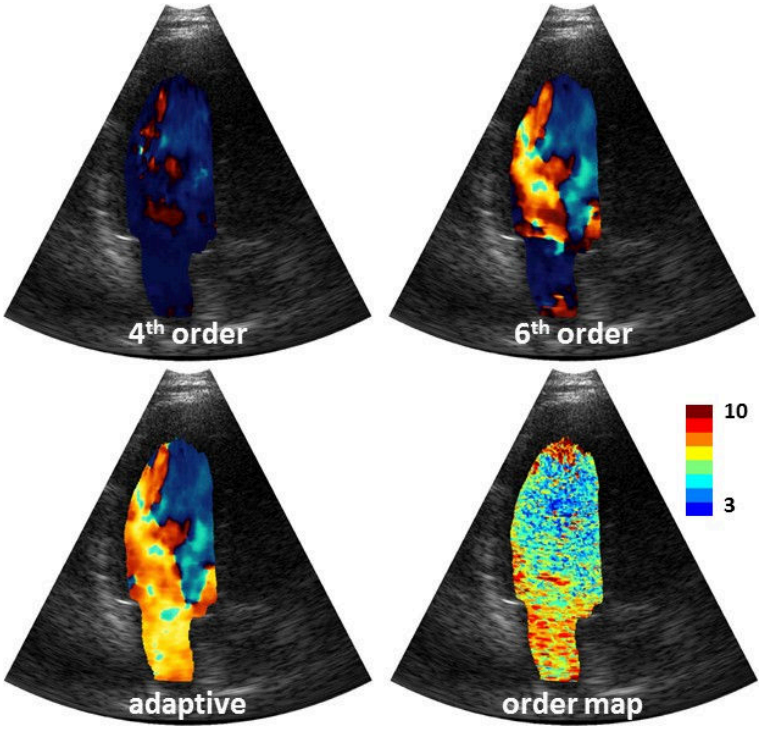

Fig. 5.10 – *Effect of clutter filter in staggered dual-PRF ultrafast cardiac data. Top-left*: Color Doppler estimates obtained after filtering the IQ Doppler ensemble with a 4th order polynomial regression clutter filter. The clutter is not totally removed. *Top-right*: idem but with a 6th order polynomial regression clutter filter. Some clutter is still present in the left atrium. *Bottom-left*: idem but with a spatially adaptive polynomial regression filter (polynomial orders selected according to the AIC minimization criterion). The Doppler map is visually consistent in the whole heart. *Bottom-right*: Corresponding map of the "optimal" polynomial orders according to the AIC minimization criterion.

5.4.3 Adaptive regression clutter filtering

Clutter canceling for staggered PRF waveforms has also been the subject of several studies in meteorology [40-42], including the regression filter [43]. As mentioned in the subsection "*Doppler velocity estimation*", we chose the orthogonal polynomial regression filter, among many existing clutter filters [34;44;45], for its ease-of-use and its versatility to non-uniform slow-time sampling. Polynomial regression filters assume that the clutter echoes can be approximated by a polynomial of a given order, which is determined in a least-squares sense. The polynomial clutter component is subtracted from the original Doppler signal to retrieve the blood flow contribution. Polynomials of first- up to fourth-order were proposed in the literature [44]. For a given packet length, the polynomial order controls the transition band and the cut-off frequency [33]. A fixed polynomial order thus results in a homogeneous clutter filtering. Fixing the polynomial order, however, may be suboptimal since the clutter-to-blood spectral separation varies spatially. In this study, for each single slow-time ensemble, we thus selected the polynomial model which minimized the Akaike information criterion (AIC) [46]. The AIC trades off the goodness-of-fit against the complexity (i.e. the number of parameters) of the model and is well adapted to parametric regression [36]. The model with the lowest AIC is considered the best possible choice among all models specified. Because the packet length was relatively small (i.e. (packet

size)/(polynomial order + 2) < 40) in our study, we used the small-sample version of the AIC (see Eq. 5.20), as recommended in [36].

To further illustrate the efficacy of the AIC in regression clutter filtering, we analysed the *in vivo* cardiac Doppler data obtained from the first series (PRF_1, see Fig. 5.8, leftmost panel) of the staggered dual-PRF transmission scheme. The total ensemble of 39 staggered samples was first filtered with a 4^{th}-order polynomial (Fig. 5.10, top left). In the resulting image, blood flow could not be identified. With a 6^{th}-order polynomial regression filter, the color Doppler image exhibited a typical intraventricular diastolic blood flow pattern (Fig. 5.10, top right). The atrial blood flow, however, still remained spurious. Finally, when using spatially-adapted polynomial orders (lying between 1 and 10) which minimized the AIC criterion, both the intraventricular and intra-atrial Doppler fields were coherent (Fig. 5.10, bottom left). The map of the polynomial orders determined by the AIC criterion (Fig. 5.10, bottom right) show that the largest orders were correspondingly located in the left atrium. It is likely that strong atrial clutter resulted from the movements of the mitral valve leaflets.

Our *in vivo* results tend to show that the polynomial regression clutter filter was very well adapted to the dual- and triple-PRF schemes. When coupled with the AIC minimization criterion, it presented an obvious benefit. We showed that Doppler velocities could be estimated even in cases where clutter-to-signal ratios were high. Further studies, however, are required to investigate the velocity bias introduced by polynomial regression clutter filtering with such staggered sequences. Indeed, non-stationary clutter might become significant due to non-uniform slow-time sampling. A possible *in vivo* validation could be provided by comparing the Doppler velocities derived from the proposed method with those obtained from aliasing-free techniques based on speckle tracking [47].

5.5 Conclusion

The staggered multiple-PRF emission scheme for ultrafast color Doppler successfully extended the Nyquist limit *in vitro* and *in vivo*. Clutter filtering by spatially-adaptive polynomial regression was ideally suited to the non-uniform slow-time sampling. Staggered multiple-PRF ultrafast color Doppler could be the method of choice for developing quantitative clinical tools based on color Doppler imaging.

5.6 Acknowledgments

The authors thank Dr. François Destrempes for his careful reading and mathematical suggestions. This work was supported by an operating grant from the Canadian Institutes of Health Research (CIHR, MOP-106465, Dr. Garcia). Dr. Garcia holds a research scholarship award from the Fonds de Recherche en Santé du Québec (FRSQ). Daniel Posada received an IEEE student travel grant to attend the 2013 IEEE International Ultrasonics Symposium.

5.7 Appendix

Table 5.2 – Lookup table for the Nyquist numbers. This table illustrates how equation (5.14) is used to determine the Nyquist numbers. It represents a triple-PRF scheme with $p_2 = 2$, $q_2 = 3$ and $p_3 = 3$, $q_3 = 4$. The expressions of the two first columns (Eq. 5.14) are calculated, for each pixel, from the Doppler velocities V_{D_i}. Each pair is associated with a unique combination of Nyquist numbers $(n_{\mathrm{N}_1}, n_{\mathrm{N}_2}, n_{\mathrm{N}_3})$.

$\mathrm{nint}\left(q_2 \frac{V_{\mathrm{D}_2} - V_{\mathrm{D}_1}}{2V_{\mathrm{N}_1}}\right)$	$\mathrm{nint}\left(q_3 \frac{V_{\mathrm{D}_3} - V_{\mathrm{D}_1}}{2V_{\mathrm{N}_1}}\right)$	n_{N_1}	n_{N_2}	n_{N_3}
-2	-3	0	1	1
-2	-2	-2	-2	-2
-2	-1	2	4	3
-2	0	0	1	0
-2	1	-2	-2	-3
-2	2	2	4	2
-2	3	0	1	-1
-1	-3	-3	-4	-3
-1	-2	1	2	2
-1	-1	-1	-1	-1
-1	0	-3	-4	-4
-1	1	1	2	1
-1	2	-1	-1	-2
0	-3	0	0	1
0	-2	-2	-3	-2
0	-1	2	3	3
0	0	0	0	0
0	1	-2	-3	-3
0	2	2	3	2
0	3	0	0	-1
1	-2	1	1	2
1	-1	-1	-2	-1
1	0	3	4	4
1	1	1	1	1
1	2	-1	-2	-2
1	3	3	4	3
2	-3	0	-1	1
2	-2	-2	-4	-2
2	-1	2	2	3
2	0	0	-1	0
2	1	-2	-4	-3
2	2	2	2	2
2	3	0	-1	-1

5.7.1 Demonstrations of expressions (5.4), (5.12) and (5.15)

We first aim at demonstrating expression (5.4) of the Nyquist number. Due to aliasing, Doppler velocities can have no absolute values above the Nyquist velocity, so that:

$$V_{\mathrm{D}} = (V_{\mathrm{D}}^{u} + V_{\mathrm{N}})\big(\mathrm{mod}(2V_{\mathrm{N}})\big) - V_{\mathrm{N}}, \tag{A.1}$$

By definition of the congruence function, $m \bmod(n) = m - n\,\mathrm{floor}(m/n)$. Thus (A.1) becomes

$$V_{\mathrm{D}} = (V_{\mathrm{D}}^{u} + V_{\mathrm{N}}) - 2V_{\mathrm{N}}\,\mathrm{floor}\left(\frac{V_{\mathrm{D}}^{u}+V_{\mathrm{N}}}{2V_{\mathrm{N}}}\right) - V_{\mathrm{N}}, \tag{A.2}$$

which can be rewritten as

$$V_{\mathrm{D}} = V_{\mathrm{D}}^{u} - 2\mathrm{floor}\left(\frac{V_{\mathrm{D}}^{u}+V_{\mathrm{N}}}{2V_{\mathrm{N}}}\right) V_{\mathrm{N}}. \tag{A.3}$$

We now aim at demonstrating expression (5.12). Inequality (5.11) gives:

$$-k\,V_{\mathrm{N}_1} < V_{\mathrm{D}}^{u} < k\,V_{\mathrm{N}_1}. \tag{A.4}$$

Adding V_{N_i} then dividing by $(2V_{\mathrm{N}_i})$ results in

$$-\frac{k\,V_{\mathrm{N}1}}{2\,V_{\mathrm{N}_i}} + \frac{1}{2} < \frac{V_{\mathrm{D}}^{u}+V_{\mathrm{N}_i}}{2V_{\mathrm{N}_i}} < \frac{k\,V_{\mathrm{N}1}}{2\,V_{\mathrm{N}_i}} + \frac{1}{2}, \tag{A.5}$$

which, from (5.8), can be rewritten as

$$-\frac{k\,q_i}{2\,p_i} + \frac{1}{2} < \frac{V_{\mathrm{D}}^{u}+V_{\mathrm{N}_i}}{2V_{\mathrm{N}_i}} < \frac{k\,q_i}{2\,p_i} + \frac{1}{2}. \tag{A.6}$$

It can be verified that $a \le x < b \Longrightarrow \mathrm{floor}(a) \le \mathrm{floor}(x) \le \mathrm{ceiling}(b-1)$. Therefore (A.6) gives

$$\text{floor}\left(-\frac{k\,q_i}{2\,p_i}+\frac{1}{2}\right) \leq \text{floor}\left(\frac{V_{\text{D}}^{u}+V_{\text{N}_i}}{2V_{\text{N}_i}}\right) \leq \text{ceiling}\left(\frac{k\,q_i}{2\,p_i}-\frac{1}{2}\right). \tag{A.7}$$

Since $\forall x, -\text{floor}(-x) = \text{ceiling}(x)$, (A.4) becomes

$$\left|\text{floor}\left(\frac{V_{\text{D}}^{u}+V_{\text{N}_i}}{2V_{\text{N}_i}}\right)\right| \leq \text{ceiling}\left(\frac{k\,q_i}{2\,p_i}-\frac{1}{2}\right). \tag{A.8}$$

From the definition of the Nyquist number (5.4), (A.8) leads to inequality (5.12)

$$\left|n_{\text{N}_i}\right| \leq \text{ceiling}\left(\frac{k\,q_i}{2\,p_i}-\frac{1}{2}\right). \tag{A.9}$$

We finally aim at demonstrating the strict inequality (5.15). We have, by definition of the Nyquist velocity

$$\forall i, \left|V_{\text{D}_i}\right| \leq V_{\text{N}_i}. \tag{A.10}$$

The triangle inequality leads to

$$\left|V_{\text{D}_i} - V_{\text{D}_1}\right| \leq V_{\text{N}_i} + V_{\text{N}_1}, \tag{A.11}$$

which can be rewritten, after division by $2\,V_{\text{N}_1}$, as

$$\left|\frac{V_{\text{D}_i}-V_{\text{D}_1}}{2\,V_{\text{N}_1}}\right| \leq \frac{V_{\text{N}_i}}{2\,V_{\text{N}_1}}+\frac{1}{2}. \tag{A.12}$$

Using equalities (5.8) and (5.13), because $q_i > 0$, we obtain the constraint (5.15)

$$\left|n_{\text{N}_1}q_i - n_{\text{N}_i}p_i\right| \leq \frac{1}{2}(p_i + q_i). \tag{A.13}$$

Bibliography

[1] T. Uejima, A. Koike, H. Sawada, T. Aizawa, S. Ohtsuki, M. Tanaka, T. Furukawa, and A. G. Fraser, "A new echocardiographic method for identifying vortex flow in the left ventricle: numerical validation," Ultrasound Med. Biol., vol. 36, no. 5, pp. 772-788, May2010.

[2] D. Garcia, J. C. del Álamo, D. Tanné, R. Yotti, C. Cortina, E. Bertrand, J. C. Antoranz, R. Rieu, M. A. Garcia-Fernandez, F. Fernandez-Aviles, and J. Bermejo, "Two-dimensional intraventricular flow mapping by digital processing conventional color-Doppler echocardiography images," IEEE Trans. Med. Imaging, vol. 29, no. 10, pp. 1701-1713, 2010.

[3] F. Mehregan, F. Tournoux, S. Muth, P. Pibarot, R. Rieu, G. Cloutier, and D. Garcia, "Doppler vortography: a color Doppler approach to quantification of intraventricular blood flow vortices," Ultrasound Med. Biol., vol. 40, no. 1, pp. 210-221, Jan.2014.

[4] R. Ro, D. Halpern, D. J. Sahn, P. Homel, M. Arabadjian, C. Lopresto, and M. V. Sherrid, "Vector flow mapping in obstructive hypertrophic cardiomyopathy to assess the relationship of early systolic left ventricular flow and the mitral valve," Journal of the American College of Cardiology, vol. 64, no. 19, pp. 1984-1995, Nov.2014.

[5] J. Bermejo, Y. Benito, M. Alhama, R. Yotti, P. Martinez-Legazpi, C. P. del Villar, E. Perez-David, A. Gonzalez-Mansilla, C. Santa-Marta, A. Barrio, F. Fernandez-Aviles, and J. C. Del Alamo, "Intraventricular vortex properties in nonischemic dilated cardiomyopathy," Am. J. Physiol Heart Circ. Physiol, vol. 306, no. 5, p. H718-H729, Mar.2014.

[6] S. Muth, S. Dort, I. A. Sebag, M. J. Blais, and D. Garcia, "Unsupervised dealiasing and denoising of color-Doppler data," Med. Image Anal., vol. 15, no. 4, pp. 577-588, Aug.2011.

[7] A. A. Pellett, W. G. Tolar, D. G. Merwin, and E. K. Kerut, "Doppler aliasing," Echocardiography., vol. 22, no. 6, pp. 540-543, July2005.

[8] J. Bercoff, G. Montaldo, T. Loupas, D. Savery, F. Meziere, M. Fink, and M. Tanter, "Ultrafast compound Doppler imaging: providing full blood flow characterization," IEEE Trans. Ultrason. Ferroelectr. Freq. Control, vol. 58, no. 1, pp. 134-147, Jan.2011.

[9] B. F. Osmanski, D. Maresca, E. Messas, M. Tanter, and M. Pernot, "Transthoracic ultrafast Doppler imaging of human left ventricular hemodynamic function," Ultrasonics, Ferroelectrics, and Frequency Control, IEEE Transactions on, vol. 61, no. 8, pp. 1268-1275, 2014.

[10] J. Udesen, F. Gran, K. Hansen, J. A. Jensen, C. Thomsen, and M. B. Nielsen, "High frame-rate blood vector velocity imaging using plane waves: Simulations and preliminary experiments," IEEE Trans. Ultrason. Ferroelectr. Freq. Control, vol. 55, no. 8, pp. 1729-1743, Aug.2008.

[11] I. K. Ekroll, T. Dahl, H. Torp, and L. Lovstakken, "Combined vector velocity and spectral Doppler imaging for improved imaging of complex blood flow in the carotid arteries," Ultrasound Med. Biol., vol. 40, no. 7, pp. 1629-1640, July2014.

[12] B. Y. Yiu and A. C. Yu, "High-frame-rate ultrasound color-encoded speckle imaging of complex flow dynamics," Ultrasound Med. Biol., vol. 39, no. 6, pp. 1015-1025, June2013.

[13] S. Ricci, L. Bassi, and P. Tortoli, "Real-time vector velocity assessment through multigate doppler and plane waves," IEEE transactions on ultrasonics, ferroelectrics, and frequency control, vol. 61, no. 2, pp. 314-324, 2014.

[14] C. Papadacci, M. Pernot, M. Couade, M. Fink, and M. Tanter, "High-contrast ultrafast imaging of the heart," IEEE transactions on ultrasonics, ferroelectrics, and frequency control, vol. 61, no. 2, pp. 288-301, 2014.

[15] J. A. Jensen, S. I. Nikolov, K. L. Gammelmark, and M. H. Pedersen, "Synthetic aperture ultrasound imaging," Ultrasonics, vol. 44 Suppl 1, pp. e5-15, Dec.2006.

[16] B. F. Osmanski, M. Pernot, M. Fink, and M. Tanter, "*In vivo* transthoracic ultrafast Doppler imaging of left intraventricular blood flow pattern," Ultrasonics Symposium (IUS), 2013 IEEE International, pp. 1741-1744, July2013.

[17] J. Provost, C. Papadacci, J. E. Arango, M. Imbault, M. Fink, J. L. Gennisson, M. Tanter, and M. Pernot, "3D ultrafast ultrasound imaging *in vivo*," Phys. Med. Biol., vol. 59, no. 19, p. L1-L13, Oct.2014.

[18] J. E. Moller, E. Sondergaard, S. H. Poulsen, and K. Egstrup, "Pseudonormal and restrictive filling patterns predict left ventricular dilation and cardiac death after a first myocardial infarction: a serial color M-mode Doppler echocardiographic study," J. Am. Coll. Cardiol., vol. 36, no. 6, pp. 1841-1846, Nov.2000.

[19] P. Tortoli, F. Valgimigli, G. Guidi, and P. Pignoli, "Clinical evaluation of a new anti-aliasing technique for ultrasound pulsed Doppler analysis," Ultrasound Med. Biol., vol. 15, no. 8, pp. 749-756, 1989.

[20] V. L. Newhouse, P. LeCong, E. S. Furgason, and C. T. Ho, "On increasing the range of pulsed Doppler systems for blood flow measurement," Ultrasound Med. Biol., vol. 6, no. 3, pp. 233-237, 1980.

[21] R. J. Doviak, D. S. Zrnic, and D. S. Sirmans, "Doppler weather radar," Proc. IEEE, vol. 67, no. 11, pp. 1522-1553, 1979.

[22] R. J. Doviak and D. S. Zrnic, Doppler radar and weather observations Courier Dover Publications, 1993.

[23] H. Nishiyama and K. Katakura, "Non-equally-spaced pulse transmission for non-aliasing ultrasonic pulsed Doppler measurement," Journal of the Acoustical Society of Japan. E, vol. 13, no. 4, pp. 215-222, 1992.

[24] G. E. C. Nogueira, A. Ferreira, and J. T. Vidal, "A nonuniform sampled coherent pulsed Doppler ultrasonic velocimeter with increased velocity range," Ultrasonics, Ferroelectrics and Frequency Control, IEEE Transactions on, vol. 46, no. 2, pp. 452-456, 1999.

[25] D. S. Zrnic and P. Mahapatra, "Two methods of ambiguity resolution in pulse Doppler weather radars," IEEE Trans. Aerosp. Electron. Syst., no. 4, pp. 470-483, 1985.

[26] H. J. Nitzpon, J. C. Rajaonah, C. B. Burckhardt, B. Dousse, and J. J. Meister, "A new pulsed wave Doppler ultrasound system to measure blood velocities beyond the Nyquist limit," Ultrasonics, Ferroelectrics and Frequency Control, IEEE Transactions on, vol. 42, no. 2, pp. 265-279, 1995.

[27] Z. Zhang, A. Jakobsson, S. Nikolov, and J. A. Chambers, "Extending the unambiguous velocity range using multiple carrier frequencies," Electronics Letters, vol. 41, no. 22, pp. 1206-1208, 2005.

[28] D. Sirmans, D. Zrnic, and B. Bumgarner, "Extension of maximum unambiguous Doppler velocity by use of two sampling rates," 17th Conf. on Radar Meteorology, Seattle, WA, Amer. Meteor. Soc, pp. 23-28, 1976.

[29] S. L. Durden and C. L. Werner, "Application of an interferometric phase unwrapping technique to dealiasing of weather radar velocity fields," Journal of Atmospheric and Oceanic Technology, vol. 13, no. 5, pp. 1107-1109, Oct.1996.

[30] P. Tabary, F. Guibert, L. Perier, and J. Parent-du-Chatelet, "An operational triple-PRT Doppler scheme for the French radar network," Journal of Atmospheric and Oceanic Technology, vol. 23, no. 12, pp. 1645-1656, 2006.

[31] J. A. Jensen, "Color flow mapping using phase shift estimation," in Estimation of blood velocities using ultrasound Cambridge University Press, 1996, pp. 195-226.

[32] O. D. Kripfgans, J. M. Rubin, A. L. Hall, and J. B. Fowlkes, "Vector Doppler imaging of a spinning disc ultrasound Doppler phantom," Ultrasound Med. Biol., vol. 32, no. 7, pp. 1037-1046, July2006.

[33] H. Torp, "Clutter rejection filters in color flow imaging: A theoretical approach," Ultrasonics, Ferroelectrics and Frequency Control, IEEE Transactions on, vol. 44, no. 2, pp. 417-424, 1997.

[34] A. Yu and L. Lovstakken, "Eigen-based clutter filter design for ultrasound color flow imaging: a review," IEEE Trans. Ultrason. Ferroelectr. Freq. Control, vol. 57, no. 5, pp. 1096-1111, May2010.

[35] A. P. Kadi and T. Loupas, "On the performance of regression and step-initialized IIR clutter filters for color Doppler systems in diagnostic medical ultrasound," Ultrasonics, Ferroelectrics and Frequency Control, IEEE Transactions on, vol. 42, no. 5, pp. 927-937, 1995.

[36] C. M. Hurvich and C. L. Tsai, "Regression and time series model selection in small samples," Biometrika, vol. 76, no. 2, pp. 297-307, June1989.

[37] T. Loupas, J. T. Powers, and R. W. Gill, "An axial velocity estimator for ultrasound blood flow imaging, based on a full evaluation of the Doppler equation by means of a two-dimensional autocorrelation approach," Ultrasonics, Ferroelectrics and Frequency Control, IEEE Transactions on, vol. 42, no. 4, pp. 672-688, 1995.

[38] D. Garcia, P. Pibarot, C. Landry, A. Allard, B. Chayer, J. G. Dumesnil, and L. G. Durand, "Estimation of aortic valve effective orifice area by Doppler echocardiography: effects of valve inflow shape and flow rate," J. Am. Soc. Echocardiogr., vol. 17, no. 7, pp. 756-765, July2004.

[39] T. Masuyama, K. Kodama, A. Kitabatake, S. Nanto, H. Sato, M. Uematsu, M. Inoue, and T. Kamada, "Noninvasive evaluation of aortic regurgitation by continuous-wave Doppler echocardiography," Circulation, vol. 73, no. 3, pp. 460-466, Mar.1986.

[40] D. N. Moisseev, C. M. Nguyen, and V. Chandrasekar, "Clutter suppression for staggered PRT waveforms," Journal of Atmospheric and Oceanic Technology, vol. 25, no. 12, pp. 2209-2218, 2008.

[41] J. Y. Cho and E. S. Chornoboy, "Multi-PRI signal processing for the terminal Doppler weather radar. Part I: Clutter filtering," Journal of Atmospheric and Oceanic Technology, vol. 22, no. 5, pp. 575-582, 2005.

[42] M. Sachidananda and D. S. Zrnic, "An improved clutter filtering and spectral moment estimation algorithm for staggered PRT sequences," Journal of Atmospheric and Oceanic Technology, vol. 19, no. 12, pp. 2009-2019, 2002.

[43] S. M. Torres and D. S. Zrnic, "Ground clutter canceling with a regression filter," Journal of Atmospheric and Oceanic Technology, vol. 16, no. 10, pp. 1364-1372, 1999.

[44] S. Bjaerum, H. Torp, and K. Kristoffersen, "Clutter filter design for ultrasound color flow imaging," Ultrasonics, Ferroelectrics and Frequency Control, IEEE Transactions on, vol. 49, no. 2, pp. 204-216, 2002.

[45] A. C. H. Yu, K. W. Johnston, and R. S. Cobbold, "Frequency-based signal processing for ultrasound color flow imaging," Canadian Acoustics, vol. 35, no. 2, pp. 11-23, 2007.

[46] K. P. Burnham and D. R. Anderson, "Multimodel inference. Understanding AIC and BIC in model selection," Sociological methods & research, vol. 33, no. 2, pp. 261-304, 2004.

[47] S. Fadnes, S. A. Nyrnes, H. Torp, and L. Lovstakken, "Shunt Flow Evaluation in Congenital Heart Disease Based on Two-Dimensional Speckle Tracking," Ultrasound in medicine & biology, vol. 40, no. 10, pp. 2379-2391, 2014.

Chapter 6

Limitations, further work and concluding remarks

The methods and results included in this manuscript are discussed in the following lines. The main limitations encountered throughout this project are outlined in the first section. Further work and potential projects related to the ultrafast echocardiography approach are anticipated in the second section. The perspectives of the ultrafast cardiac echo scheme are portrayed in section number three. To finalize, some concluding remarks are shared in section number four.

6.1 Limitations

The main limitations related to the *diverging wave* ultrafast echocardiography technique are addressed in the following paragraphs. Problems encountered in both the B-mode and color Doppler ultrafast imaging modalities are briefly discussed. Some possible solutions are also proposed.

Low spatial resolution and contrast to noise ratio

The diverging ultrasound imaging technique enhances the temporal resolution at the expense of lower spatial resolution and CNR. Coherent plane-wave compounding imaging can reach very high frame rates with the same CNR displayed by the focused technique [1]. The basic difference between the diverging wave and the plane wave modalities is the transmitted beams diffraction, which for plane waves is almost negligible. The plane wave limited diffraction property is the key to high resolution and CNR. In a similar way to plane waves, the angular aperture of diverging waves can be reduced to ameliorate both the CNR and spatial resolution as presented in chapter 4 (section 4.3.2).

Motion artifacts in ultrafast B-mode echocardiography

In ultrafast ultrasound, each frame is created by coherently averaging images obtained from successively transmitted steered beams. Since compounded images are acquired one after the other one, artifacts appear in B-mode images when structures moves into the interrogated volume. A very straight forward strategy to reduce motion artifacts is to limit the amount of compounded images; however, this strategy does not always solve efficiently such a drawback.

Motion correction between successive synthetic beam transmissions has been investigated by Denarie *et al* [2]; they have proposed to perform a phase correction in the beamformed images by taking into account motion between multiple consecutive transmissions. The technique proposed by Denary *et al* could be successfully implemented into the ultrafast echocardiography technique to mitigate motion artifacts. This enhancement could solve the inconvenient to implement techniques such as speckle tracking, which require high correlation in images sequences.

Color Doppler - axial velocities only

The ultrafast color Doppler echocardiography presented in this manuscript only provides blood axial velocities. Cardiac vector blood velocity imaging would allow for more complete and further quantitative results. The *color Doppler VFM* imaging application has already been implemented using the conventional color Doppler echocardiography [3, 4], therefore validation using the ultrafast echocardiography approach should be feasible.

Signal processing in real time

The ultrafast echocardiography technique requires fast digital processing tools in order to efficiently generate images and other results. Techniques such as parallel computing and GPU processing would enable to speed up the migration, filtering and other essential signal processing tasks. On the other hand, ultrafast imaging can capture a lot more information than the human eye can perceive per time unit, therefore, two different processing standards should be available: *the first one* should allow enough data to be processed so images can be displayed at a frame rate of about 30 *fps* in real time; *the second one* should enable a more efficient off-line data processing, so quantitative analysis can be performed right after the medical examination.

6.2 Further work

Further research are needed to ameliorate the ultrafast echocardiography B-mode and color Doppler imaging modalities. Potential research subjects related to these imaging techniques are proposed in the following paragraphs:

Wall filter of the staggered PRF pulsing methodology

Although *ultrafast echocardiography* can attain very high frame rates, such a feature does not enhance the color Doppler unambiguous range itself. In this context, the staggered PFRs scheme was exploited to extend the echocardiography color Doppler Nyquist velocity, using a polynomial regression filter approach to attenuate the clutter signal stemming from slowly moving structures.

Although the polynomial filter scheme seemed to be well adapted to the staggered PRFs application, further studies are required to find out how this filtering scheme affects the velocity estimates. Considering that clutter filtering has already been extensively investigated in the weather radar staggered PRF application [5-7], some of these filtering strategies could be tried in the cardiac ultrasound imaging field.

Ultrafast color-Doppler VFM

The color Doppler VFM technique exhibits an enormous potential to investigate the cardiac hemodynamics. The *color Doppler VFM* method has already been implemented using conventional color Doppler (see chapter 2, section 2.6.3); in the past, Garcia *et al* conducted the VFM technique by averaging multiple cardiac cycles. The ultrafast echocardiography technique presented in this manuscript should provide enough information to efficiently perform the *color Doppler VFM technique* in a single cardiac cycle.

Being able to perform *color Doppler VFM* echocardiography in every cardiac cycle will facilitate to incorporate new quantitative markers into echocardiography such as vorticity, vortexes size ratio, etc. New emerging parameters that were before out of reach could revolutionize once again the cardiac echo technique.

Ultrafast color tissue Doppler imaging (TDI)

Tissue Doppler is widely used to measure volume variations of the cardiac chambers; such measurements are used to estimate the ejection fraction, which is a quantitative indicator of the ventricular function. Just like color Doppler in blood flow examinations, tissue Doppler also features important frame rate limitations (15 to 30 fps) that prevent tracking some cardiac dynamic events. Ultrafast echocardiography could be investigated to perform tissue Doppler at higher frame rates and enhance the results conveyed by this technique.

Ultrafast strain echocardiography

Strain imaging can measure tissue heart displacement and therefore it could be useful on the diagnosis of some specific cardiac diseases. Such an imaging technique is currently performed using images delivered by conventional echocardiography; the success and reliability of strain imaging has been strongly criticized because of its lack of reproducibility.

Strain imaging is based in motion tracking algorithms such speckle tracking which require image sequences to be acquired at elevated frame rates. A single motion estimate can use dozens of images, so performing multiple motion estimates per second requires an ultrafast frame rate. Ultrafast echocardiography could be investigated to improve the strain imaging technique results and reproducibility.

Ultrafast 3D echocardiography using spherical waves

3D echocardiography is and emerging technology that has steadily improved in the last 20 years. Given the 3D echocardiography computational complexity, such a technique has just been recently made available for the clinical practice. Although its presumable advantages, 3D echocardiography pertinence has been critically discussed, since no real contribution has been proved up to date. The ultrafast echocardiography advent could extensively help exploring new horizons of the 3D cardiac-echo methodology; reducing the amount of transmissions to create a whole 3D image would represents a huge advantage for this imaging approach, however, data collection and processing remains a big challenge.

6.3 Concluding Remarks

It has been verified that diverging circular beams are well suited to conduct cardiac ultrasound imaging. The use of steered diverging waves and coherent compounding proved to be a reasonable approach when being compared to conventional focused echocardiography. Rigorous *in vitro* validations showed that both the lateral and contrast resolution of the ultrafast echocardiography technique land close to those of the conventional focused echocardiography approach.

The ultrafast echocardiography method was validated in *in vivo* experiments; the heart of a healthy volunteer was recorded at a very high temporal resolution (633 fps). The images reconstructed with the ultrafast echocardiography technique were presented to two cardiologists who agreed in the good quality of the acquired images. The enhanced frame-rate used to record the events taking place during the cardiac cycles made it possible to visualise transitory events and very fine movements of the structures in the heart.

The implementation of the ultrafast color Doppler ultrasound technique using DCB was validated to increase the color Doppler temporal resolution, extend the unambiguous range and deliver more precise velocity estimates thanks to the longer *ensemble lengths* attainable.

The *in vitro* and *in vivo* results conducted with the ultrafast staggered PRFs color Doppler echocardiography technique provided extended velocity estimates beyond the conventional Nyquist limit at very high frame rates; The implementation of such a technique would have not been possible without the use of diverging beams.

The DCB ultrafast echocardiography approach sacrifices image quality for higher B-mode and color Doppler frame rates. The high temporal resolution provided by the ultrafast echocardiography scheme has been exploited to extend the Nyquist limit, and it could be exploited to perform other valuable imaging techniques, *e.g.* speckle tracking and color Doppler VFM.

Biobliography

[1] G. Montaldo*, et al.*, "Coherent plane-wave compounding for very high frame rate ultrasonography and transient elastography," *Ultrasonics, Ferroelectrics and Frequency Control, IEEE Transactions on,* vol. 56, pp. 489-506, 2009.

[2] B. Denarie*, et al.*, "Coherent plane wave compounding for very high frame rate ultrasonography of rapidly moving targets," *Medical Imaging, IEEE Transactions on,* vol. 32, pp. 1265-1276, 2013.

[3] D. Garcia*, et al.*, "Two-dimensional intraventricular flow mapping by digital processing conventional color-Doppler echocardiography images," *Medical Imaging, IEEE Transactions on,* vol. 29, pp. 1701-1713, 2010.

[4] G.-R. Hong*, et al.*, "Characterization and quantification of vortex flow in the human left ventricle by contrast echocardiography using vector particle image velocimetry," *JACC: Cardiovascular Imaging,* vol. 1, pp. 705-717, 2008.

[5] G. Meymaris*, et al.*, "A simplified approach to staggered PRT clutter filtering," in *Preprints, 25th Conf. on Interactive Information Processing Systems for Meteorology, Oceanography, and Hydrology, Phoenix, AZ, Amer. Meteor. Soc. B*, 2009.

[6] M. Sachidananda and D. Zrnic, "Clutter filtering and spectral moment estimation for Doppler weather radars using staggered pulse repetition time (PRT)," *Journal of Atmospheric and Oceanic Technology,* vol. 17, pp. 323-331, 2000.

[7] S. M. Torres*, et al.*, "Design, implementation, and demonstration of a staggered PRT algorithm for the WSR-88D," *Journal of Atmospheric and Oceanic Technology,* vol. 21, pp. 1389-1399, 2004.